T.R.

GEBZE TECHNICAL UNIVERSITY

GRADUATE SCHOOL OF NATURAL AND APPLIED SCIENCES

FABRICATION AND CHARACTERIZATION OF UNDOPED AND DOPED PNN-PZT CERAMICS AND COMPOSITES

EZGİ YALÇIN

A THESIS SUBMITTED FOR THE DEGREE OF

MASTER OF SCIENCE

DEPARTMANT OF MATERIALS SCIENCE AND ENGINEERING

GEBZE

2022

T.R.

GEBZE TECHNICAL UNIVERSITY

GRADUATE SCHOOL OF NATURAL AND APPLIED SCIENCES

FABRICATION AND CHARACTERIZATION OF UNDOPED AND DOPED PNN-PZT CERAMICS AND COMPOSITES

EZGİ YALÇIN

A THESIS SUBMITTED FOR THE DEGREE OF MASTER OF SCIENCE

DEPARTMENT OF MATERIALS SCIENCE AND ENGINEERING

THESIS SUPERVISOR

PROF. DR. EBRU MENŞUR ALKOY

GEBZE

2022

T.C.
GEBZE TEKNİK ÜNİVERSİTESİ
FEN BİLİMLERİ ENSTİTÜSÜ

KATKISIZ VE KATKILI PNN-PZT SERAMİKLERİN VE KOMPOZİTLERİN ÜRETİMİ VE KARAKTERİZASYONU

EZGİ YALÇIN

YÜKSEK LİSANS TEZİ
MALZEME BİLİMİ VE MÜHENDİSLİĞİ ANABİLİM DALI

DANIŞMANI
PROF. DR. EBRU MENŞUR ALKOY

GEBZE
2022

GEBZE TEKNİK ÜNİVERSİTESİ	**YÜKSEK LİSANS JÜRİ ONAY FORMU**

GTÜ Fen Bilimleri Enstitüsü Yönetim Kurulu'nun 09/06/2022 tarih ve 2022/28 sayılı kararıyla oluşturulan jüri tarafından 23/06/2022 tarihinde tez savunma sınavı yapılan Ezgi YALÇIN'ın tez çalışması Malzeme Bilimi ve Mühendisliği Anabilim Dalında YÜKSEK LİSANS tezi olarak kabul edilmiştir.

JÜRİ

ÜYE (TEZ DANIŞMANI)	:Prof. Dr. Ebru MENŞUR ALKOY
ÜYE	:Prof. Dr. Metin USTA
ÜYE	:Dr. Öğr. Üyesi Ali AKMAN

ONAY

Gebze Teknik Üniversitesi Fen Bilimleri Enstitüsü Yönetim Kurulu'nun ...…/……/…… tarih ve ……/…..... sayılı kararı.

İMZA/MÜHÜR

SUMMARY

In this study, the usability of lead nickel niobate–lead zirconate titanate (PNN-PZT) composition in $0.5Pb(Ni_{1/3}Nb_{2/3})O_3$-$0.35PbTiO_3$-$0.15PbZrO_3$ composition, which has superior piezoelectric properties, in applications such as passive underwater listening was investigated. Undoped and 0.5, 1.0, 1.5 mol % manganese (Mn), iron (Fe), neodymium (Nd)-doped ceramics were produced by the columbite precursor method. The produced ceramics were sintered at 1200℃ for 4 hours. Electrical and structural analyzes were performed for doped and undoped ceramics.

Fibers were produced from undoped PNN-PZT powders by alginate gelation method. Piezocomposites with 1-3 connectivity were produced from these fibers. Commercially available PZT-5A and PZT-5H ceramics were also produced for comparison of underwater acoustic performance with the undoped PNN-PZT piezocomposite.

Pure perovskite phase was obtained for Mn, Fe and 0.5% Nd-doped ceramics. There was not observed any secondary phase for 1.0% and 1.5% Nd-doped ceramics. Mn and Fe-doped ceramics exhibited electrically hard character whereas Nd-doped ceramics exhibited soft character.

Due to the higher piezoelectric properties, free field voltage sensitivity (FFVS)-transmission voltage response (TVR) values, flexibility, and larger bandwidth of 1-3 PNN-PZT piezocomposite, it can be promising for underwater acoustic applications.

Key Words: Lead Nickel Niobate-Lead Zirconate Titanate (PNN-PZT), Alginate Gelation, 1-3 Piezocomposite, Doped, Relaxor Ferroelectric.

ÖZET

Bu çalışmada üstün piezoelektrik özelliklere sahip olan $0.5Pb(Ni_{1/3}Nb_{2/3})O_3$-$0.35PbTiO_3$-$0.15PbZrO_3$ bileşimindeki kurşun nikel niyobat–kurşun zirkonat titanat (PNN-PZT) kompozisyonunun sualtı uygulamalarında kullanılabilirliği incelenmiştir. Molce %0.5, %1.0, %1.5 oranlarında mangan (Mn), demir (Fe), neodimiyum (Nd) katkılı ve katkısız PNN-PZT tozları kolumbit öncül metodu ile üretilmiştir. Üretilen seramikler 1200℃ 'de 4 saat süre ile sinterlenmiştir. Katkılı ve katkısız seramiklere elektriksel ve yapısal analizler yapılmıştır.

Katkısız PNN-PZT tozlarından alginate jelleşmesi yöntemi ile fiberler üretilmiştir. Bu fiberler kullanılarak 1-3 bağlantılı piezokompozitler üretilmiştir. Ayrıca ticari PZT-5A ve PZT-5H seramikleri de üretilmiş ve sualtı akustik performansları katkısız PNN-PZT piezokompozit ile kıyaslanmıştır.

Mn, Fe ve %0.5 Nd katkılı seramiklerde saf perovskite fazı elde edilmiştir. %1.0 ve %1.5 Nd katkılı seramiklerde ise ikincil faz gözlemlenmiştir. Mn ve Fe katkılı seramikler elektriksel olarak sert karakter gösterirken, Nd katkılı seramikler ise elektriksel olarak yumşak karakter sergilemiştir.

1-3 PNN-PZT piezokompozit, yüksek piezoelektrik özellikleri, serbest alan voltaj hassasiyeti (FFVS)-voltaj iletim cevabı (TVR) değerleri, esnekliği ve yüksek band genişliğinden dolayı sualtı akustik uygulamalar için ön plana çıkmaktadır.

Anahtar Kelimeler: Kurşun Nikel Niyobat-Kurşun Zirkonat Titanat (PNN-PZT), Alginate Jelleşmesi, 1-3 Piezokompozit, Katkılı, Relaksör Ferroelektrik.

ACKNOWLEDGEMENT

I would like to express my gratitude to my supervisor Prof. Dr. Ebru Menşur Alkoy for her guidence, support and motivation during my thesis study and education. Also, I would like to thank Prof. Dr. Sedat Alkoy for his guidence and criticism during completing of this thesis successfully.

I want to thank to thesis jury members; Prof. Dr. Metin Usta and Assoc. Prof. Ali Akman for their criticism and valuable opinions.

I would like to thank Assist. Prof. Mustafa Yunus Kaya and Assist. Prof. Ayşe Berksoy Yavuz for their guidence and valuable opinions. I would like to thank lecturer Namık Kemal Gözüaçık and Hüseyin Alptekin Sarı for their help during my thesis study and thank to all members of 'Piezodevices Research Group' for their support and help.

I would like to thank technician Adem Şen for XRD analyses and lecturer Ahmet Nazım for SEM analyses.

Lastly, the most special appreciation to my family; my mother Sevgi Abussuutoğlu, my father Mahmut Abussuutoğlu, my husband Yusuf Yalçın, my sister Elif Yüksel, my niece Kumsal Ada Yüksel. They always supported me on my decisions in my life. I want to dedicate this thesis to my husband Yusuf Yalçın.

TABLE of CONTENTS

	Page
SUMMARY	v
ÖZET	vi
ACKNOWLEDMENT	vii
TABLE of CONTENTS	viii
LIST of ABBREVIATIONS and ACRONYMS	x
LIST of FIGURES	xii
LIST of TABLES	xv
1. INTRODUCTION	1
1.1. Aim of the Study	2
2. LITERATURE REVIEW	3
2.1. Electroceramics	3
2.2. Dielectricity	4
2.3. Piezoelectricity	8
2.4. Ferroelectricity	10
2.5. PNN-PZT Composition	14
2.6. Piezoelectric Ceramic Fiber Production	20
2.7. Electroceramic Composite	21
3. EXPERIMENTAL STUDY	23
3.1. Synthesis of the PNN-PZT Ceramic Powders	23
3.2. Synthesis of the PNN-PZT Ceramics	25
3.3. Synthesis of Fibers	26
3.4. Structural and Electrical Analysis	28
4. RESULTS AND DISCUSSION	30
4.1. Phase Analysis of PNN-PZT Compositions	30
4.1.1. XRD Analysis of $NiNb_2O_6$ Powder	30
4.1.2. XRD Analysis of PNN-PZT Powders and Ceramics	30
4.1.3. SEM Analysis of PNN-PZT Ceramics and Fibers	36
4.2. Electrical Measurement Results	38
4.2.1. Dielectric Measurements	38

4.2.2. Polarization-Electric Field Hysteresis Measurements 48
4.2.3. Effects of Doping on PNN-PZT Ceramic 53
4.2.4. Electromechanical Properties of the PNN-PZT Ceramics 55
4.2.5. Underwater Measurement Results of PNN-PZT Ceramics and Composite 58
5. CONCLUSION 62

REFERENCES 63
BIOGRAPHY 69

LIST OF ABBREVIATIONS AND ACRONYMS

Abbreviations and Acronyms		**Explanations**
°	:	Degree
℃	:	Degree Celcius
%	:	Percentage
2θ	:	X-ray Diffraction Angle
γ	:	Diffusive Constant
dB	:	Decibel
Ø	:	Diameter
$V_{\ddot{O}}$	:	Oxygen Vacancy
Q_m	:	Mechanical Quality Factor
E_c	:	Coercive Field
T_c	:	Curie Temperature
ε_r	:	Dielectric Permittivity
pC/N	:	PicoColoumb per Newton
P	:	Polarization
p	:	Dipole Moment
P_m	:	Maximum Polarization
P_r	:	Remnant Polarization
f_r	:	Anti-Resonance Frequency
E	:	Electric Field
k_p	:	Electromechanical Coefficient
k	:	Electromechanical Coupling Factor
Å	:	Angstrom
ε_0	:	Permittivity of Free Space
ε'	:	Real Component of Dielectric Permitivity
ε"	:	Imaginary Component of Dielectric Permitivity
χ_e	:	Electric Susceptibility
X	:	Stress
Z	:	Acoustic Impedance
x	:	Strain

n	:	Unit Vector
f_a	:	Anti-Resonance Frequency
FFVS	:	Free Field Voltage Sensitivity
MPB	:	Morphotropic Phase Boundary
PNN	:	Lead Nickel Niobate- $Pb(Ni_{1/3}Nb_{2/3})O_3$
PZT	:	Lead Zirconate Titanate- $Pb(Zr_yTi_{1-y})O_3$
rpm	:	Rotation per Minute
SEM	:	Scanning Electron Microscope
TVR	:	Transmission Voltage Response
XRD	:	X-ray diffraction

LIST OF FIGURES

Figure No:		Page
2.1:	Classification of ceramic materials	3
2.2:	Types of dielectric materials and their relationships	4
2.3:	Schematic representation of polarized material	5
2.4:	Schematic representation of polarization mechanisms	7
2.5:	Relationship between dielectric polarization and frequency	8
2.6:	Piezoelectric and subgroup relationship based on symmetry	8
2.7:	Impedance of a piezoelectric ceramic at resonance	10
2.8:	Phase transition from paraelectric to ferroelectric for $PbTiO_3$	11
2.9:	Hysteresis loop of a typical ferroelectric ceramic	12
2.10:	Phase diagram of PZT	13
2.11:	Phase diagram of PNN-PZT system. F_α : rhombohedral phase, F_β: tetragonal phase, FPC: pseudocubic phase, P: cubic paraelectric phase, A_α: antiferroelectric phase	15
2.12:	Gelation and stereochemical structure of the GG dimer block	20
2.13:	Different connectivity types for composites	22
2.14:	Schematic representation of 1-3 connectivity in piezocomposite	22
3.1:	The flowchart of the powder fabrication	24
3.2:	The picture of uncoated and silver electrode coated bulk ceramics	26
3.3:	Fiber drawing machine	27
3.4:	Flowchart of the pictures of from one fiber to composite	28
3.5:	Picture of PNN-PZT piezocomposite and ceramic for underwater measurements	29
4.1:	XRD pattern of the $NiNb_2O_6$ powder	30
4.2:	XRD pattern of calcined undoped and Mn-doped powders	31
4.3:	XRD pattern of sintered undoped and Mn-doped ceramics	31
4.4:	XRD pattern of calcined undoped and Fe-doped powders	32
4.5:	XRD pattern of sintered undoped and Fe-doped ceramics	32
4.6:	XRD pattern of calcined undoped and Nd-doped powders	33
4.7:	XRD pattern of sintered undoped and Nd-doped ceramics	33

4.8:	Comparison of the (002)/(200) peaks of undoped and Mn-doped ceramics in detail.	34
4.9:	Comparison of the (002)/(200) peaks of undoped and Fe-doped ceramics in detailed	35
4.10:	Comparison of the (002)/(200) peaks of undoped and Nd-doped ceramics in detailed	35
4.11:	SEM micrograph of sintered PNN-PZT ceramic	36
4.12:	SEM micrographs of (a) 0.5% Mn, (b) 1.0% Mn, (c) 1.5% Mn, (d) 0.5% Fe, (e) 1.0% Fe, (f) 1.5% Fe, (g) 0.5% Nd, (h) 1.0% Nd (ı) 1.5% Nd doped ceramics	37
4.13:	SEM micrographs of cross-sectional fiber surface a) 125x b)500x c)1000x d)2000x	38
4.14:	Optic microscope images of PNN-PZT piezocomposite a)50x b)100x	38
4.15:	Temperature correlation of the dielectric constant and loss tangent of undoped ceramic	39
4.16:	$\ln(1/\varepsilon_r - 1/\varepsilon_m)$-ln $(T-T_m)$ relation for undoped ceramic	40
4.17:	Temperature correlation of the dielectric constant and loss tangent of (a) 0.5% Mn, (b) 1.0% Mn, (c) 1.5% Mn-doped ceramics	42
4.18:	Temperature correlation of the dielectric constant and loss tangent of Mn-doped ceramics at 1 kHz	42
4.19:	Temperature correlation of the dielectric constant and loss tangent of (a) 0.5% Fe, (b) 1.0% Fe, (c) 1.5% Fe-doped ceramics	44
4.20:	Temperature correlation of the dielectric constant and loss tangent of Fe-doped ceramics at 1 kHz	44
4.21:	Temperature correlation of the dielectric constant and loss tangent of (a) 0.5% Nd, (b) 1.0% Nd, (c) 1.5% Nd-doped ceramics	46
4.22:	Temperature correlation of the dielectric constant and loss tangent of Nd-doped ceramics at 1 kHz	46
4.23:	P–E hysteresis loops of undoped ceramic	48
4.24:	Comparison of P–E hysteresis loops of undoped and Mn-doped ceramics	49

4.25:	Comparison of P–E hysteresis loops of undoped and Fe-doped ceramics	50
4.27:	Comparison of P-E hysteresis loops and strain curves of PNN-PZT ceramic and PNN-PZT piezocomposite	52
4.28:	Possible defect chemistry reacitons for dopants	54
4.29:	Empedance vs. frequency measurements of undoped and Mn-doped ceramics	55
4.30:	Empedance vs. frequency measurements of undoped and Fe-doped ceramics	56
4.31:	Empedance vs. frequency measurements of undoped and Nd-doped ceramics	56
4.32:	Admittance-phase angle vs. frequency measurements of undoped, PZT-5A, PZT-5H and piezocomposite	58
4.33:	TVR vs. frequency measurements of undoped, PZT-5A, PZT-5H and piezocomposite	60
4.34:	FFVS vs. frequency measurements of undoped, PZT-5A, PZT-5H and piezocomposite	61

LIST OF TABLES

Table No:		Page
2.1:	Electrical and electromechanical properties of PNN-PZT ceramics studied in the literature	18
3.1:	Information about oxide powders	23
3.2:	The used chemicals of the binder solution	25
3.3:	The raw materials used in the preparation of slurry and their weights	26
4.1:	Dielectric properties of undoped and doped PNN-PZT ceramics	47
4.2:	P_{max}, P_r and E_c values of doped PNN-PZT ceramics	51
4.3:	P_{max}, P_r, E_c and maximum strain values of doped PNN-PZT composite and ceramic	53
4.4:	Electromechanical properties of undoped and doped ceramics	57
4.5:	Resonance and antiresonance frequencies of ceramics	59

1. INTRODUCTION

Piezoelectric materials show an electrical potential (direct effect) against a mechanical effect or mechanical strain (converse effect) against an electric field. Piezoelectric materials are widely used in applications such as transducers, sensors. In particular, lead-based compositions have been the subject of many different studies in the literature due to their superior piezoelectric properties compared to lead-free compositions [Kaya, 2018]. Because the triple system has a wider morphotropic phase boundary (MPB) than a secondary system like PZT, several piezoelectric ceramic of the triple system have recently been found. $Pb(B'B'')O_3$ is the general formula for relaxor ferroelectrics fabricated from lead. Because of its exceptional piezoelectric properties 0.5PNN-0.5PZT in this ternary system has garnered increasing attention [Kang and Kang, 2019].

Piezoelectric ceramic materials can be in disc, cylindrical, and spherical forms. However, especially in underwater applications, a transducer with a frequency lower than 100 kHz will only be able to operate if it exhibits a very significant shape change. The electric field generated strain in piezoelectric ceramic materials is restricted to 0.1-0.2%. Piezoelectric ceramic materials can be used in fiber structures, which give anisotropy and flexibility in underwater sonar, vibration control, and energy harvesting applications [Mensur-Alkoy et al., 2015].

Piezoceramic fibers are fabricated using a variety of techniques. The alginate gelation fiber drawing procedure, which was first reported by Alkoy et al, is preferred among these methods since it is an environmentally process [Mensur-Alkoy et al., 2020]. Phase connectivity, defined as the manner in which the constituent phases are interconnected, has been proven to be a critical element in composite material design. 0-0, 1-0, 2-0, 3-0, 1-1, 2-1, 3-1, 2-2, 3-2, and 3-3 are the ten potential connection notation. Parallel PZT rods inserted in a three-dimensional continuous polymer matrix make up a 1-3 connectivity notation [Gururaja et al., 1985].

1.1. Aim of the Study

The main aim of this thesis is to fabricate 1-3 piezocomposite from 0.5PNN-0.5PZT ceramic composition for underwater accoustic applications. The main objectives planned to be achieved as a result of this thesis are as follows: firstly, undoped and manganese (Mn), iron (Fe) and neodimyum (Nd)-doped PNN-PZT powders will be produced by using the columbite precursor method. Structural and electrical characterization of doped and undoped PNN-PZT ceramics will be carried out. PNN-PZT fibers will be fabricated by alginate gelation method. 1-3 PNN-PZT piezocomposite will be fabricated to obtain higher piezoelectric properties, FFVS-TVR values, flexibility and larger bandwidth as a contribution to the literature. 1-3 piezocomspoite, PZT-5A, PZT-5H, PNN-PZT ceramics will be electrically and acoustically characterized.

2. LITERATURE REVIEW

2.1. Electroceramics

Ceramic materials are water-insoluble inorganic, non-metallic compounds with ionic additions in their chemical bonds [Setter and Waser, 1999]. Ceramic materials are thought to have originated somewhere in ancient times, possibly with the production of bricks, pottery and tiles [Miclea et al., 2002]. Classification of ceramics according to their usage areas is given in Figure 2.1 [Callister, 2007].

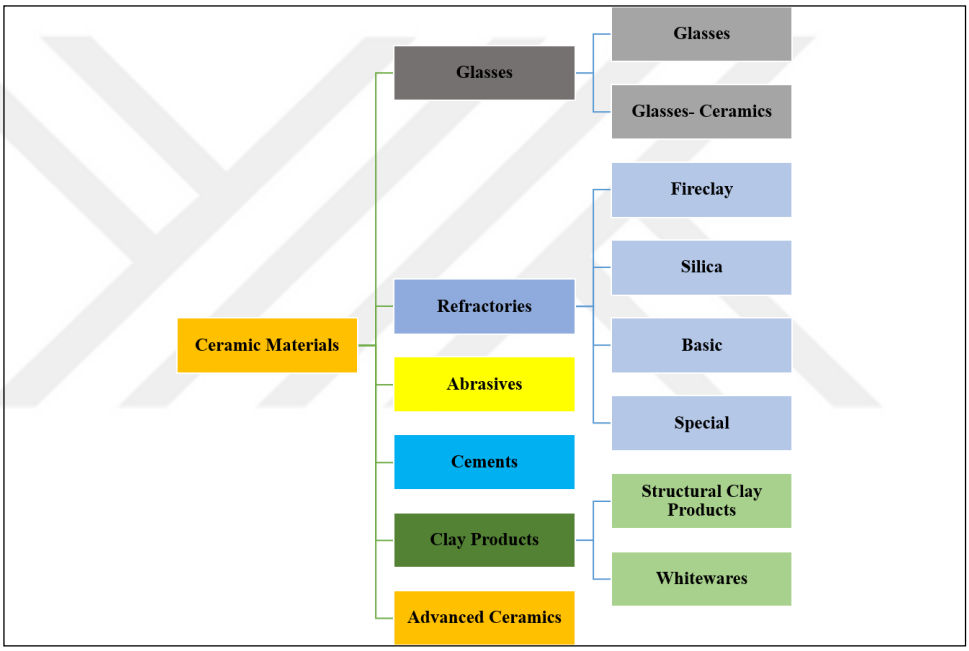

Figure 2.1: Classification of ceramic materials.

Traditional and advanced technology ceramics are the two major types of ceramics. Traditional ceramics include clay, porcelain, glass, refractory whereas advanced ceramics include aluminum nitride, zirconia, silicon nitride. Ceramic materials are generally hard, have high abrasion resistance and thermal shock resistance, are fire resistant, insulating, transparent and have high oxidation resistance. On the other hand, some ceramics are electrically and thermally highly conductive and superconductive. The properties of a ceramic depend on its microstructure, which depends on the composition and process conditions of the ceramic. Ceramic materials are used in many different applications due to such properties [Wang, 2012]. Electroceramic materials are advanced technology ceramics used especially for their

electrical properties. Electroceramic materials are used in ferroelectric, pyroelectric, piezoelectric, electro-optical devices and multilayer capacitor, sensor, actuator, underwater sonar applications [Bharadwaj et. al., 2012].

2.2. Dielectricity

Dielectric materials are electrically insulating and have electric dipole structure; this means that the positive and negative electrical charges are separated at the molecular or atomic level. When an electric field is applied to an ideal dielectric material, no charge transfer occurs, but only a limited rearrangement occurs, resulting in the dielectric gaining a dipole moment and becoming polarized [Callister, 2007], [Moulson and Herbert, 2003]. There is no such thing as a perfect dielectric on this planet. Although a perfect vacuum is close to the ideal dielectric, it cannot be achieved on Earth [Kao, 2004]. Types of dielectric materials and their relationships are given in Figure 2.2 [Khan and Upadhyay, 2021].

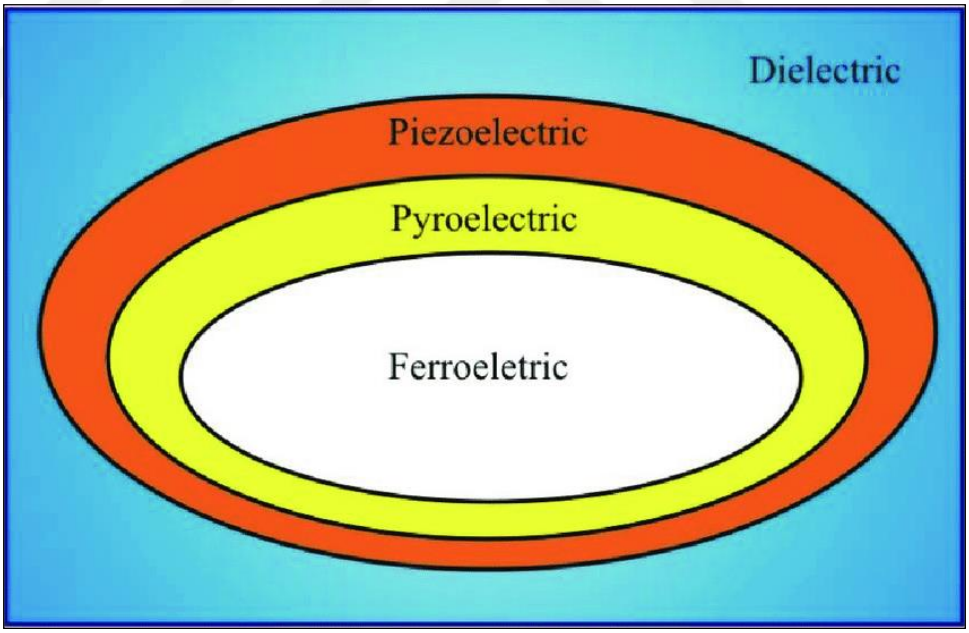

Figure 2.2: Types of dielectric materials and their relationships.

Electric dipole is made up of two equal opposing charges separated with a space δx in its most basic form. The dipole moment of the dipole, p, is described as

$$p = Q\delta x \tag{2.1}$$

2.1 is a vector whose positive direction is from negative to positive charge. As illustrated in Figure 1.3, polarized material is formed up of dipolar prisms, the end faces of which have surface charge densities of $+\sigma_p$ and $-\sigma_p$ [Moulson and Herbert, 2003]. The polarization refers to the dipole moment per unit volume of material, which varies by area. In Figure 2.3 the vectors magnitudes are given by

$$\delta p = \sigma p \delta A \delta x \tag{2.2}$$

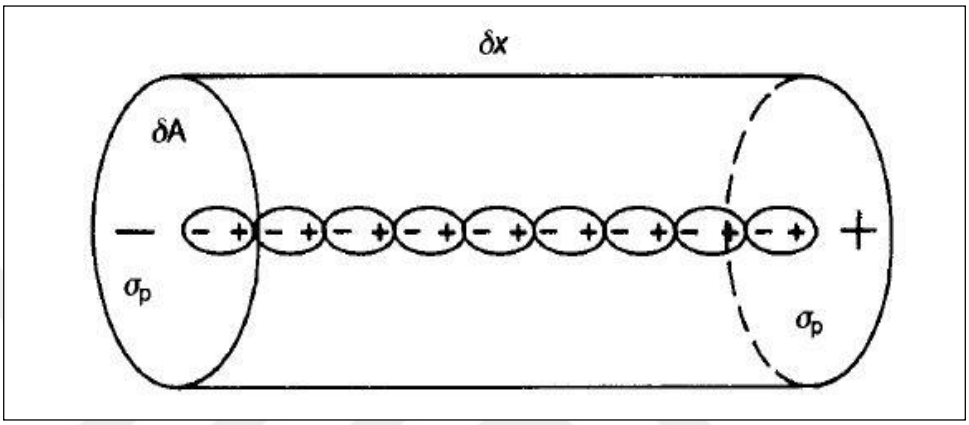

Figure 2.3: Schematic representation of polarized material.

$\sigma p = n.P$ where **n** is unit vector normal to surface of polarized material and directed from the material outwards. Magnitude of the vector of electric displacement, can be stated as

$$D = P + E\varepsilon_0 \tag{2.3}$$

where ε_0 is the permittivity of free space. In the case of the dielectric is 'linear', meaning that polarization is proportional to the electric field in the material as is most often the case,

$$P = E\chi_e\varepsilon_0 \tag{2.4}$$

where χ_e is the electric susceptibility which is a dimensionless constant [Moulson and Herbert, 2003]. Permittivity (ε) is an fundamental electrical property of dielectric materials. The dielectric constant is a term used to describe the relative permittivity of a material. Relative permittivity of the dielectric materials is represented ε_r. The dielectric constant depends on the frequency of the electric field,

structure and the defects of the material, temperature and pressure [Moulson and Herbert, 2003], [Kao, 2004].

In a dielectric material, there are atoms or molecules with one or more of the four types of electrical polarization [Kao, 2004]. Types of the polarization are given in the Figure 2.4 [Liu et al., 2019]. Electronic polarizability is caused by the movement of electrons in an atom relative to the atomic nucleus under an external electric field. Ionic polarizability is caused by the relative displacement of positive and negative ions from their equilibrium locations to a distance less than the spacing between neighboring ions. Only materials containing complex ions with a persistent dipole moment have dipolar polarizability, also known as orientational polarizability. Charge carriers travel in a constrained manner until they come into a potential barrier, such as a grain or phase boundary, in space charge polarization [Moulson and Herbert, 2003], [Khan and Upadhyay, 2021].

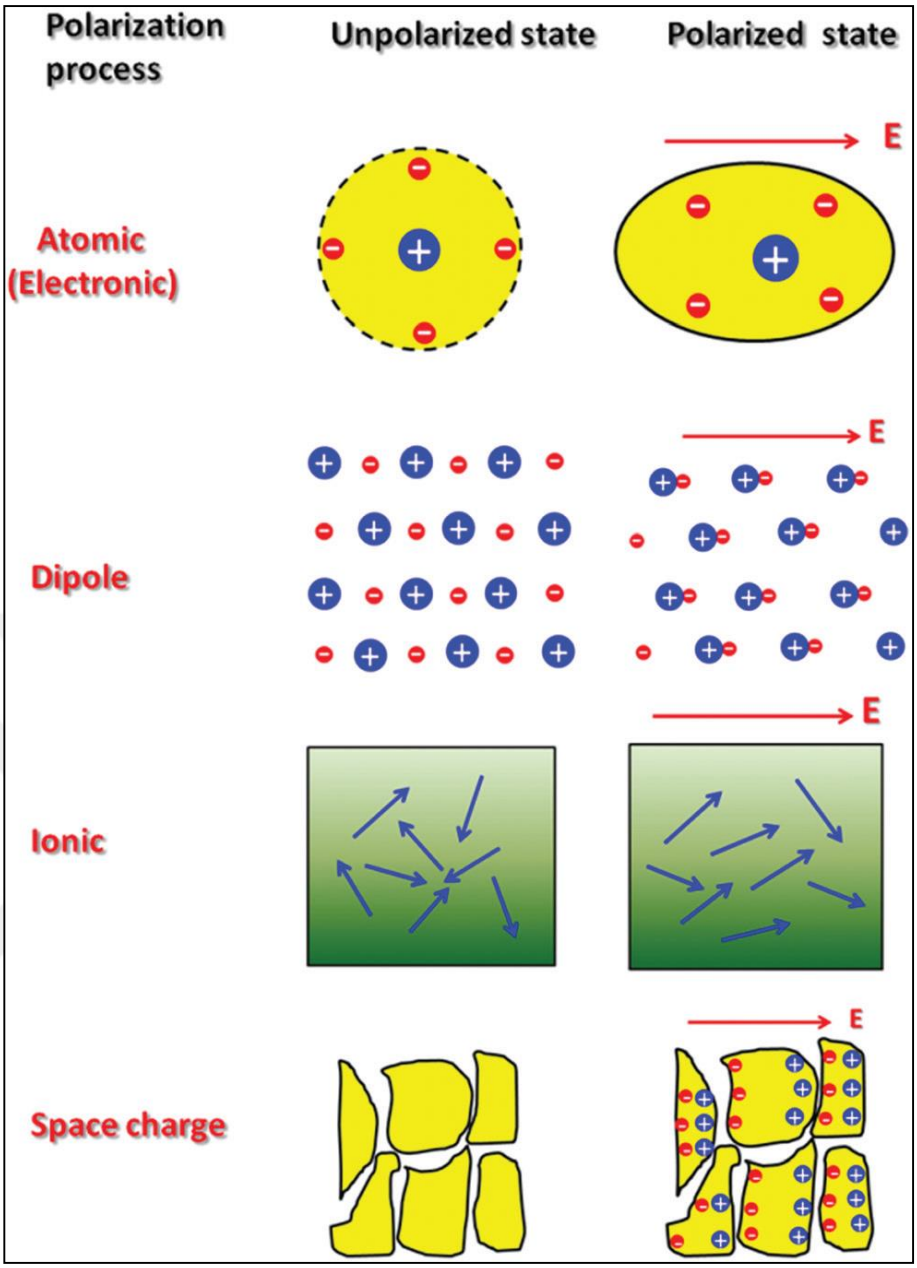

Figure 2.4: Schematic representation of polarization mechanisms.

In Figure 2.5, I is represent the radio frequency range, II is represent the microwave frequency range, III is represent the infrared-visible frequency range, IV is represent the ultraviolet frequency range [Bibi et al., 2016].

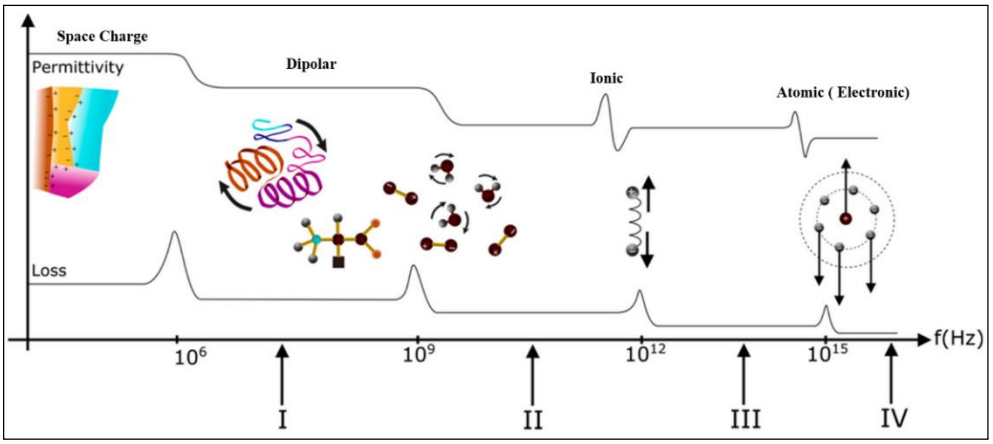

Figure 2.5: Relationship between dielectric polarization and frequency.

2.3. Piezoelectricity

The name "piezoelectric" comes from the Greek word "piezo," which literally means "to press."Piezoelectric materials are that have the natural capacity to create electrical polarization when mechanical stress is applied. This action may be achieved in the other direction, mechanical strain can be produced by putting electrical field. The piezoelectric effect or piezoelectricity is the name for this phenomena [Padasalkar et. al., 2015]. Piezoelectric effect was discovered by the French physicists Pierre Curie and Paul-Jean Curie. It is the emergence of electrical energy on the crystals when they are operated upon by mechanical stress [Bain, 2017]. The unit cell is the smallest repeating unit in the lattice, and its symmetry to indicate whether piezoelectricity may occur in the crystal. The absence of a center of symmetry is critical for the presence of piezoelectricity. The relationship between piezoelectricity and its subgroups based on symmetry is given in the Figure 2.6 [Haertling, 1999].

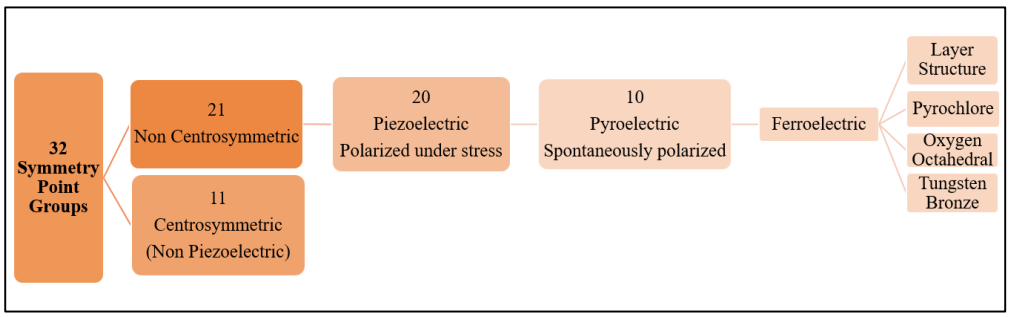

Figure 2.6: Piezoelectric and subgroup relationship based on symmetry.

The magnitude of the polarization is proportional to the magnitude of the voltage, and the proportionality constant is expressed by the piezoelectric coefficient (d_{ij}). High electrostrictive coefficient, self-polarization high dielectric permittivity leads to high piezoelectric coefficient [Newnham, 2005]. Piezoelectric coefficients are typically represented by two inferiors indicating the direction of the properties. The first inferior represent the electric field E direction (or the displacement). The second inferior represent the mechanical stress X direction (or the strain) [Kao, 2004].

The piezoelectric strain coefficient d, the piezoelectric voltage coefficient g, the electromechanical coupling coefficient k, the mechanical quality factor Q_m, and the acoustic impedance Z are the five most essential figures of merit for piezoelectric compostions. The magnitude of the induced strain x by an external electric field E is the piezoelectric strain constant. Piezoelectric strain constant is important property for actuator applications.

$$x = dE \tag{2.5}$$

Through the piezoelectric voltage constant g, the induced electric field E is related to a stress X.

$$E = \mathrm{g}X \tag{2.6}$$

k is the electromechanical coupling factor shown as below

$$k^2 = \text{Stored mechanical energy/Input electiracal energy} \tag{2.7}$$

or

$$k^2 = \text{Stored electrical energy/Input mechanical energy} \tag{2.8}$$

The acoustic impedance is a argument used to evaluate the transfer of acoustic energy between two materials. Z is defined by,

$$Z^2 = \text{Pressure/Volume Velocity} \tag{2.9}$$

The proportion of reactance to resistivity in a material is known as the mechanical quality factor (Q_m). The impedance value of piezoelectric ceramic is lowest at resonance frequency (f_r) and highest at anti-resonance frequency (f_a). Q_m is a mechanical quality factor that expresses the sharpness of the electromechanical resonance peak [Uchino, 2010], [Xu, 1991], [Jordan and Qunaies, 2001]. Knowing the impedance characteristics is critical in high-power applications so that maximum transmission performance may be attained. Figure 2.7 shows the frequency dependent impedance for a piezoelectric ceramic [Davari et. al., 2014], [Dong et al., 2010].

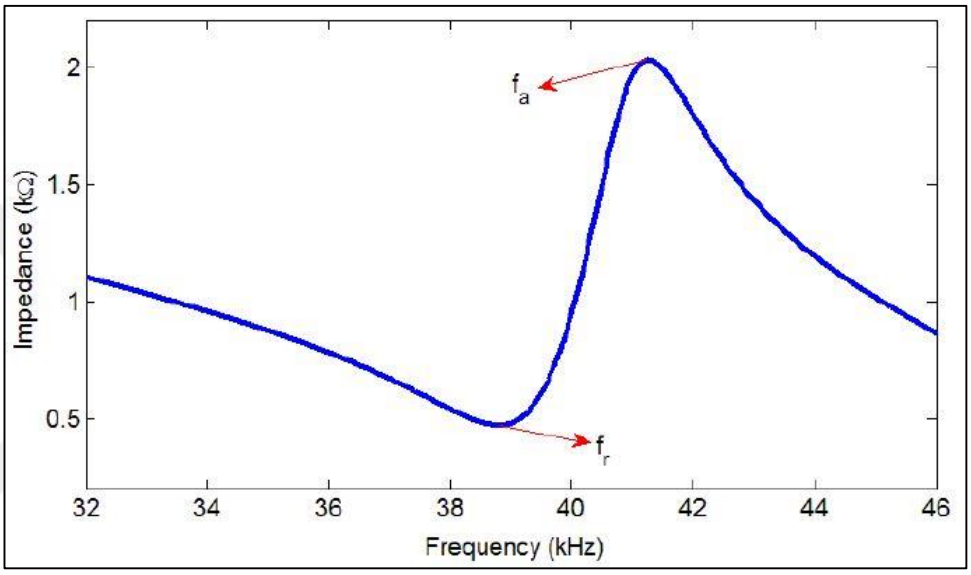

Figure 2.7: Impedance of a piezoelectric ceramic at resonance.

2.4. Ferroelectricity

In the lack of an external electric field, ferroelectrics have at least two equilibrium orientations of the spontaneous polarization, and the spontaneous polarization vector can be exchanged between those orientations by an electric field. The structural phase transition of most ferroelectric materials occurs from a high-temperature non-ferroelectric (or paraelectric) phase to a low-temperature ferroelectric phase. Symmetry of the ferroelectric phase is always less than that of the paraelectric phase. The Curie point, T_C, is the temperature at which a phase transition occurs. Figure 2.8 shows, changes that can occur in a ferroelectric material as it transitions from a paraelectric cubic to a ferroelectric tetragonal phase [Damjanovic, 1998], [Andres, 2012].

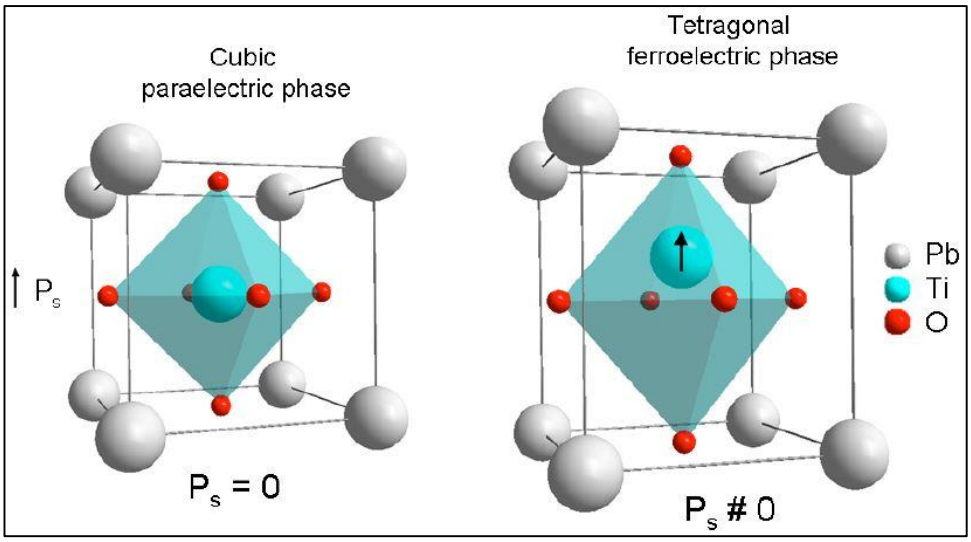

Figure 2.8: Phase transition from paraelectric to ferroelectric for $PbTiO_3$.

As the ferroelectric material cools with the paraelectric-ferroelectric phase transition, ferroelectric domains emerge to reduce the electrostatic energy of depolarizing fields and the elastic energy associated with mechanical limitations [Andres, 2012]. Figure 2.9 shows, a typical ferroelectric hysteresis loop. In the loop, polarization increases as the electric field increases (2-3), then the polarization saturates once the electric field reaches a particular value (3-4). If the electric field decreases, the polarization mechanism follows the 4, 3 and 5 paths, respectively. Point 5 represents remnant polarization (P_r), which is polarization value of the material after the removal of the electric field. When electrcic field decreases, polarization decreases (5-6). At point 6, there is no polarization even if there is an applied electric field. Beacuse of the switching of domains in the reverse direction along with the electric field. Coercive field (E_c) is this point. That is the field necessary to carry the polarization to zero. The reverse polarization mechanism is represented by 6-7. Remnant polarization is shown in reverse direction by 8 [Kao, 2004], [Vilarinho, 2001].

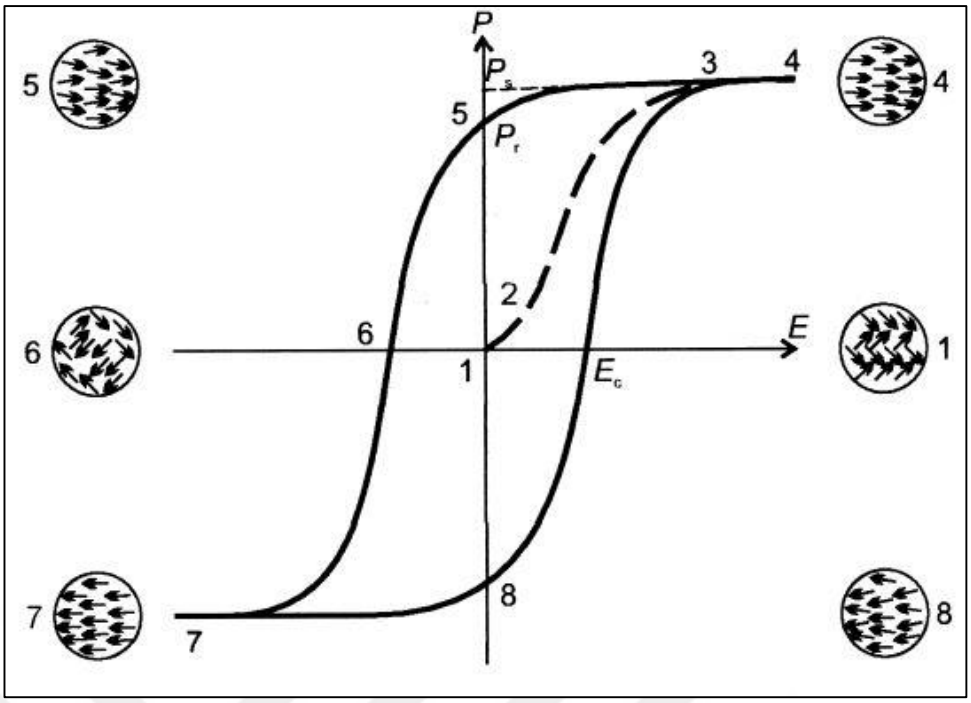

Figure 2.9: Hysteresis loop of a typical ferroelectric ceramic.

Perovskite crystal structure is observed in most commercial piezoelectric ceramics [Trolier-McKinstry et al., 2018]. The perovskite structure is represented to as ABO_3. A ions are at the corner of the unit cell, B ions are at the center, and O are at the centers of surface [Roth, 1957]. Barium titanate ($BaTiO_3$), lead titanate ($PbTiO_3$), lead lanthanum zirconate titanate (PLZT), lead magnesium niobate (PMN) have perovskite structure. The ions Ti^{4+} and Zr^{4+} occupy the B site, whereas Pb^{2+} ions occupy the A site in lead zirconate titanate (PZT), which has a perovskite structure. Excellent piezoelectric characteristics are seen in PZT near the morphotropic phase boundary (MPB), which separates the tetragonal and orthorhombic phases [Safari et al., 2000]. Figure 2.10 illustrates the PZT phase diagram [Yang et. al., 2010].

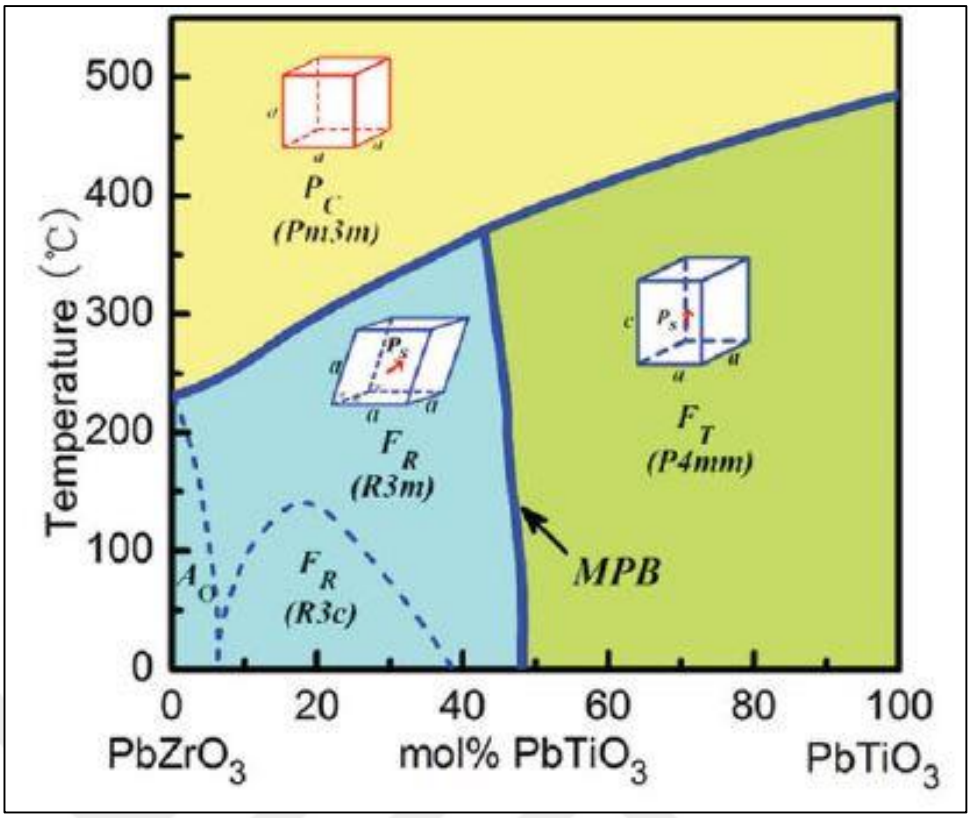

Figure 2.10: Phase diagram of PZT.

Some ferroelectrics, known as relaxor ferroelectrics, have gotten a lot of interest in recent years due to their unusual dielectric properties. The following are some notable properties of the dielectric response of relaxor materials: a) the temperature dependence of the dielectric permittivity is characterized by wide peaks, and b) the temperature of the corresponding maximum for the real (ε') and imaginary (ε") components of the dielectric permittivity appears at different values, indicating frequency dependent behavior [Peláiz-Barranco et al., 2013]. The perovskite structure of relaxor ferroelectrics is disordered, whereas that of typical ferroelectrics is ordered. Atoms are divided into two sizes (large and small sizes). Small ions have a limited range of motion in normal ferroelectrics. Small ions, on the other hand, have bigger space to move within the structure of relaxor ferroelectrics. Because big ions force the lattice frame to open. Relaxor ferroelectrics are advantageous for memory device applications because of the movement of small ions [Uchino, 2010].

2.5. PNN-PZT Composition

The general formula of lead nickel niobate ($Pb(Ni_{1/3}Nb_{2/3})O_3$-PNN) is a member of the lead containing complex perovskite group. The structure of this material is perovskite, and it has typical relaxor ferroelectric characteristics. Dielectric constant and Curie temperature of the PNN are highly dependent of the frequency. Since its discovery by Smolenskii and Agranovskaya in 1958, it has been examined by a number of researchers. The mixed-oxide method failed to produce the pure perovskite phase of PNN, as Agranovskaya reported in 1960. The presence of the pyrochlore phase causes dielectric characteristics of PNN to decrease. Swartz and Shrou reported a columbite precursor method to fabricate pyrochlore-free $Pb(Mg_{1/3}Nb_{2/3})O_3$. First step of the method is the preparation of the columbite precursor $MgNb_2O_6$, followed by the reaction between $MgNb_2O_6$ and PbO. The production of the pyrochlore phase can be avoided using this method. Veitch and Sharama used columbite $NiNb_2O_6$ to prepare PNN in a similar method [Lu and Hwang, 1995], [Vittayakorn et al., 2004]. Many piezoelectric ceramic materials with high dielectric permittivities have been developed from binary systems having a mix of relaxor-normal ferroelectric materials. Luff et al. reported solid solution in the $Pb(Ni_{1/3}Nb_{2/3})O_3$-$PbZrO_3$-$PbTiO_3$ ternary system in 1974 and discovered excellent piezoelectric properties at $0.5Pb(Ni_{1/3}Nb_{2/3})O_3$-$0.35PbTiO_3$-$0.15PbZrO_3$. Phase diagram of PNN-PZT system is shown in Figure 2.11 [Bove et al., 2001].

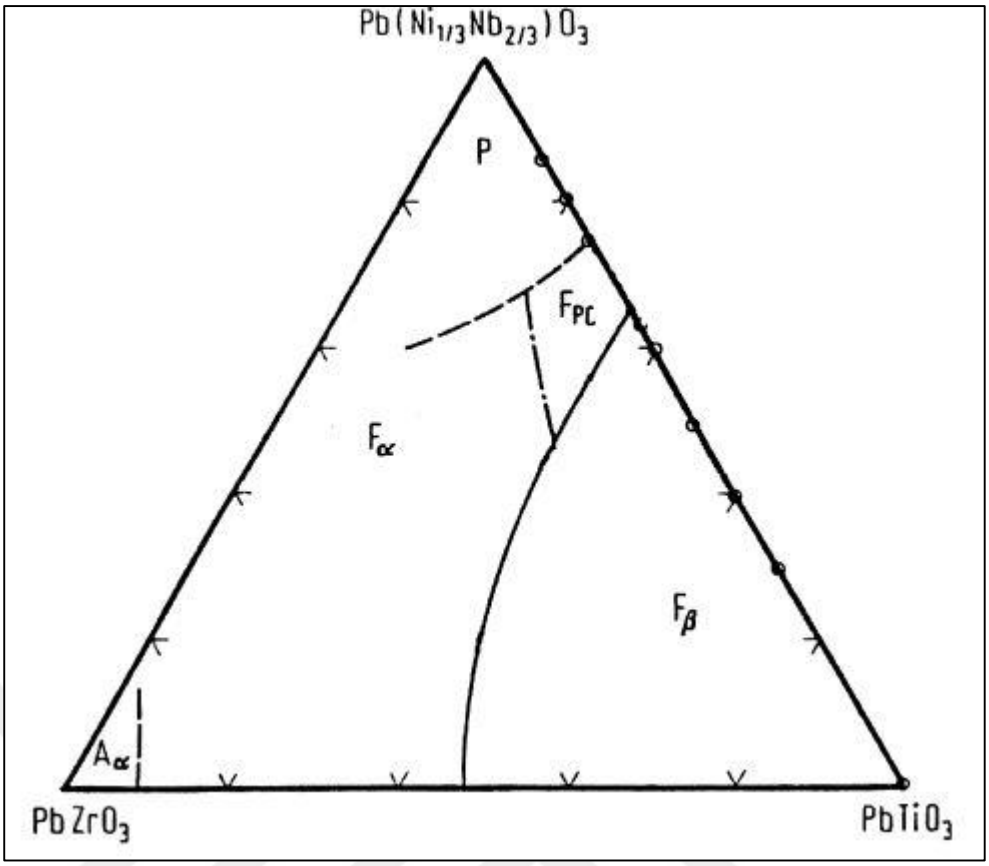

Figure 2.11: Phase diagram of PNN-PZT system. F_α: rhombohedral phase, F_β: tetragonal phase, F_{PC}: pseudo cubic phase, P: cubic paraelectric phase, A_α: antiferroelectric phase.

Solid solution of PNN-PZT was synthesised by Singh et al. The columbite method was used to synthesize powder. They sintered the ceramics at different heating rates for 4 h holding and effects of heating rate on electromechanical properties were studied. They reported when heating rate was 8 °C/min from room temperature to 900 °C and holding for 4 h at 1280 °C, highest relative permittivity and piezoelectric charge constant were observed. They reported pyrochlore-free perovskite phase with the XRD results. They reported the composition can be used for actuator applications [Singh et al., 2007].

Majahan et al. investigated the effect of different sintering temperature on the structural and piezoelectric properties of PNN-PZT. The mixed oxide method was used to synthesize powder. They obtained a high coupling factor of 0.67 and the piezoelectric charge coefficient of 750 pm/V.

The maximum strain was reported ~ 0.21 at 40 kV/cm applied field for ceramic sintered at 1100℃. They reported the composition can be used for actuator and actuator applications [Mahajan et al., 2007].

Pann et al. used to mixed oxied method to synthesize PNN-PZT. They reported the parameters of sintered was 1150℃ for 2.They reported dielectric and ferroelectric properties of PNN-PZT composition [Pan and Zhang, 2007].

Du et al. investigated the effects of Fe_2O_3 doping on the microstructure and piezoelectric properties of 0.5PNN-0.45PZT ceramics. They added different concentration of Fe_2O_3 as 0.0, 0.8, 1.2, 1.6 mol%. They obtained pure perovskite phase. They reported that the density and grain size of Fe-doped ceramics increase slightly as the concentration of Fe_2O_3 increases. They reported the piezoelectric constant as d_{33} ~956 pC/N, the electromechanical coupling factor k_p as 0.74 and the dielectric constant ε_r as 6095 for 1.2 mol% Fe_2O_3 doping ceramic [Du et al., 2012].

Kang et al. investigated the piezoelectric properties of 0.55PNN-0.45PZT with different amount of MnO_2 where as 0.0, 0.25, 0.5, 1.0, 2.0, 3.0 mol%. They reported Q_m and Young's modulus of composition increased with MnO_2 doing due to the oxygen vacancies created by the MnO_2. They obtained optimum dielectric and electromechanical properties by doping MnO_2 of 0.5–1 mol% [Kang and Kang, 2019].

Wang et al. investigated the effect of Ta doping with different amounts (0.0-0.7 mol%) for 0.55PNN-0.45PZT composition. They observed rhombohedral-tetragonal morphotropic phase boundary for 0.5 mol% Ta doping. And they also obtained better electrical properties. They stated that this composition can be suitable for micro-displacement actuator applications [Wang et al., 2021].

Peng et al. investigated the effect of CeO_2 and Sm_2O_3 doping on PNN-PZT ceramic composition. When they compared to undoped ceramics, the relaxation behavior of Sm_2O_3 doped ceramics was smaller, the Curie temperature reduced, and the electric characteristics were bad. The relaxation behavior of ceramics doped with CeO_2 was obvious, indicating that the dielectric relaxation behavior of ceramics improved, while the Curie temperature increased and dielectric loss decreased. Furthermore, CeO_2 doped ceramics exhibited the best electric characteristics. It was discovered that adding CeO_2 to ceramics improves their characteristics [Peng et al., 2017].

To prepare 0.55PNN-0.45PZT relaxor-ferroelectric ceramics, Du et al. used a standard solid-state sintering process with CuO as a sintering aid. With increasing amounts of CuO added, the grain size and density of these specimens rose marginally. The addition of 0.4 wt.% CuO resulted in the best piezoelectric, dielectric, and ferroelectric characteristics [Du et al., 2015].

Studies in the literature about PNN-PZT composition are given in the Table 2.1.

Table 2.1: Electrical and electromechanical properties of PNN-PZT ceramics studied in the literature.

Composition	**Type of Doping**	**d_{33}**	**k_p**	**ε_r**	**T_c**	**Q_m**	**Reference**
0.25PNN-0.75PZT	PGO (1 wt %)	387	*	2331	*	*	Kim et al.
0.35PNN -0.65PZT	$LiBiO_2$-CuO (0.1 wt %)	538	0.62	3381	*	61	Yi et al.
0.55PNN - 0.45PZT	*	986	0.634	9015	115	36	Gao et al.
PNN-PZT	CeO_2-Sm_2O_3 (0.4 wt %)	700-620	0.62-	5300-	151-	*	Peng et al.
0.5PNN - 0.5PZT	*	612	0.54	5950	*	73	Singh et al.
0.55PNN-0.45PZT	Li_2CO_3 (2 mol %)	936	0.701	*	117	*	Pu et al.
0.55PNN - 0.45PZT	MnO_2 (1mol %)	710	0.595	3092	133	176	Liu et al.
PSNN-PZT	Sr (0.06 mol %)	*	*	6316.41	71.65	*	Butnoi et al.
PNN-PZT	*	750	0.67	*	*	*	Mahajan et al.
0.5PNN - 0.5PZT	Sm_2O_3 (0.6 wt %)	688	0.579	6260	110	*	Cheng et al.
0.55PNN - 0.45PZT	*	887	0.621	8763	*	31	Yue et al.
PNN-PZT	Sb_2O_3 and Ta_2O_5 (0.02	1001	0.67	8534	110	*	Chen et al.

Continuation of Table 2.1.

Composition	**Type of Doping**	**d_{33}**	**k_p**	**ε_r**	**T_c**	**Q_m**	**Reference**
0.5PNN - 0.5PZT	*	780	0.6	6180	*	*	Zhu et al.
0.55PNN - 0.45PZT	CuO (0.4 wt %)	777	0.55	7365	*	*	Du et al.
0.35PNN - 0.65PZT	$0.5PbO\text{-}0.5B_2O_3$ glass	479	0.55	2904	*	79	Y1 et al.
0.5PNN - 0.5PZT	*	710	0.67	5480	*	*	Mahajan et al.
0.38PNN-0.62PZT	*	825	0.61	4244	*	59	Nie et al.
0.55PNN - 0.45PZT	MnO_2 (0.25 mol %)	592	0.27	3772.38	*	51	Kang et al.
0.5PNN - 0.5PZT	*	*	*	22388	141.4	*	Pan et al.
0.55PNN - 0.45PZT	Fe_2O_3 (1.2 mol %)	956	0.74	6095	108	*	Du et al.
0.25PNN-0.75PZT	$BiFeO_3\text{-}Ba(Cu_{0,5}W_{0.5})O_3$	*	*	4091	*	*	Chu et al.
0.55PNN - 0.45PZT	Sn (8 mol %)	*	*	12900	79	*	Sutjarittangtham et al.

2.6. Piezoelectric Ceramic Fiber Production

For actuators and transducers applications, piezoelectric ceramics have been widely used. In polycrystalline materials, electric field induced strain are generally less than 0.1 % and in some single crystals are limited to 1%. Different types of actuators, such as the rainbow, moonie, and thunder, have been created to increase the magnitude of this little displacement. The fiber form of piezoelectric materials is highly beneficial for a actuator applications [Yoon et al., 2006], [Mensur-Alkoy, 2015]. Piezoelectric ceramics in fiber form are used because of their anisotropic characteristics, improved flexibility and strength [Alkoy et al., 2012], [Mensur Alkoy et al., 2011]. Extrusion, viscous suspension spinning process (VSSP), and the sol–gel method are the three main methods for producing piezoceramic fibers. The green fiber precursors employed and how the green fibers are formed prior to sintering are the main diffirences between these methods. Variations in processing conditions can cause variances in fiber form and microstructure, which can affect the mechanical and electrical qualities of the final products. In addition to these methods, the alginate gelation method is another excellent way for producing ceramic fibers. Alkoy et al. were the first to reported this method, which contain extrusion and gelation of a sodium alginate based slurry [Alkoy et al., 2006].

Sodium (Na) alginate[$(C_5H_7O_4COONa)_x \bullet yH_2O$] is an anionic polysaccharide obtained from brown seaweed. In the existence of divalent cations such as calcium (Ca^{+2}), sodium alginate gels at room temperature by forming a three-dimensional network structure, as shown in Figure 2.12, as a result of the displacement of Na^+ with the divalent cation [Draget et al.,2005].

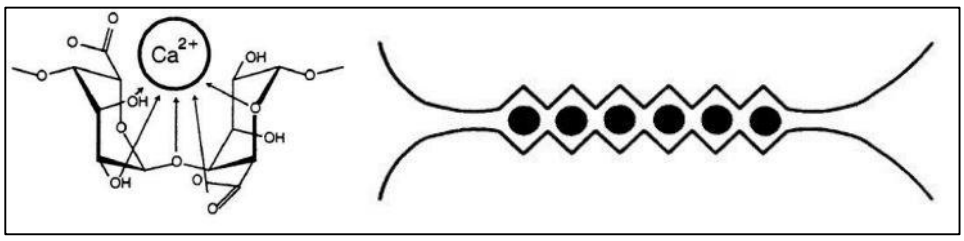

Figure 2.12: Gelation and stereochemical structure of the GG dimer block.

2.7. Electroceramic Composite

Piezocomposites are formed by the combination of an active and a passive polymer matrix [Mensur-Alkoy et al., 2019]. For reasons such as high pressure tolerance, high hydrostatic sensitivity, and good acoustic impedance matching with water, researchers have been studying piezocomposites in underwater transducer and sensor applications for many years. Piezocomposites were classified according to the connectivity of the individual phases by Newman et al. [Mensur-Alkoy et al., 2019], [Kaya, 2018]. Because physical properties can change by several orders of magnitude depending on how connections are created, connectivity is an important factor in property development in multiphase solids [Newnham et al., 1978].

0-0, 0-1, 0-2, 0-3, 1-1, 1-2, 2-2, 1-3, 2-3, and 3-3 are the globally approved denonatation for piezocomposites. The number of connection dimensions for the piezoelectrically active phase is represented by the first digit, while the electromechanically inactive polymer phase is represented by the second digit [Akdogan et al., 2005]. Ten different connectivity patterns are seen in Figure 2.13. [Islam and Priya, 2012].

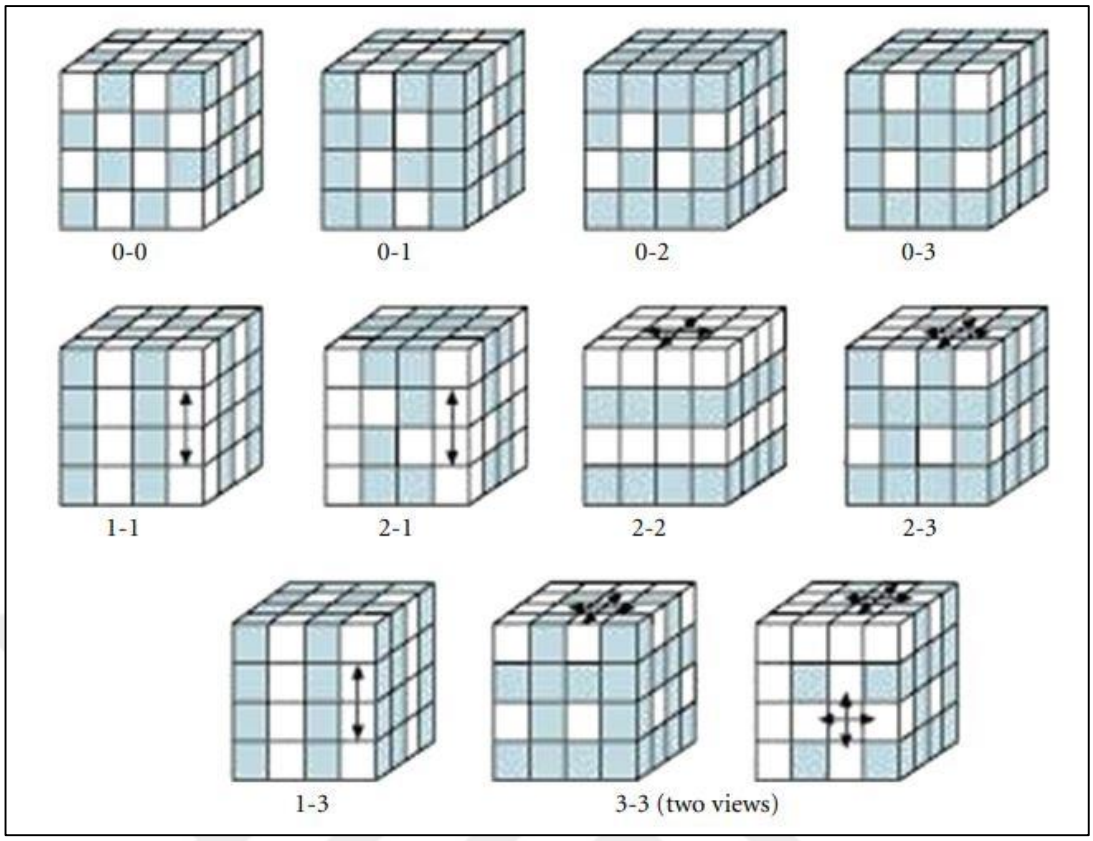

Figure 2.13: Different connectivity types for composites.

Figure 2.14 describes a 1-3 connected piezocomposite that is widely used. Because of their excellent piezoelectric capabilities as an active ceramic phase, PZT fibers are frequently utilized for 1-3 piezocomposites [Özyazıcı, 2018].

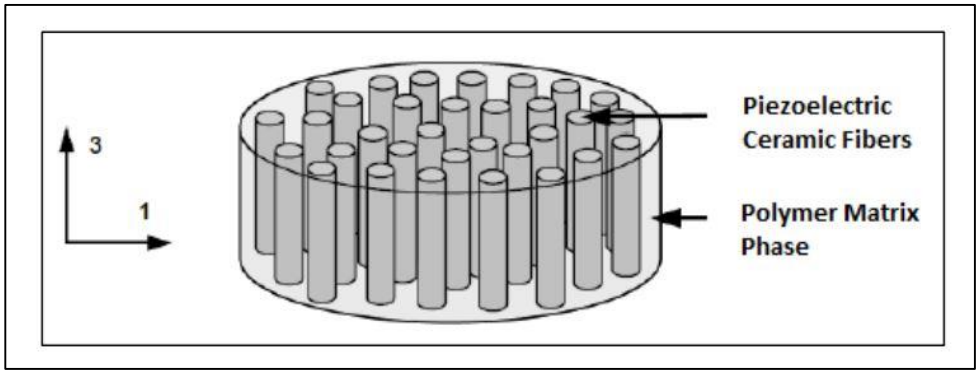

Figure 2.14: Schematic representation of 1-3 connectivity in piezecomposite.

3. EXPERIMENTAL STUDY

3.1. Synthesis of the PNN-PZT Ceramic Powders

In this study, lead oxide (PbO), zirconium oxide (ZrO_2), titanium dioxide (TiO_2), niobium penta oxide (Nb_2O_5) and nickel oxide (NiO) powders were used as the sources for the synthesis of the PNN-PZT ceramic composition. In this content, undoped and 0.5%, 1.0%, 1.5% Nd, Fe, Mn doped PNN-PZT powders were produced. The purity and mark of the powders are given in Table 3.1. The flowchart of the powder fabrication is given in Figure 3.1.

Table 3.1: Information about oxide powders.

Source of Oxide Powder	**Purity**	**Mark**
PbO	99.9 %	Alfa Aesar
ZrO_2	99+ %	Alfa Aesar
TiO_2	99.5%	Alfa Aesar
NiO	99%	Alfa Aesar
Nb_2O_5	99.5%	Alfa Aesar
Nd_2O_3	99%	Alfa Aesar
Fe_2O_3	99%	Alfa Aesar
MnO_2	99.9%	Alfa Aesar

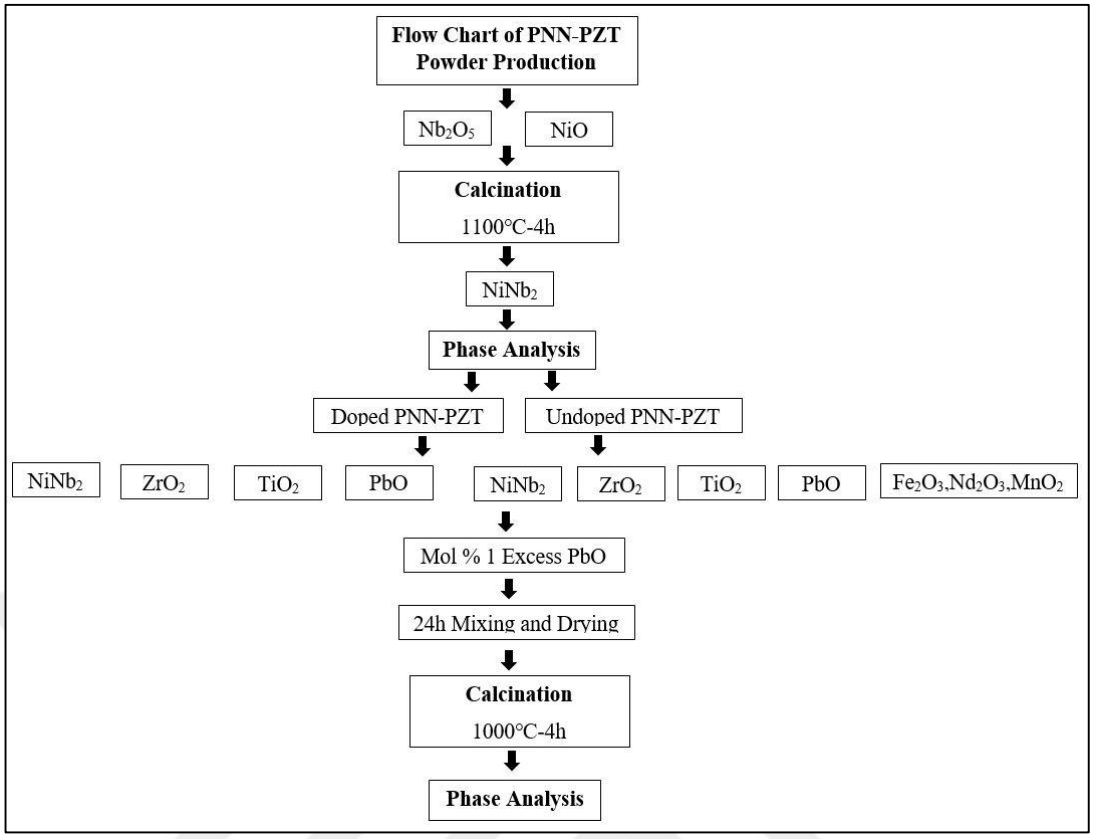

Figure 3.1: The flowchart of the powder fabrication.

Ceramic powder synthesis was completed in two steps by conventional solid state reaction method. Firstly, $NiNb_2O_6$ precursor powder was produced in order to synthesis of PNN-PZT ceramic composition. The synthesis of compounds such as $NiNb_2O_6$ as a first step is called the Columbite or Woflramite method [Kaya M.Y., 2018]. By using this method, it is aimed to prevent the formation of pyrochlore phase in the structure. In this content, NiO and Nb_2O_5 powders were mixed in a 1:1 stoichiometric ratio. After NiO and Nb_2O_5 powders are weighed, they were mixed using ytria stabilized zirconia (YSZ) balls of 3-5 mm diameter and ethanol in a ball mill (MSE) at 150 rpm for 24 hours. At the end of this time, the mixture was taken into a glass beaker and dried in a heated magnetic stirrer at 70°C using 150 rpm. After drying, the mixture was kept in the oven (BINDER-120) for 24 hours at 80°C. After that, the mixture was placed in an alumina crucible and kept in the oven (Nabertherm) at 5°C/min heating regime at 1100°C for 4 hours, finally, nickel niobate ($NiNb_2O_6$) precursor powder was obtained. After $NiNb_2O_6$ was obtained, $NiNb_2O_6$, PbO, ZrO_2 and TiO_2 powders were mixed to synthesize powder composition stoichiometric $0.5[Pb(Ni_{1/3}Nb_{2/3})O_3.0.5Pb(Zr_{0.3}\ Ti_{0.7})O_3]$. In order to produce doped PNN-PZT, 0.5

%, 1.0 % and 1.5 mol% Fe_2O_3, MnO_2, Nd_2O_3 powders were added at this step. In order to compensate the lead loss during sintering, 1 mol% PbO (99.9% Alpha Aesar) was added to this mixture. Powders were mixed using 3-5 mm diameter YSZ balls in ethanol media at 150 rpm for 24 hours. Then the mixture was taken into a glass beaker and dried at 70°C in a magnetic stirrer. After drying, the mixture was kept in the drying oven (BINDER-120) for 24 hours at 80°C. After that, the powder mixture was placed to the alumina crucible and annealed in the furnace (MSE) 5°C/min heating regime at 1000°C for 4 hours. Doped and undoped PNN-PZT powders were fabricated wit the same way. After the powder synthesis, the phase analysis of the powders was done by X-ray diffraction (XRD) (Rigaku D-MAX 2200-Japan) with a scanning speed of 2θ=20°-70° (in 0.02°steps).

3.2. Synthesis of the PNN-PZT Ceramics

Undoped and doped PNN-PZT ceramic powders, binder solution all chemicals were given Table 3.2 as 7.0 wt % of these powders, methyl ethyl ketone (MEK-Merck) and YSZ balls were ball-milled for 24 hours.

Table 3.2: The used chemicals of the binder solution.

Chemicals	**Mark**
Polyvinyl Butyral-PVB B-92	Sigma
Bnzyl Butyl Phthalate-BBP	Alfa Aesar
Polyethylene Glycol 400-PEG400	Alfa Aesar
Ethanol	Merck
Methyl Ethyl Ketone	Merck

After drying at the magnetic stirrer, the ceramic powder mixture was ground in a mortar and sieved using an ASTM 90 μm sieve. After syntehesis of doped and undoped PNN-PZT ceramic powders, bulk ceramics were formed by uniaxial pressing using 100MPa pressure for 2 minutes. Then, all ceramics were sintered at 1200 °C for 4 hours. Sintering processing of all compositions were carried out at the same temperature and time in a lead-rich atmosphere and using a covered alumina crucible. The picture of bulk ceramics is shown in Figure 3.2.

Figure 3.2: The picture of uncoated and silver electrode coated bulk ceramics.

3.3. Synthesis of Fibers

In this part, the preparation of the ceramic slurry, the drawing of the fibers and the experimental studies of the production of 1-3 piezocomposites consisting of these fibers are explained. PNN-PZT ceramic powders were used to prepare fiber by alginate gelation method. For preparation of the slurry, in addition to PNN-PZT ceramic powders, distilled water, sodium alginic acid (Sigma Aldrich), glycerol (Merck) as plasticizer, darvan 821A (MSE) as dispersant and surfyanol (Air Products and Chemicals) as defoamer were used. In the Table 3.3 raw materials and their amount were reported.

Table 3.3: The raw materials used in the preparation of slurry and their weights.

Component	**Amount(g)**
PNN-PZT Powder	64.6232
Distilled Water	32.3116
Alginic Acid	1.5057
Glycerol	1.2931
Surfyanol	0.041
Darvan	1.2931

Glycerol, distilled water, darvan 821A and surfyanol, were ball milled using 3-5mm diameter YSZ balls at 150 rpm for 15 minutes. Then calcined PNN-PZT ceramic powder was also added to the this mixture. After adding ceramic powder, the mixture was ball milled at 150 rpm for 4 hours. At the end of this process, the slurry was taken into a glass beaker and the slurry was mixed in the mechanical mixer at a temperature of 75°C. While mixing the slurry, sodium alginic acid was also added slowly into the slurry. Process was supported by the addition of 30-50 ml of distilled water for homogeneous mixing of sodium alginic acid. The mixing and heating process of the slurry continued until the slurry reached desired viscosity. After reaching the desired viscosity, the slurry was filled into the injector and the fibers were drawn with the fiber drawing machine given in the Figure 3.3 [Özyazıcı, 2018]. Calcium chlorate dihydrate($CaCl_2$)(Merck) solution is used to complete alginate gelation process and the solution contains salt and 30g/L distilled water.

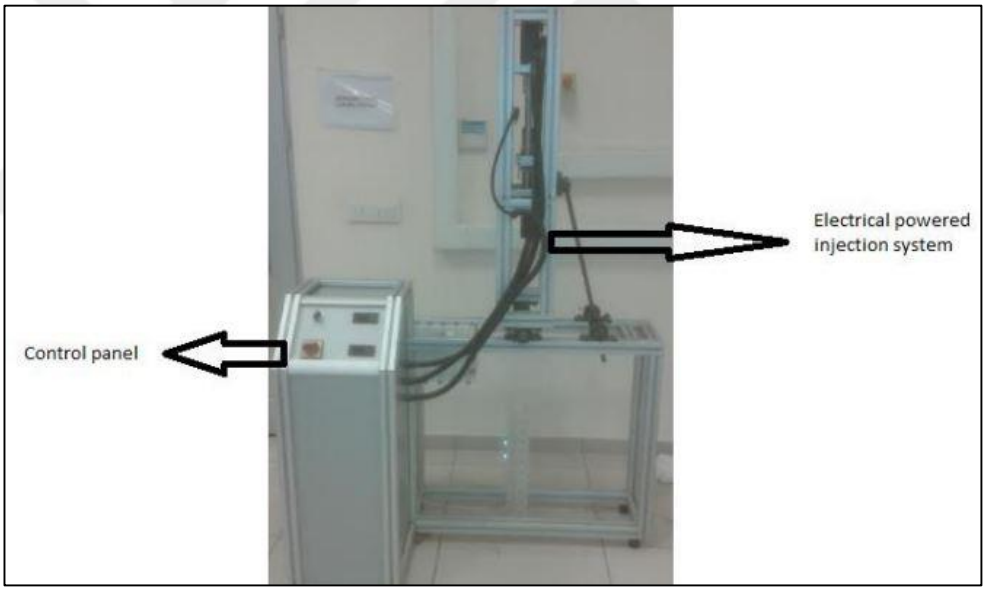

Figure 3.3: Fiber drawing machine.

In this solution, substition of Na^+ ions with Ca^{2+} ions occurs, crosslinks between Ca^{2+} ions form and strengthened green body occur. [Özyazıcı, 2018]. Green fibers were drawn into this solution and they were kept for 24 hours. After this time, the fibers were hanged and dried. After drying, the fibers were cut into 5 cm lengths. 5 cm long fibers were placed in batches of 40 in alumina crucibles for further sintering. The sintering of the green fibers was carried out in the furnace (MSE) at 1200°C for 4 hours with a heating regime of 5°/min. In order to prevent PbO loss due to high temperature

and create a PbO rich atmosphere, atmospheric powder consisting of PbO and ZrO_2 powder mixture was put into the crucible. In order to produce 1-3 PNN-PZT piezocomposite a metal mesh was used to arrange the fibers into orderly arrays. Polyurethane (Biresin U1419,SikaAxson) with a hardness of Shore A98 was used as a matrix phase. Figure 3.4 shows the pictures of from one fiber to 1-3 piezocomposite.

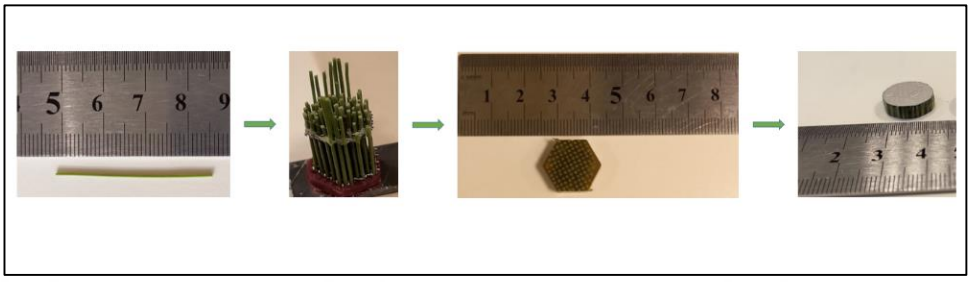

Figure 3.4: Flowchart of the pictures of from one fiber to composite.

3.4. Structural and Electrical Analysis

Phase analyses of the all ceramics such as powder, bulk were performed using X-ray diffraction (XRD) method. Analysis was performed using two different 2θ values, 20-70° and 43-47°. All microstructure analyses were performed using a Philips XL 30 SFEG scanning electron microscope(SEM). Before the microstructure analysis, thermal etching was applied to the all bulk ceramics at 1050 ℃ for 30 minutes in order to observe the grain and the grain boundaries.

In order to perform the electrical characterization of all doped and undoped PNN-PZT bulk ceramics, top and bottom surfaces of the ceramics were coated with silver electrodes(Arıteks Nanotek,0501-0100). The electrodes were fired at 700°C for 30 minutes. Silver (DAG 1415 air dry silver) paint was used as the electrode for the PNN-PZT piezocomposites (PLANO GmbH) because of the polyurethane. In order to characterize the electrical and electromechanical properties, dielectric loss, temperature dependence dielectric constant, polarization-electric field hysteresis measurements were carried out for all ceramics. All ceramics were poled for 10 minutes at room temperature (RT) by applying 25 kV/cm electric field. After the poling of the PNN-PZT piezocomposite and bulk ceramics, admittance measurements were done between 1kHz-1MHz frequency range. Measurements were performed in the air and underwater. Figure 3.5 shows the PNN-PZT piezocomposite and ceramic.

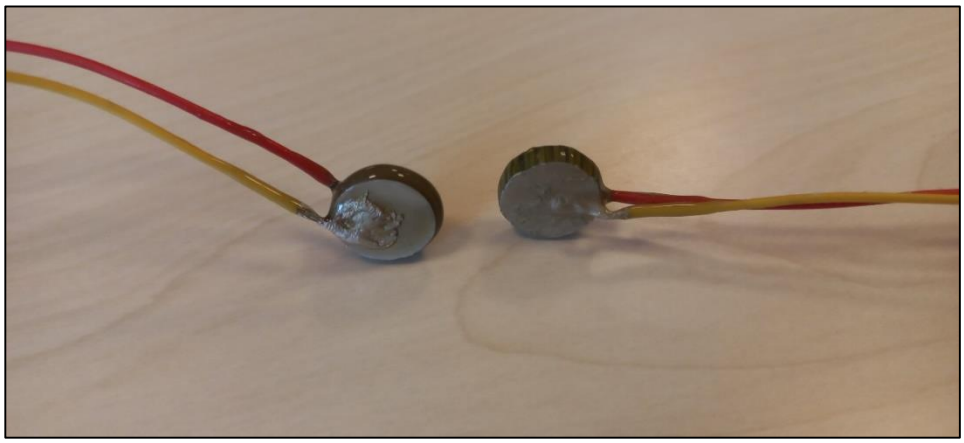

Figure 3.5: Picture of PNN-PZT piezocomposite and ceramic for underwater measurements.

4. RESULTS AND DISCUSSION

4.1. Phase Analysis of PNN-PZT Compositions

4.1.1. XRD Analysis of $NiNb_2O_6$ Powder

Firstly, nickel niobate ($NiNb_2O_6$) precursor powder was produced. The Figure 4.1 exhibits the XRD pattern of calcined $NiNb_2O_6$ powder at 1100°C for 4 hours. As seen from the XRD pattern, $NiNb_2O_6$ phase was obtained as desired and any secondary phase was not observed.

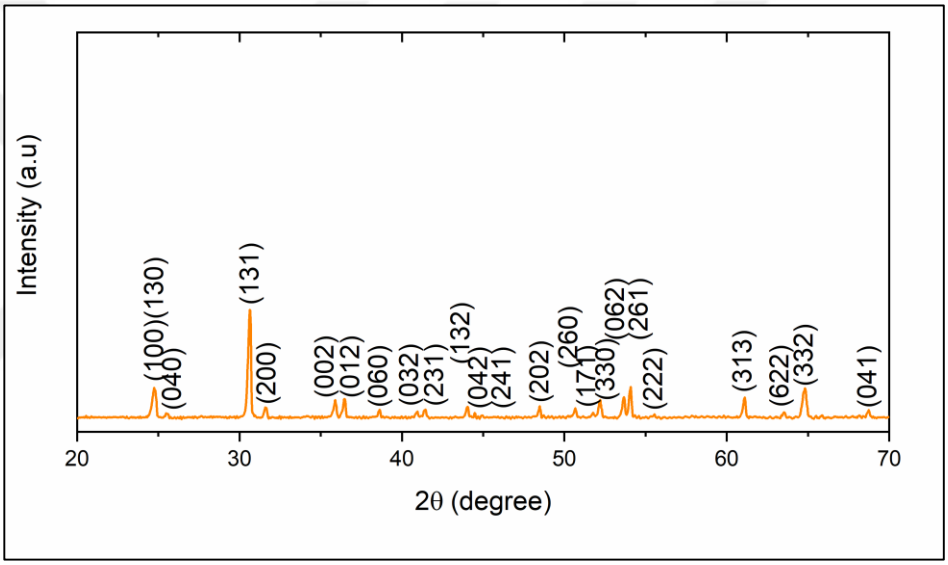

Figure 4.1: XRD pattern of the $NiNb_2O_6$ powder.

4.1.2. XRD Analysis of PNN-PZT Powders and Ceramics

Powder synthesis of doped and undoped PNN-PZT compositions were fabricated after $NiNb_2O_6$ was produced. XRD patterns of undoped and doped calcined and sintered PNN-PZT powders are given in Figure 4.2-Figure 4.7. Pure perovskite phase was obtained for each of undoped, Mn and Fe doped PNN-PZT after calcination. The comparison of XRD pattern of calcined and sintered undoped and Mn doped ceramics were given in Figure 4.2 and Figure 4.3 respectively. The same comparison was done for Fe doped samples and XRD patterns were given in Figure 4.4 and Figure 4.5. However, with the increasing amount of Nd doping, extra PbO peaks were

observed after calcination in the structure as seen in Figure 4.6. It was determined that the PbO peaks did not disappear after sintering as seen in Figure 4.7. This problem can be overcomed by changing the sintering parameters.

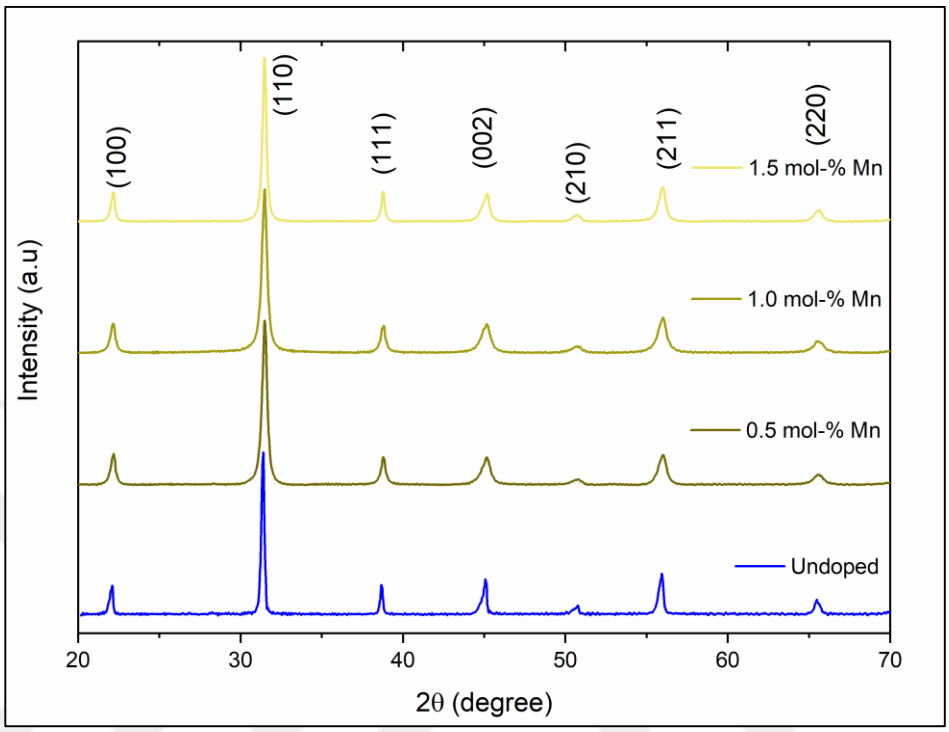

Figure 4.2: XRD pattern of calcined undoped and Mn doped powders.

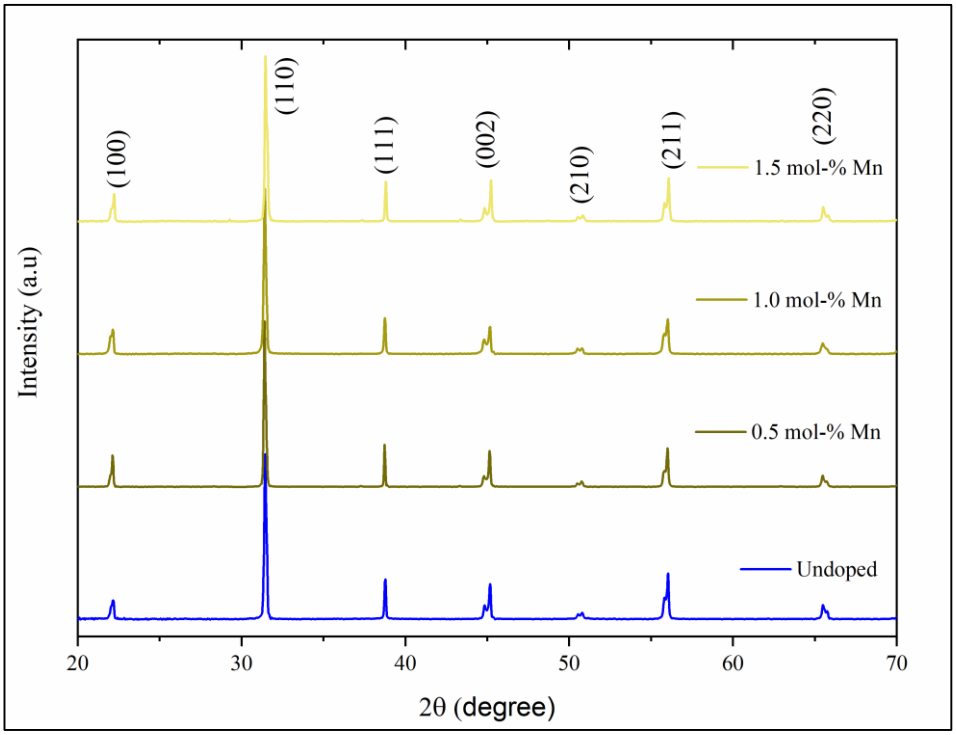

Figure 4.3: XRD pattern of sintered undoped and Mn doped ceramics.

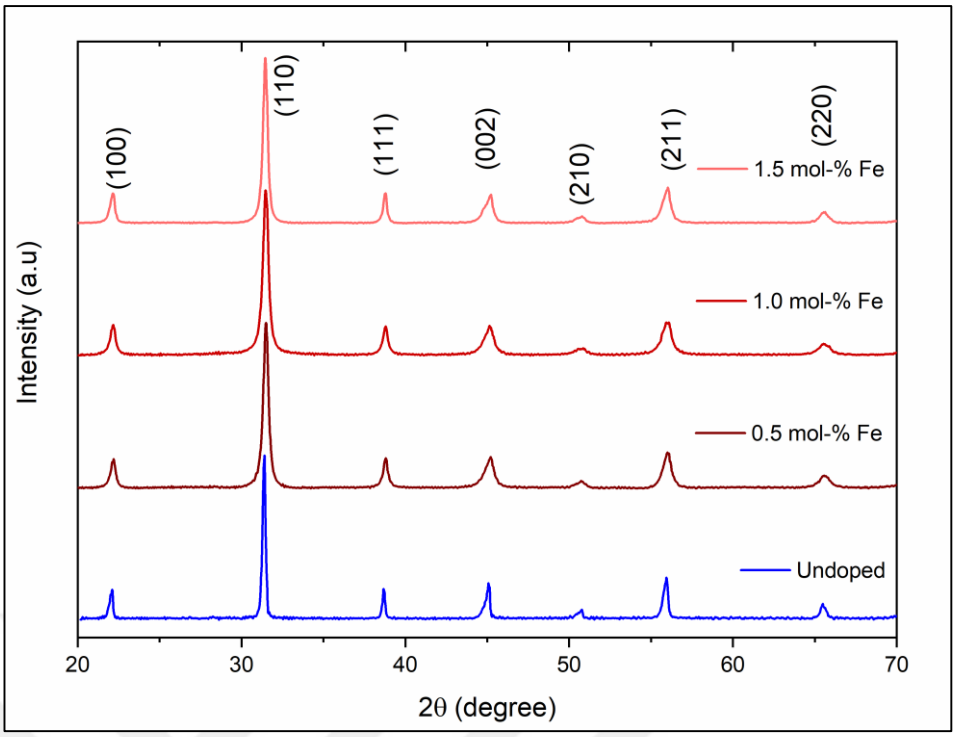

Figure 4.4: XRD pattern of calcined undoped and Fe doped powders.

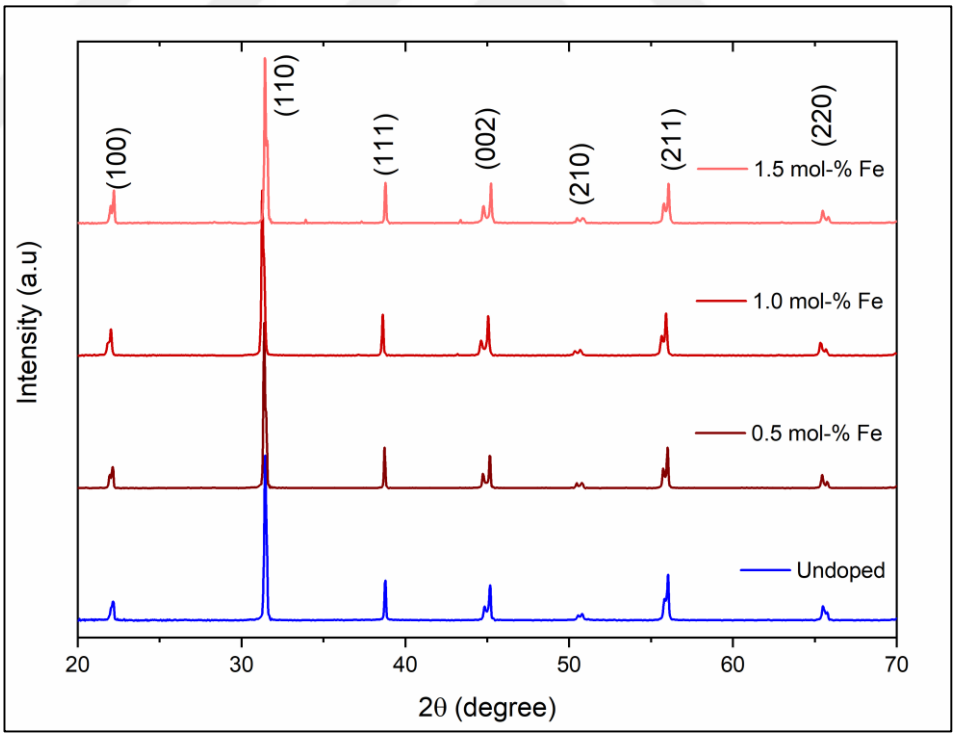

Figure 4.5: XRD pattern of sintered undoped and Fe doped ceramics.

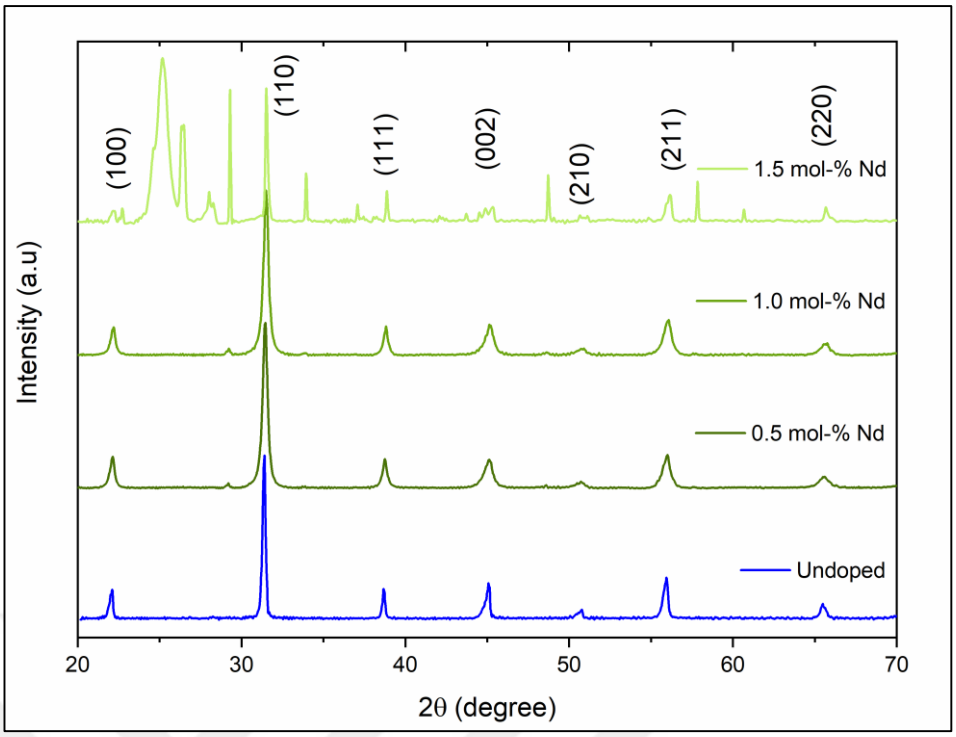

Figure 4.6: XRD pattern of calcined undoped and Nd doped powders.

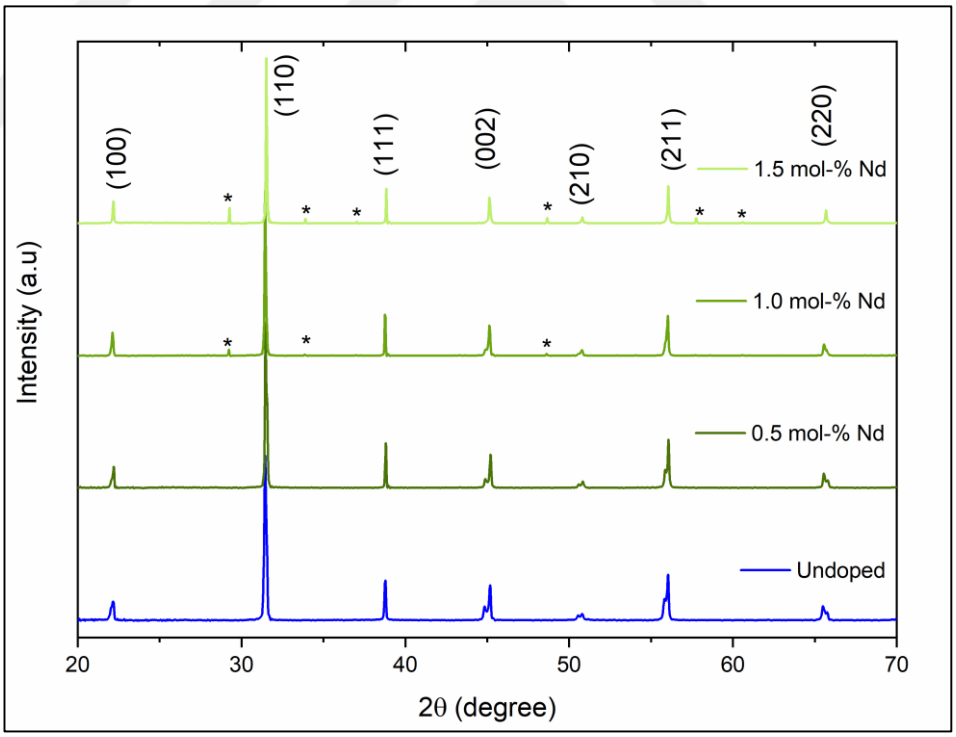

Figure 4.7: XRD pattern of sintered undoped and Nd doped ceramics.

Further investigation was done for using XRD peaks. After sintering, as seen in Figure 4.8, Figure 4.9 and Figure 4.10, a splitting was observed at (002)/(200) peaks located around 45° for doped and undoped ceramics. The reason of this splitting can

be lattice distortions generated by oxygen vacancies ($V_{ö}$) due to lead loss at 1200°C. Due to lattice distortions, shifts were observed in the XRD pattern because of the change of c/a ratios. This indicates that pseudo-cubic structure with eight polarization directions and a tetragonal structure with six polarization directions co-exist. Cheng et al. reported similar structure for 0.5PNN-0.5PZT+xSm composition. Kondo et al. reported Zr:Ti 30:70 ratio in the 0.5PNN-0.5PZT composition. It was reported that this composition was near to the morphotropic phase boundary and the tetragonal structure was richer. When the peaks around 45° were examined, it was observed that the intensities of the peaks were different in the doped and undoped ceramics.

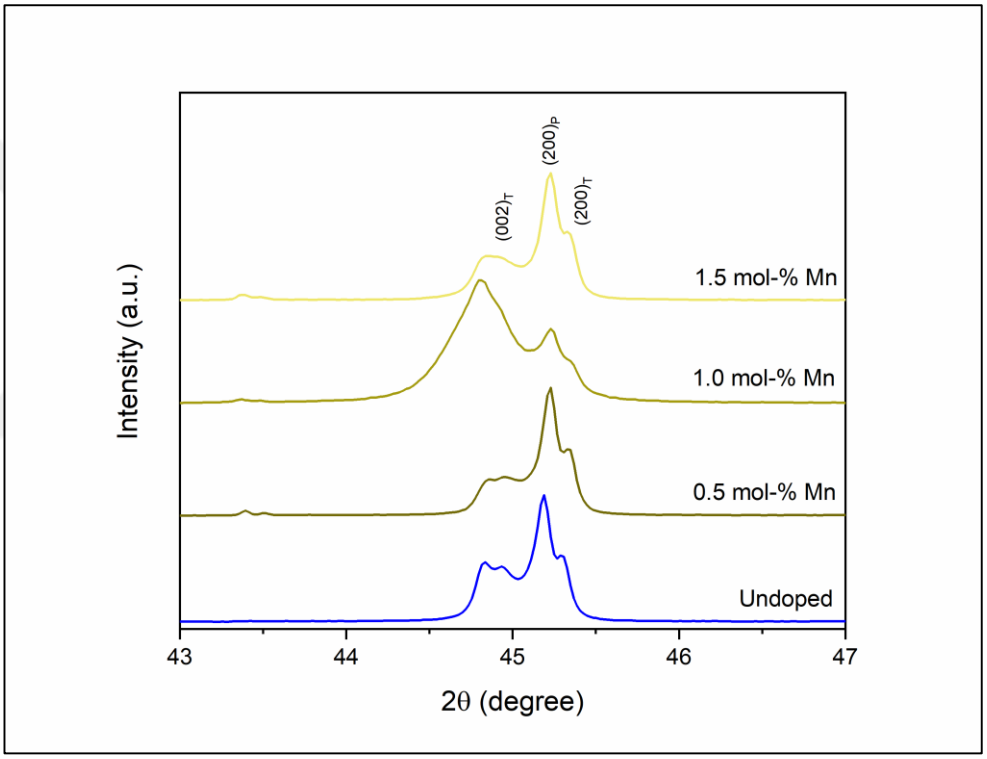

Figure 4.8: Comparison of the (002)/(200) peaks of undoped and Mn-doped ceramics in detail.

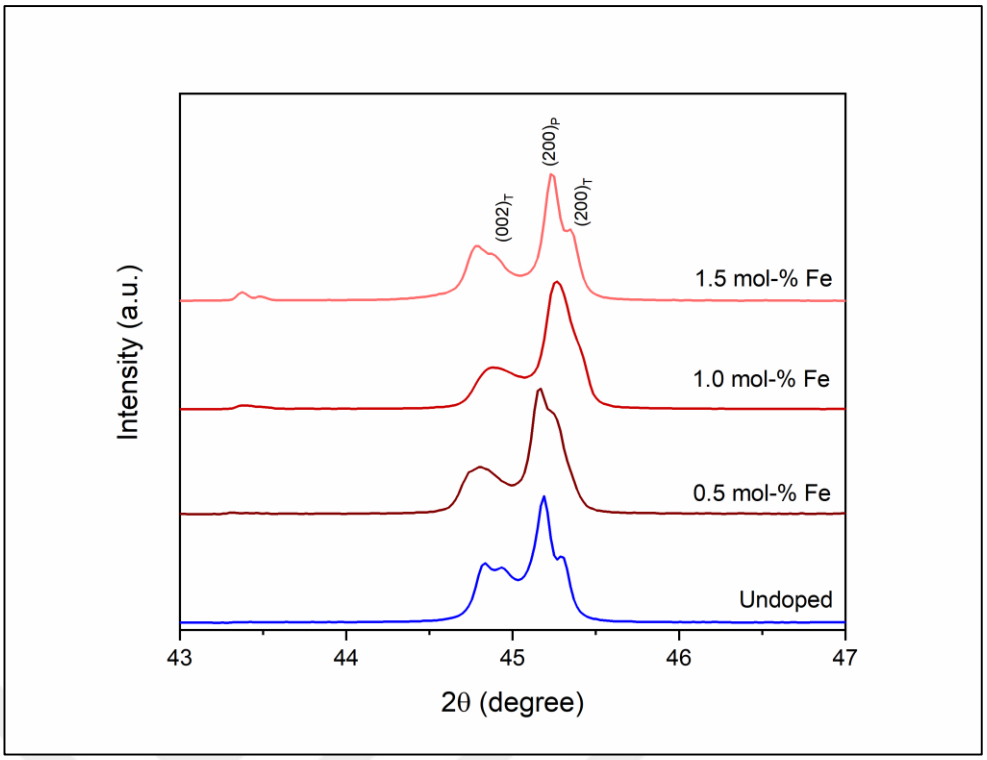

Figure 4.9: Comparison of the (002)/(200) peaks of undoped and Fe-doped ceramics in detail.

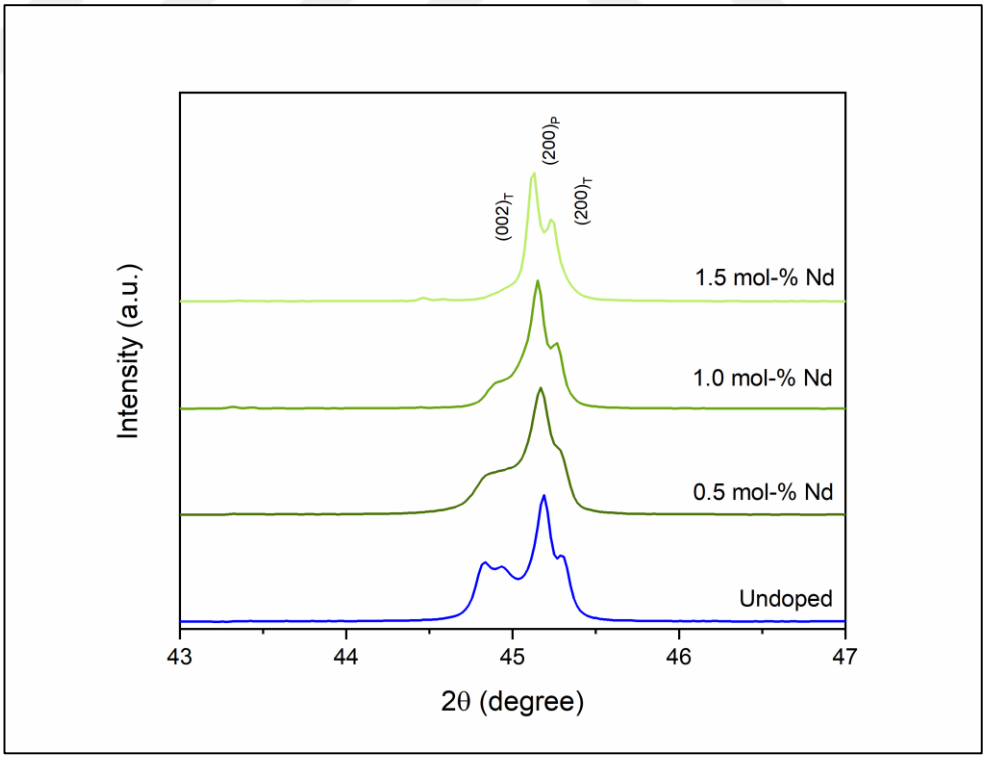

Figure 4.10: Comparison of the (002)/(200) peaks of undoped and Nd-doped ceramics in detail.

4.1.3. SEM Analysis of PNN-PZT Ceramics and Fibers

SEM image of undoped sintered PNN-PZT ceramic is shown in Figure 4.11. Homogeneous and dense structure was observed, bimodal grains were also observed. Average grain size was calculated as 1.7-1.9 μm.

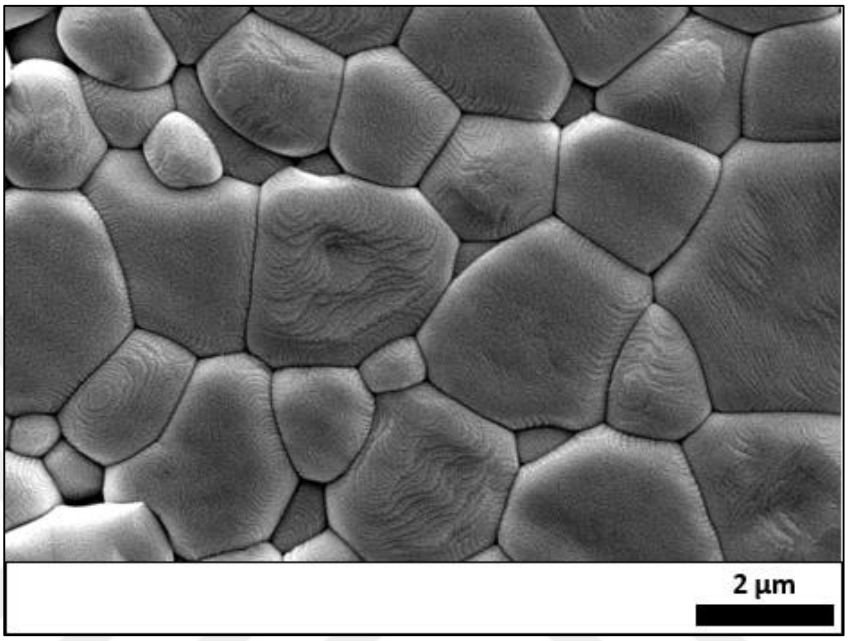

Figure 4.11: SEM micrograph of sintered PNN-PZT ceramic.

Figure 4.12 (a), Figure 4.12 (b) and Figure 4.12 (c) micrographs represent microstructures of 0.5 mol%, 1.0 mol%, 1.5 mol% Mn-doped ceramics. Micrographs for 0.5 mol%, 1.0 mol %, 1.5 mol% Fe-doped ceramics were also given in Figure 4.12 (d), Figure 4.12 (e), Figure 4.12 (g), respectively. Microstructures of Nd-doped ceramics were also seen in Figure 4.12.

Dense structure with almost no porosity was observed in all doped ceramics. Bimodal grains were observed due to the dopants and their ratios. To overcome for this problem, the sintering time and temperatures can be changed.

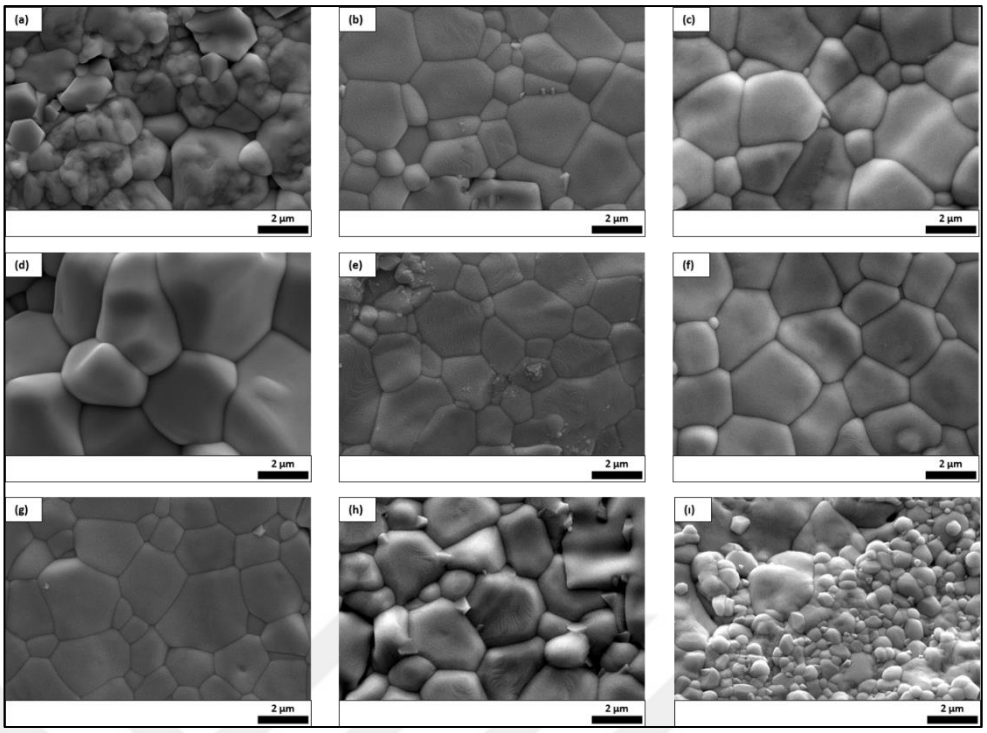

Figure 4.12: SEM micrographs of (a) 0.5% Mn, (b) 1.0% Mn, (c) 1.5% Mn, (d) 0.5% Fe, (e) 1.0% Fe, (f) 1.5% Fe, (g) 0.5% Nd, (h) 1.0% Nd (ı) 1.5% Nd doped ceramics.

PNN-PZT fibers were drawn using undoped PNN-PZT powders by alginate gelation method. Figure 4.13 illustrates the SEM micrograph of the fractured fiber surface with different magnifications. Figure 4.14 also shows the optic microscope images of the PNN-PZT piezocomposites. It is seen from SEM micrographs a dense structure was obtained for the PNN-PZT fibers. Diameters of fibers were measured as between 400-500 µm.

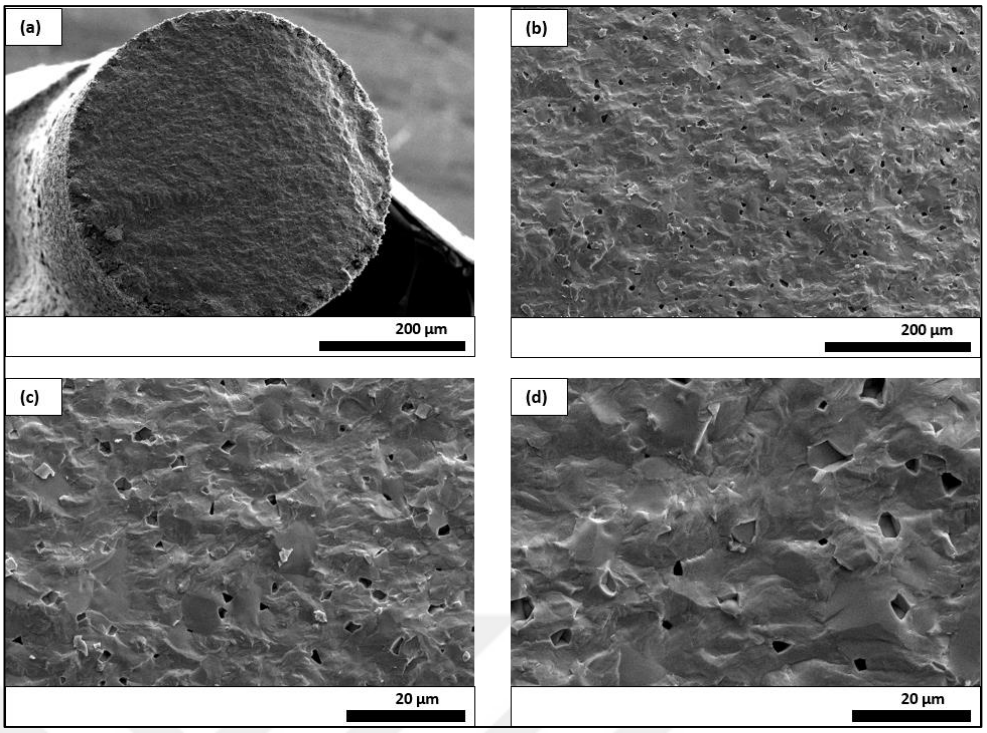

Figure 4.13: SEM micrographs of cross-sectional fiber surface
a) 125x b)500x c)1000x d)2000x.

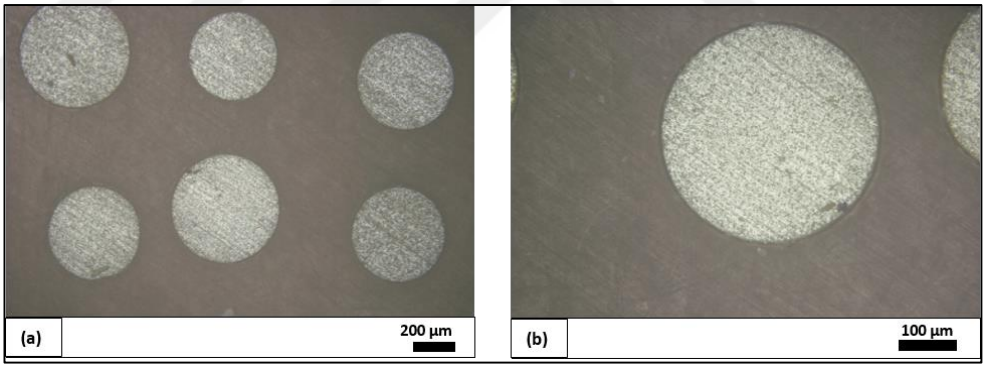

Figure 4.14: Optic microscope images of PNN-PZT piezocomposite
a)50x b)100x.

4.2. Electrical Measurement Results

4.2.1. Dielectric Measurements

Dielectric constant (ε_r) and loss tangent (tanδ) in terms of temperature and frequency for the undoped PNN-PZT ceramic were measured. The measurement was done at 1kHz, 10kHz and 100kHz frequency values as seen in Figure 4.15. The maximum dielectric permittivity (ε_{rmax}) for undoped PNN-PZT was measured at 143°C

and 1 kHz as 14697. The dielectric constant maximum changes with frequency. This is the relaxor nature of the PNN-PZT material. ε_r was found to be as 3067 at 1kHz at room temperature (RT). The loss tangent was measured 0.07 at 1 kHz, 0.13 at 10 kHz, and 0.06 at 100 kHz at RT.

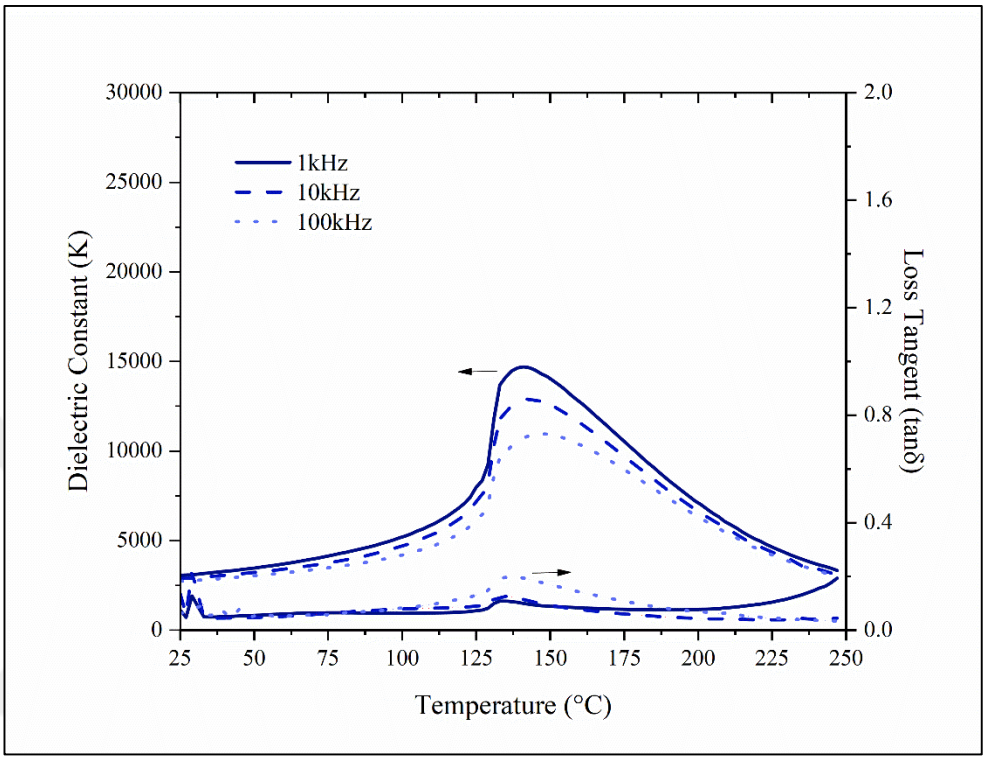

Figure 4.15: Temperature correlation of the dielectric constant and loss tangent of undoped ceramic.

The diffusive constant (γ) was found as 1.796 for undoped PNN-PZT ceramic at 100 kHz. When the diffusive constant is near to 2, it can be said that the ceramic composition shows the relaxor ferroelectric behavior [Kaya, 2018]. Figure 4.16 shows the determination of the diffusive constant for undoped PNN-PZT ceramic.

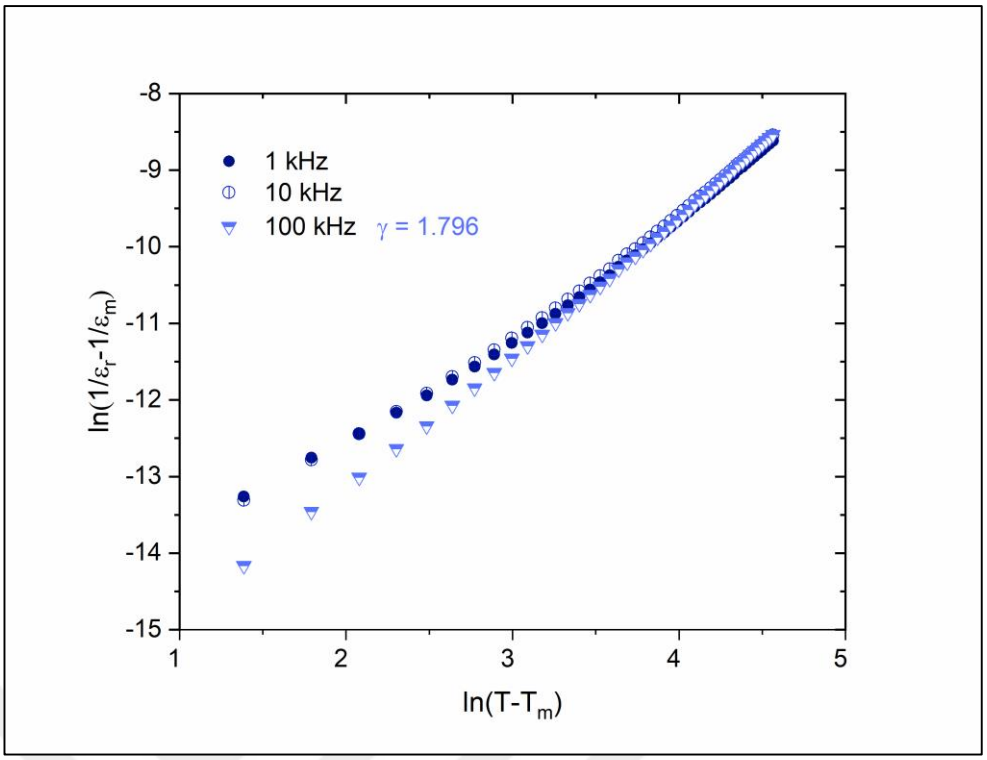

Figure 4.16: $\ln(1/\varepsilon_r-1/\varepsilon_m)$-ln $(T-T_m)$ relation for undoped ceramic.

The investigation and measurement of dielectric constant and tangent loss were done in terms of doping material. ε_r and tan(δ) values shown in Figure 4.17, 4.19, 4.21 were given in Table 4.1 and Figure 4.17, Figure 4.19, Figure 4.21 also shown Mn, Fe, and Nd with mol ratios, respectively.

Figure 4.18, Figure 4.20 and Figure 4.22 show temperature correlation of the dielectric constant and loss tangent of Mn doped, Fe doped and Nd doped ceramics at 1kHz, respectively.

Dielectric constant decreased with Mn and Fe doping whereas it increased with Nd doping. Curie temperature decreased with Nd doping however it increased with Mn and Fe doping at 100kHz.

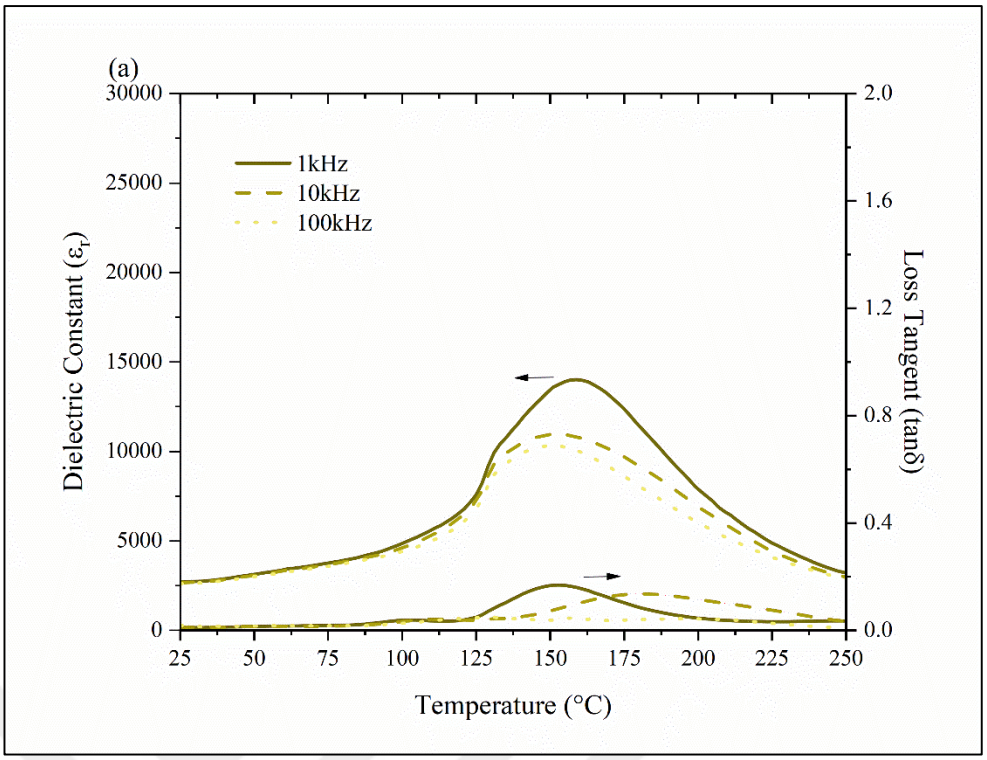
(a)
1kHz
10kHz
100kHz
Dielectric Constant (ε_r)
Loss Tangent (tanδ)
Temperature (°C)
30000
25000
20000
15000
10000
5000
0
2.0
1.6
1.2
0.8
0.4
0.0
25
50
75
100
125
150
175
200
225
250

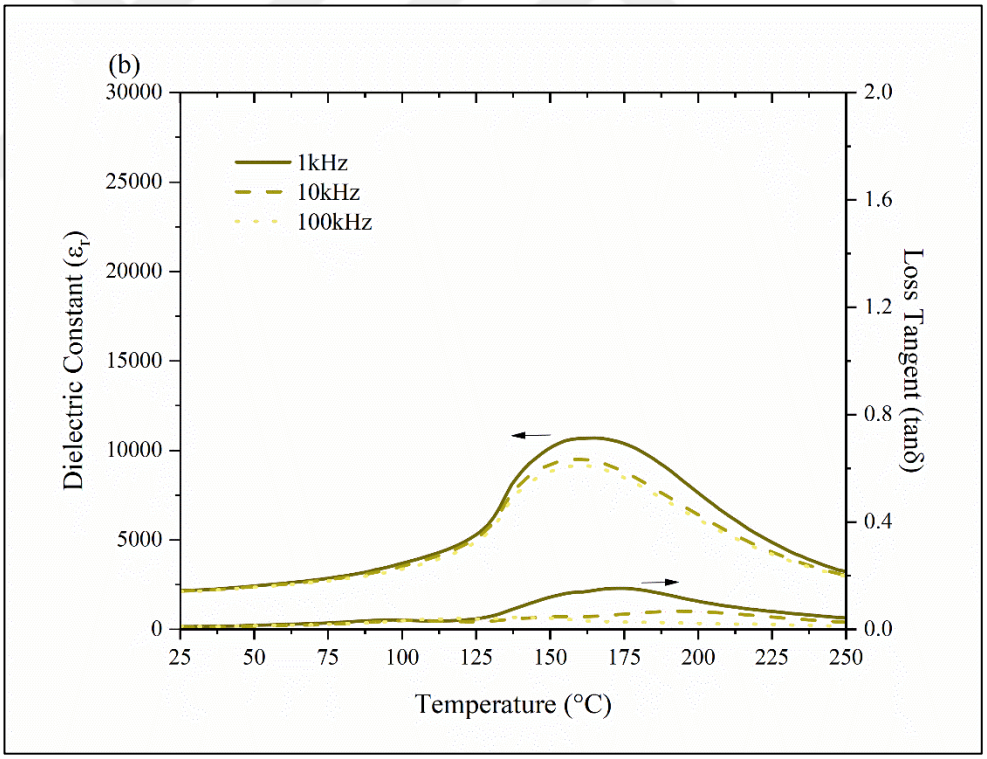
(b)
1kHz
10kHz
100kHz
Dielectric Constant (ε_r)
Loss Tangent (tanδ)
Temperature (°C)
30000
25000
20000
15000
10000
5000
0
2.0
1.6
1.2
0.8
0.4
0.0
25
50
75
100
125
150
175
200
225
250

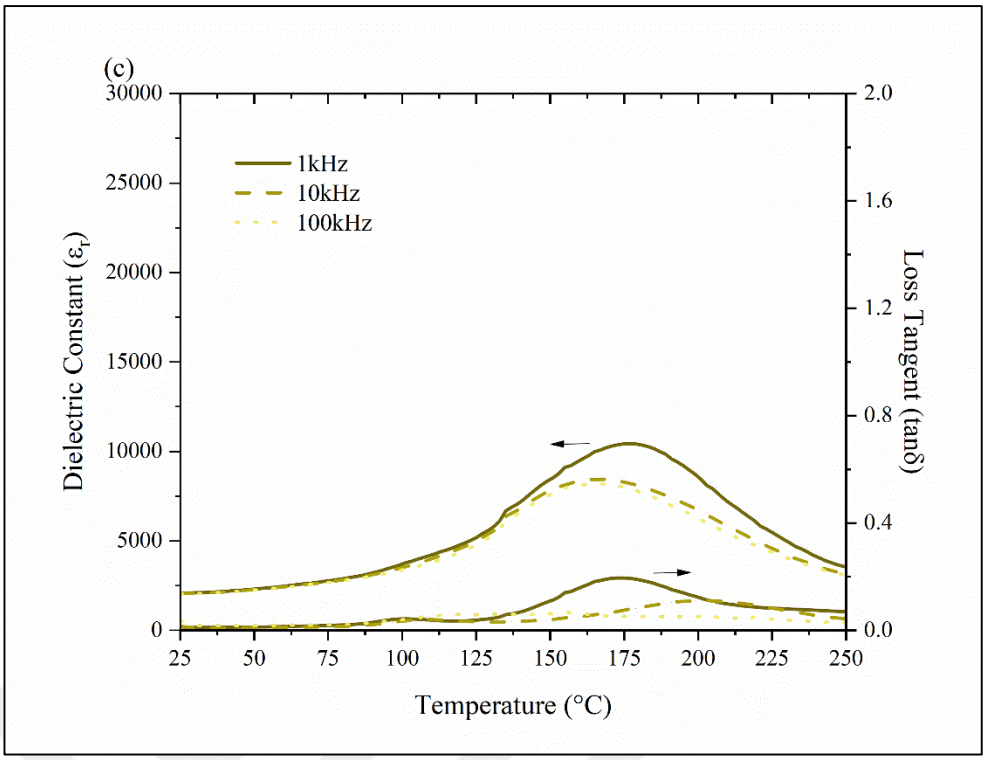

Figure 4.17: Temperature correlation of the dielectric constant and loss tangent of (a) 0.5% Mn, (b) 1.0% Mn, (c) 1.5% Mn-doped ceramics.

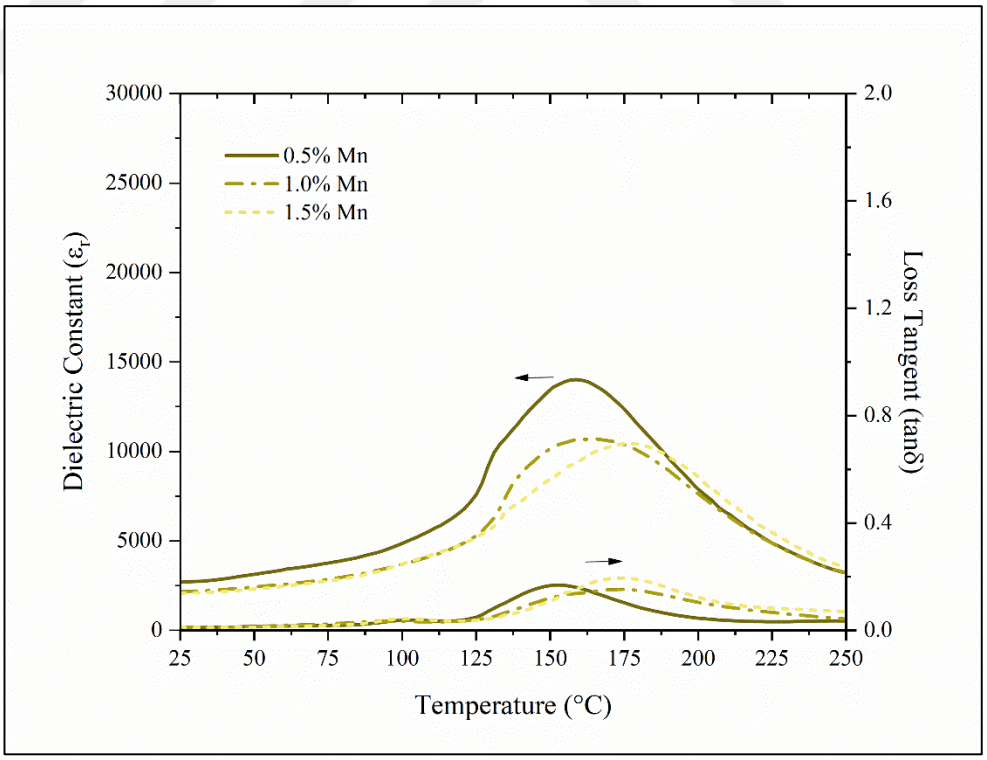

Figure 4.18: Temperature correlation of the dielectric constant and loss tangent of Mn-doped ceramics at 1 kHz.

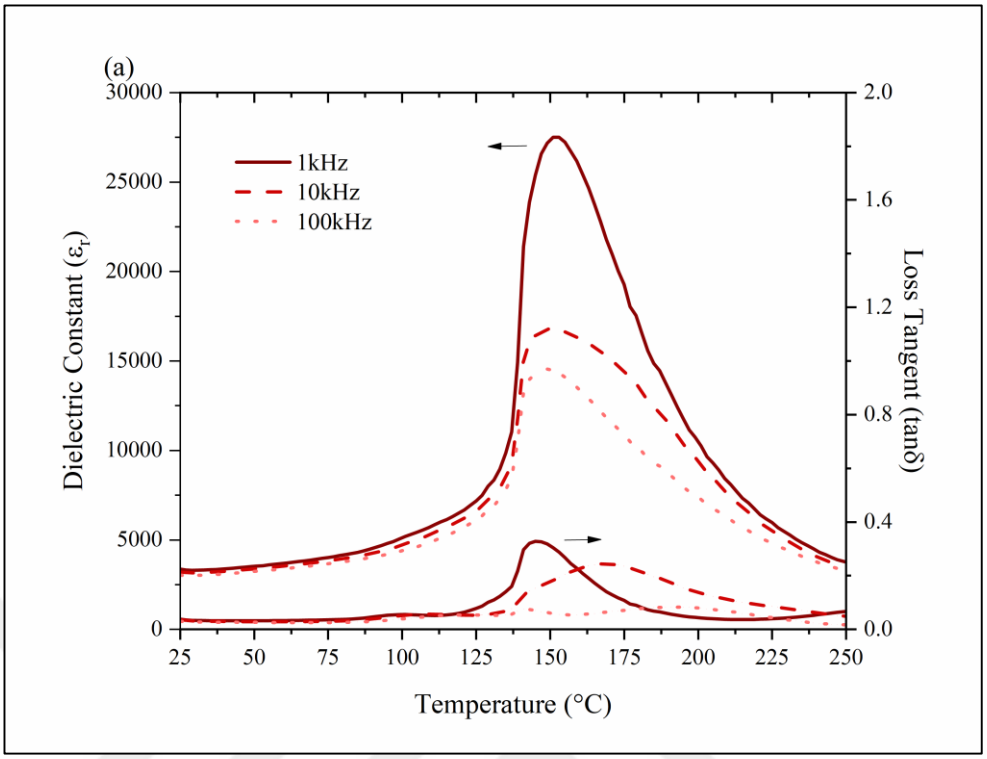
(a)
1kHz
10kHz
100kHz
Dielectric Constant (ε_r)
Loss Tangent (tanδ)
Temperature (°C)
30000
25000
20000
15000
10000
5000
0
2.0
1.6
1.2
0.8
0.4
0.0
25
50
75
100
125
150
175
200
225
250

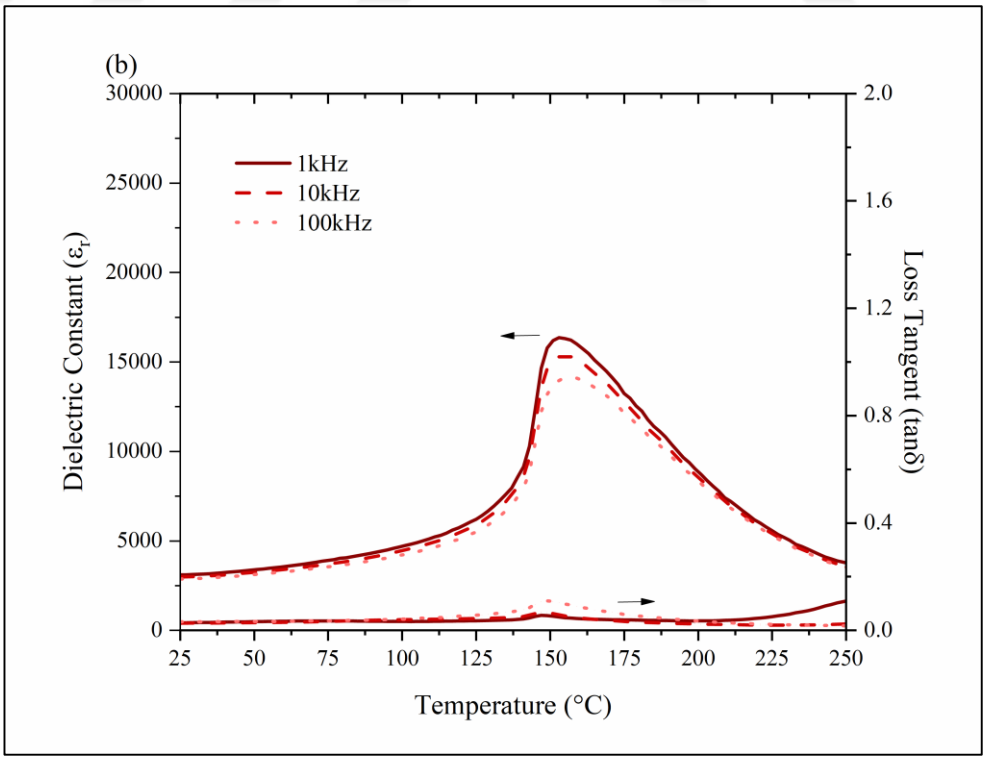
(b)
1kHz
10kHz
100kHz
Dielectric Constant (ε_r)
Loss Tangent (tanδ)
Temperature (°C)
30000
25000
20000
15000
10000
5000
0
2.0
1.6
1.2
0.8
0.4
0.0
25
50
75
100
125
150
175
200
225
250

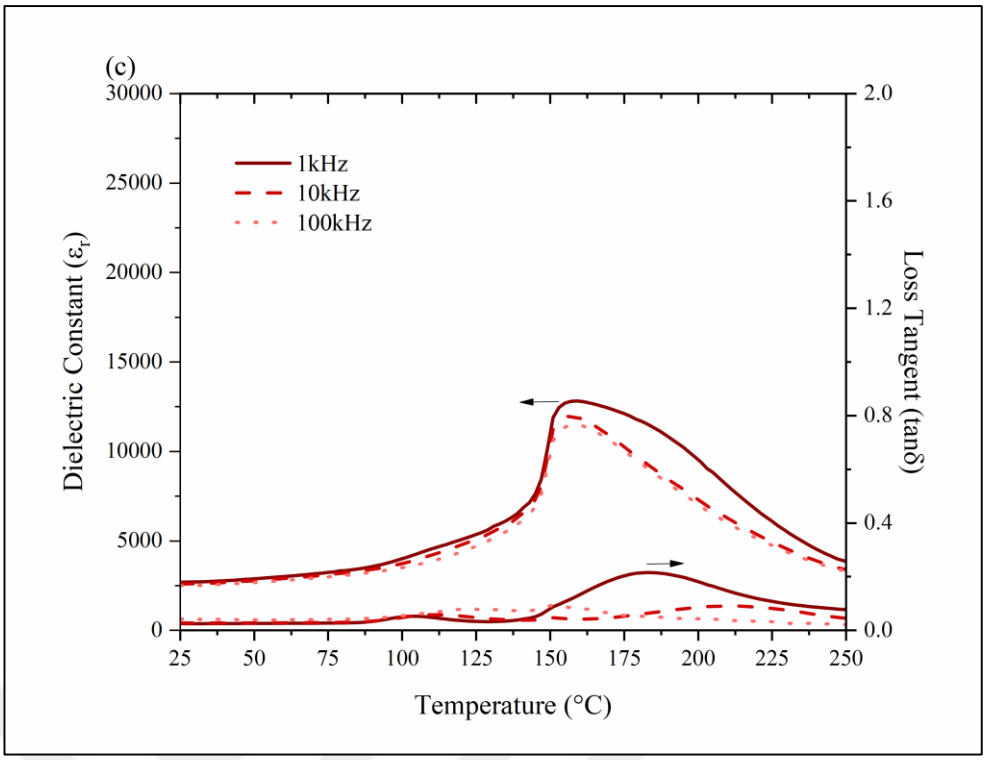

Figure 4.19: Temperature correlation of the dielectric constant and loss tangent of (a) 0.5% Fe, (b) 1.0% Fe, (c) 1.5% Fe-doped ceramics.

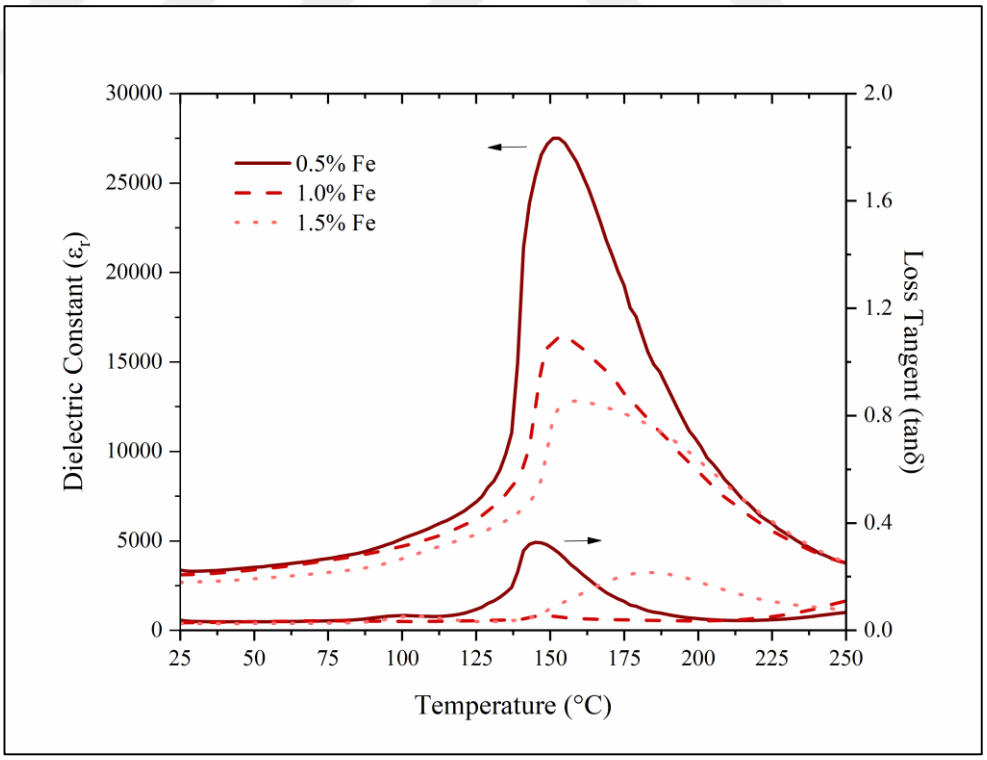

Figure 4.20: Temperature correlation of the dielectric constant and loss tangent of Fe-doped ceramics at 1 kHz.

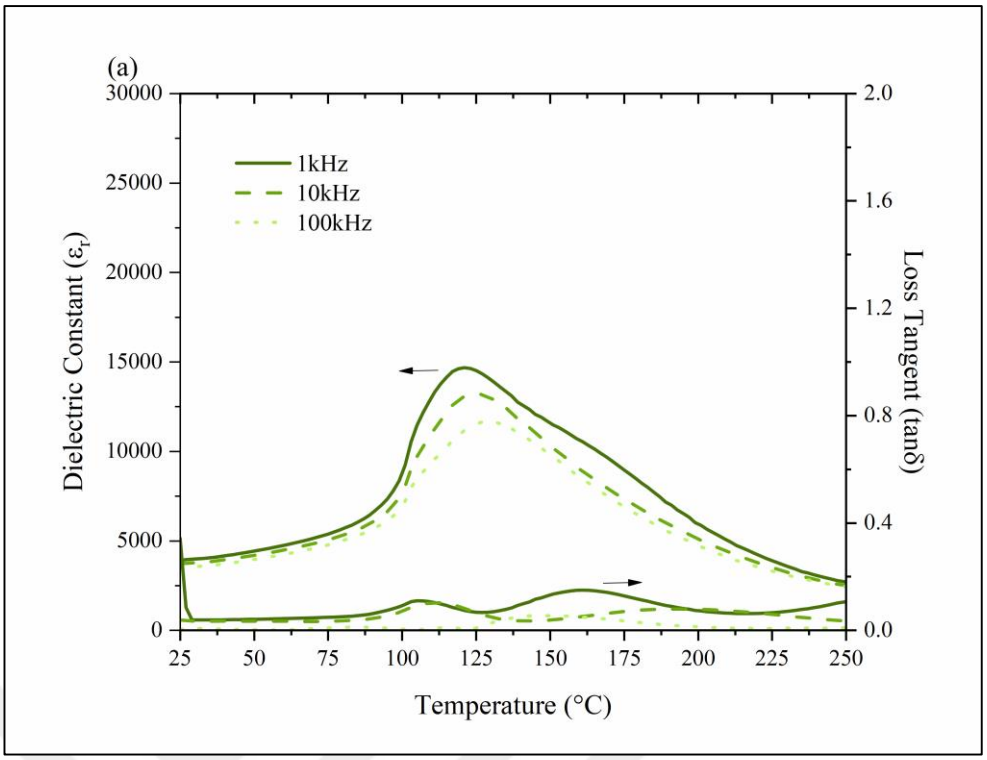
(a)
1kHz
10kHz
100kHz
Dielectric Constant (ε_r)
Loss Tangent (tanδ)
Temperature (°C)
30000
25000
20000
15000
10000
5000
0
2.0
1.6
1.2
0.8
0.4
0.0
25
50
75
100
125
150
175
200
225
250

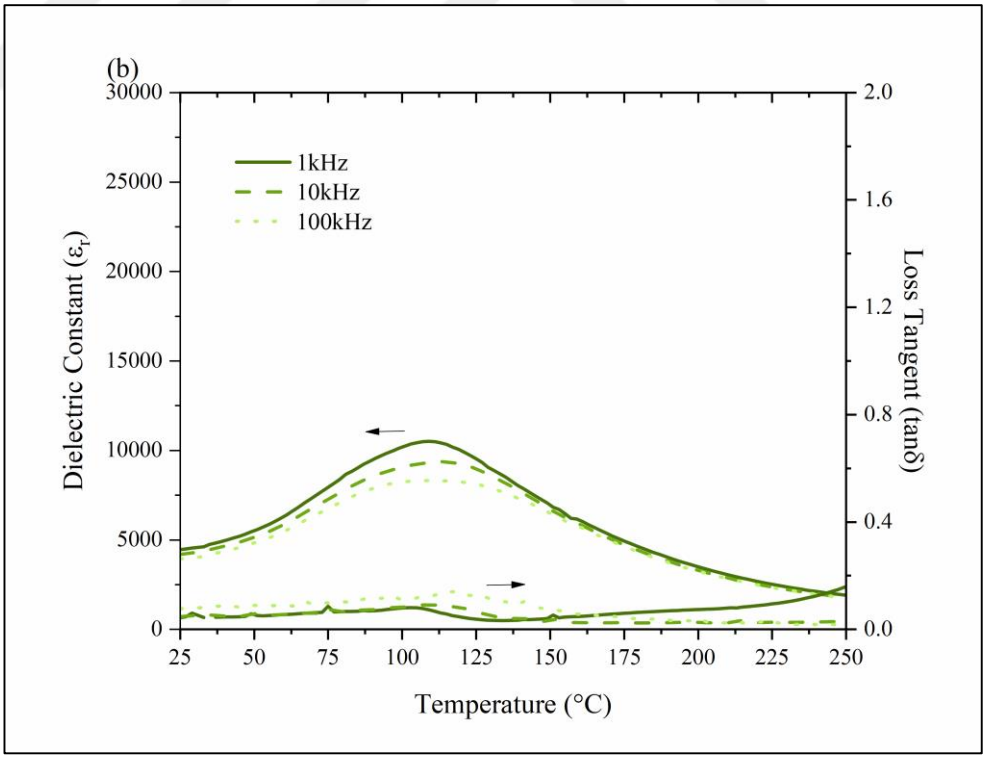
(b)
1kHz
10kHz
100kHz
Dielectric Constant (ε_r)
Loss Tangent (tanδ)
Temperature (°C)
30000
25000
20000
15000
10000
5000
0
2.0
1.6
1.2
0.8
0.4
0.0
25
50
75
100
125
150
175
200
225
250

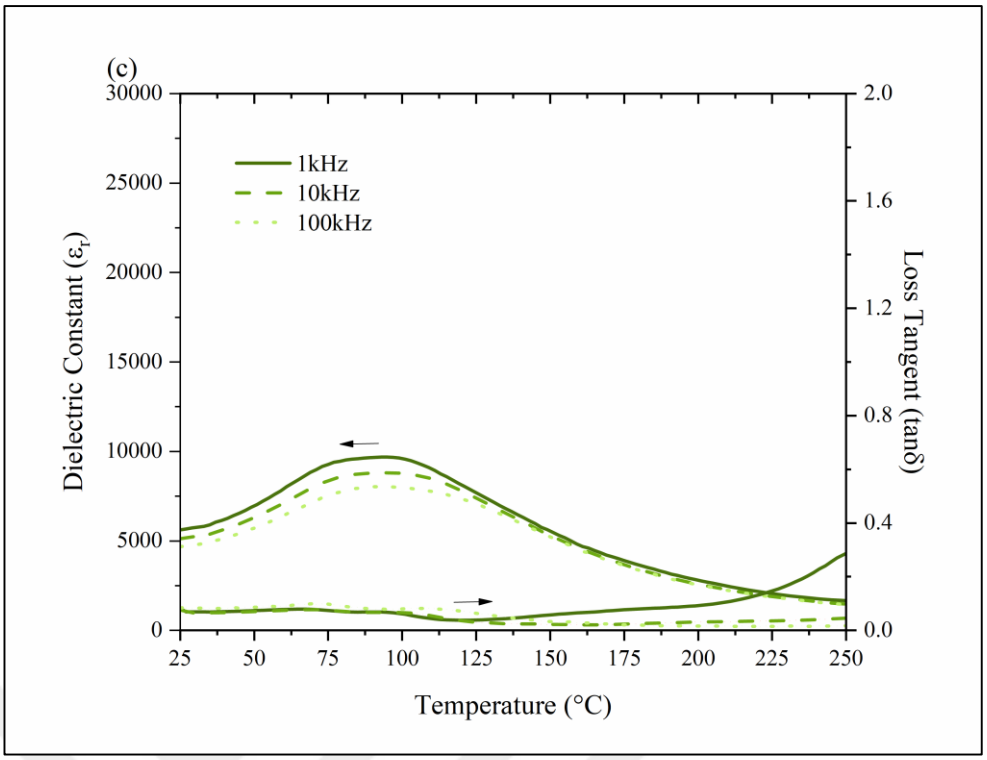

Figure 4.21: Temperature correlation of the dielectric constant and loss tangent of (a) 0.5% Nd, (b) 1.0% Nd, (c) 1.5% Nd-doped ceramics.

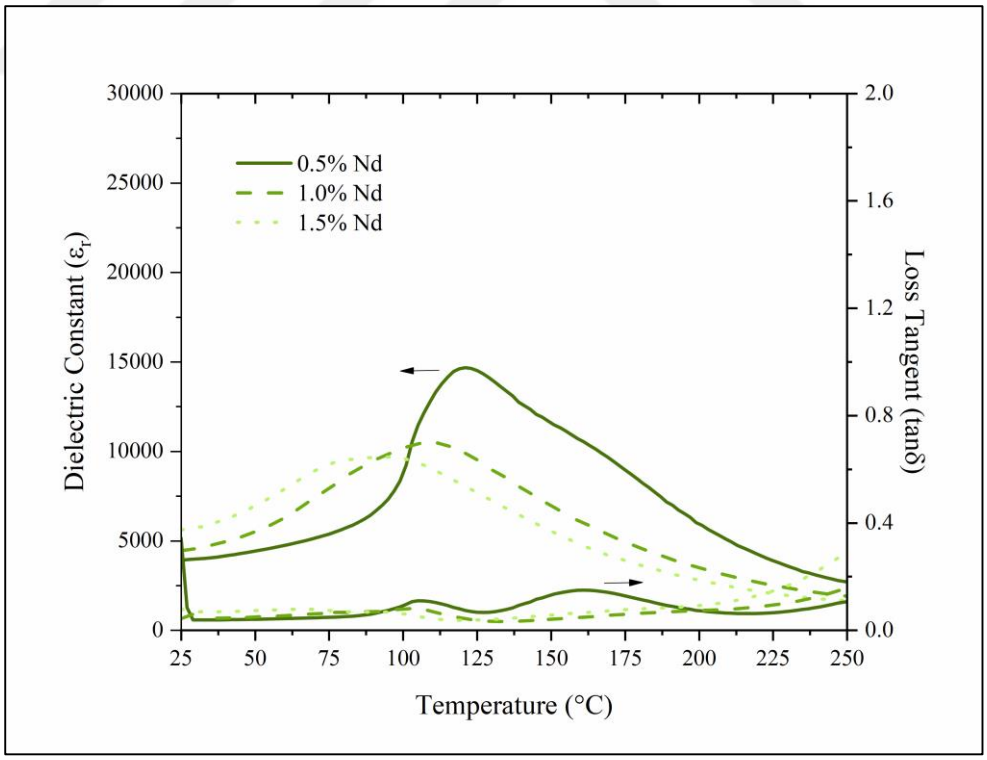

Figure 4.22: Temperature correlation of the dielectric constant and loss tangent of Nd-doped ceramics at 1 kHz.

Table 4.1: Dielectric properties of undoped and doped PNN-PZT ceramics.

Composition	1 kHz			10 kHz			100 kHz		
	ε_r@RT	T_c (°C)	tanδ @RT	ε_r@RT	T_c (°C)	tanδ @RT	ε_r@RT	T_c (°C)	tanδ @RT
Undoped	3067	143	0.075	2880	145	0.136	2733	147	0.063
0.5% Mn	2693	159	0.01	2655	151	0.011	2607	149	0.019
1.0% Mn	2165	163	0.009	2138	157	0.008	2116	159	0.011
1.5% Mn	2084	175	0.014	2057	165	0.014	2038	165	0.037
0.5% Fe	3367	149	0.037	3194	149	0.035	3031	147	0.029
1.0% Fe	3100	151	0.028	2983	153	0.026	2873	155	0.031
1.5% Fe	2689	157	0.025	2591	155	0.027	2497	157	0.041
0.5% Nd	3096	121	0.343	3724	123	0.038	3514	127	0.003
1.0% Nd	4457	111	0.043	4188	113	0.047	3934	109	0.076
1.5% Nd	5618	93	0.082	5121	93	0.075	4669	91	0.084

4.2.2. Polarization-Electric Field Hysteresis Measurements

Polarization measurements under induced electric field of doped and undoped PNN-PZT ceramics were discussed in this part. All measurements were done up to 30 kV/cm electric field. Polarization vs. electric field hysteresis loops of the undoped PNN-PZT ceramic were given in Figure 4.23.

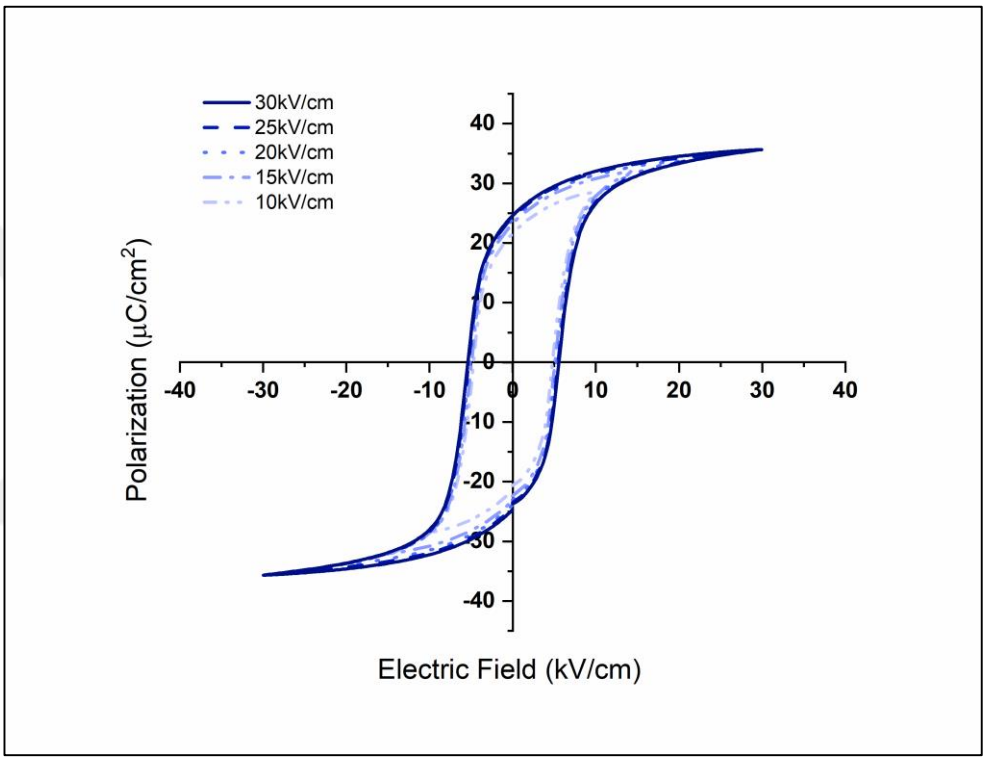

Figure 4.23: P–E hysteresis loops of undoped ceramic.

The polarization-electric field hysteresis loops of the undoped and Mn doped PNN-PZT ceramic were given in the Figure 4.24. The highest P_r value at 30 kV/cm electric field was measured for the undoped ceramic. As the amount of Mn increases, firstly the P_r value decreases and then it increases. It was observed that the E_c value increased as the amount of Mn increased. Thus, with increasing Mn amount, it is expected that the observation of harder character as electrically.

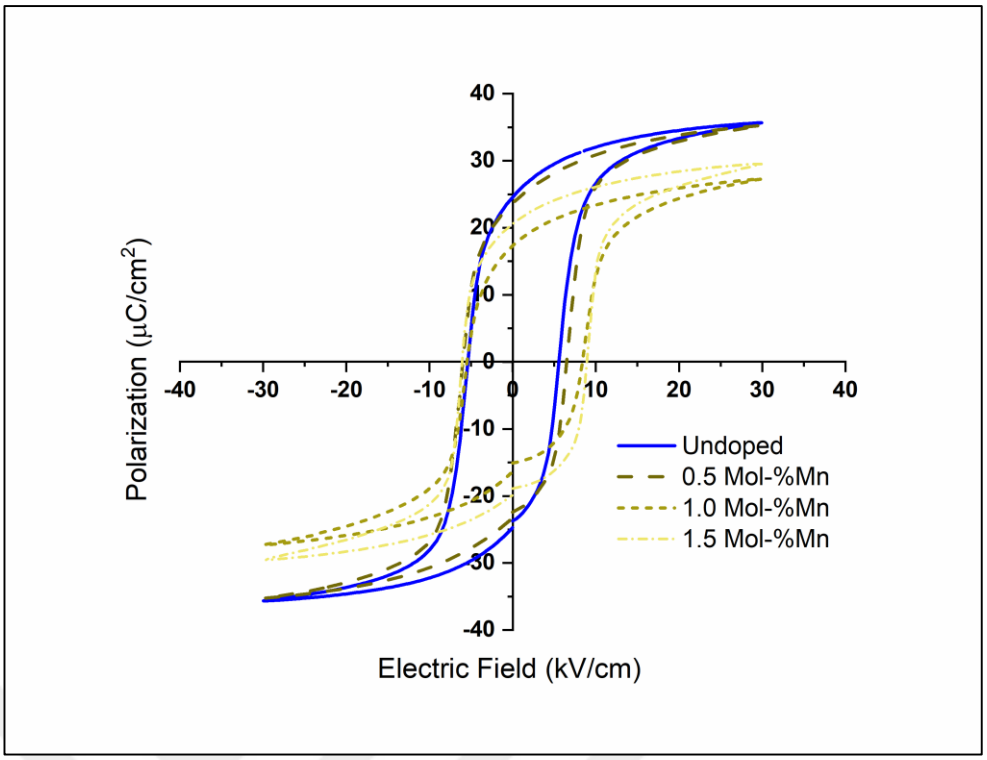

Figure 4.24: Comparison of P–E hysteresis loops of undoped and Mn-doped ceramics.

The comparising P-E hysteresis loops of the undoped and Fe doped PNN-PZT ceramics were given in the Figure 4.25. The highest P_r value at 30 kV/cm electric field was measured for the 0.5% mol Fe doped ceramic as 25.18μC/cm^2. As the amount of Fe was increased in the structure, firstly the P_r value decreases and then it increases. It was observed that the E_c value increased as the amount of Fe increased.

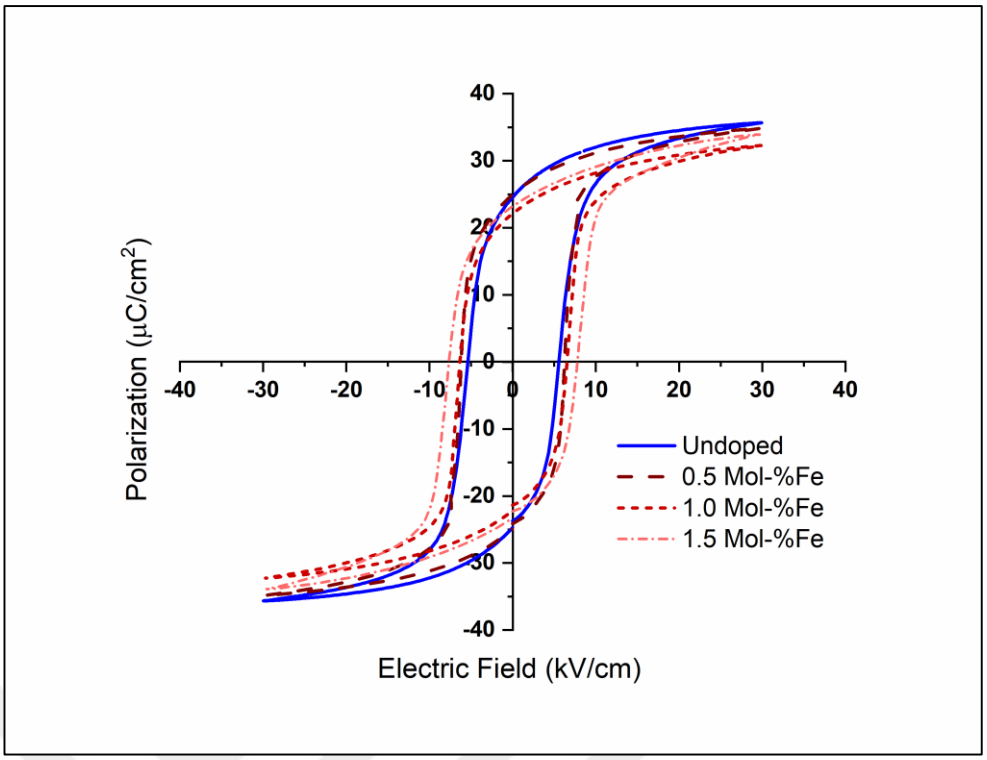

Figure 4.25: Comparison of P–E hysteresis loops of undoped and Fe-doped ceramics.

The comparison of the electric field induced polarization loops of the undoped and Nd doped PNN-PZT ceramics were given in the Figure 4.26. It was observed that as the Nd ratio increases in the structure, the P_r value decreases. The E_c value also decreased as a function of increasing of Nd amount. All ferroelectric values of the ceramics are reported in Table 4.2.

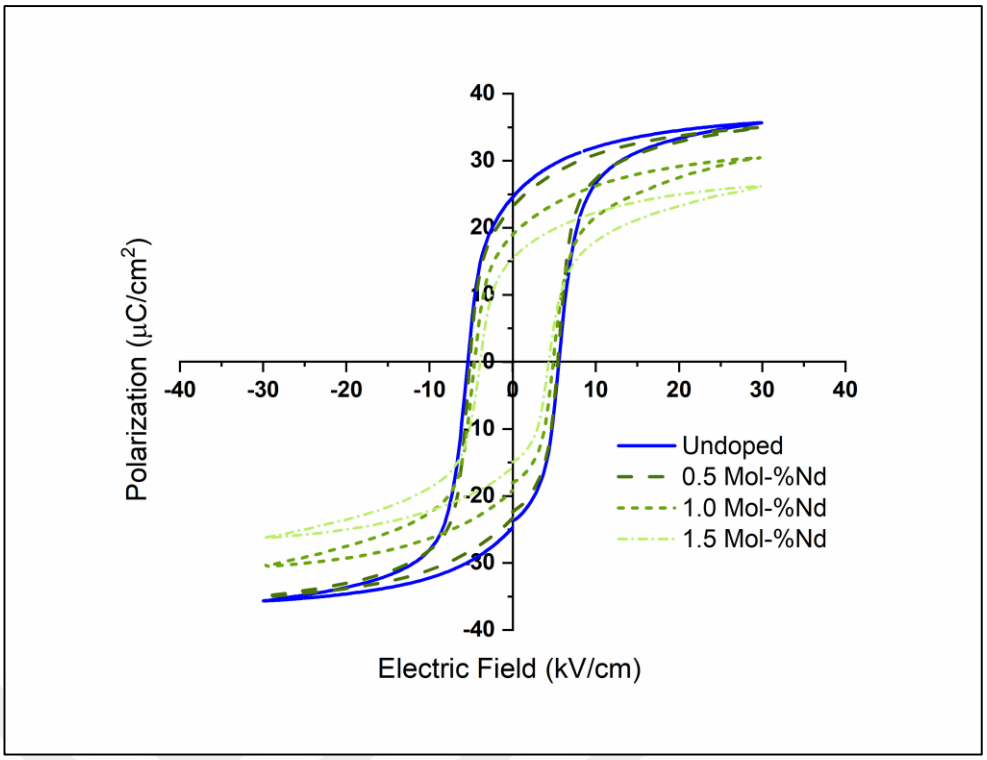

Figure 4.26: Comparison of P–E hysteresis loops of undoped and Nd-doped ceramics.

Table 4.2: P_{max}, P_r and E_c values of doped PNN-PZT ceramics.

Composition	**P_{max} (μC/cm²)**	**P_r(μC/cm²)**	**E_c (kV/cm)**
Undoped	35.66	24.85	5.46
0.5 Mol-%Mn	35.24	23.65	6.29
1.0 Mol-%Mn	27.29	16.73	6.98
1.5 Mol-%Mn	29.49	20.57	7.45
0.5 Mol-%Fe	34.85	25.18	6.18
1.0 Mol-%Fe	32.26	22.32	6.35
1.5 Mol-%Fe	33.95	23.39	7.73
0.5 Mol-%Nd	34.98	23.42	5.19
1.0 Mol-%Nd	30.48	19.18	4.74
1.5 Mol-%Nd	26.18	15.7	4.16

Comparison of P–E hysteresis loops and strain curves of PNN-PZT ceramic and PNN-PZT piezocomposite at 20 kV/cm is given in Figure 4.27.

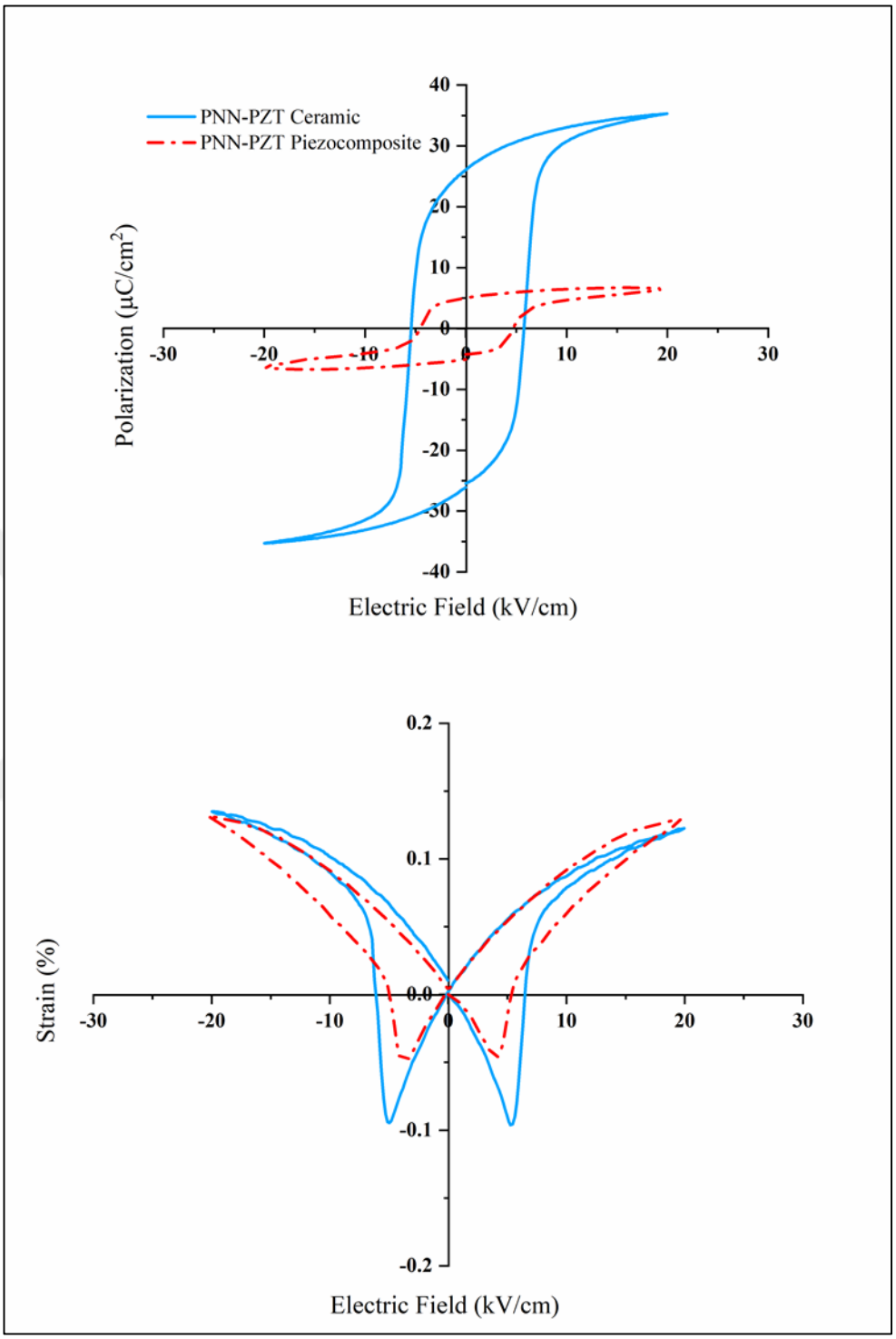

Figure 4.27: Comparison of P–E hysteresis loops and strain curves of PNN-PZT ceramic and PNN-PZT piezocomposite.

Ferroelectric properties of PNN-PZT composite and PNN-PZT ceramic are given in Table 4.3. Lower P_{max}, P_r, and E_c values were measured for piezocomposite

than ceramic due to the lower content of active ceramic phase in composite. The strain levels are comparable to bulk ceramic, since the fiber volume % is not effective in the case of longitudinal displacement of fibers in a 1-3 piezocomposite.

Table 4.3: P_{max}, P_r, E_c and maximum strain values of doped PNN-PZT composite and ceramic.

Composition	**P_{max} ($\mu C/cm^2$)**	**P_r ($\mu C/cm^2$)**	**E_c (kV/cm)**	**Maximum Strain (%)**
PNN-PZT Composite	6.51	5.04	4.59	0.13
PNN-PZT Ceramic	35.29	26.08	5.79	0.12

4.2.3. Effects of Doping on PNN-PZT Ceramic

In this study, 0.5%, 1.0% and 1.5% Mn, Fe and Nd were doped to PNN-PZT ceramic. It is expected that Mn and Fe can occupy B-site and Nd can occupy A-site due to the their ionic radii in the ABO_3 perovskite structure. Mn and Fe doping can act as acceptor dopants for B-site ions. These dopants may cause formation of oxygen vacancies in the perovskite structure. Nd doping can act as donor dopant for A-site ion. This dopant may cause formation of lead vacancies in the perovskite structure. Possible defect chemistry reactions for different dopants are given in Figure 4.28. Mn^{4+} and Fe^{3+} can be substituted with Nb, Zr or Ti as acceptor dopant and Nd^{3+} can be substituted with Pb as donor dopant.

Mn doping

$$2MnO_2 \longrightarrow 2Mn_{Nb}^{'} + V_O^{\bullet\bullet} + 4O_o$$

$$MnO_2 \longrightarrow Mn_{Zr} + 2O_o$$

$$MnO_2 \longrightarrow Mn_{Ti} + 2O_o$$

Fe doping

$$Fe_2O_3 \longrightarrow 2Fe_{Ti}^{'} + V_O^{\bullet\bullet} + 3O_o$$

$$Fe_2O_3 \longrightarrow 2Fe_{Zr}^{'} + V_O^{\bullet\bullet} + 3O_o$$

$$Fe_2O_3 \longrightarrow 2Fe_{Nb}^{''} + 2V_O^{\bullet\bullet} + 3O_o$$

Nd doping

$$Nd_2O_3 \longrightarrow 2Nd_{Pb}^{\bullet} + V_{Pb}^{''} + 3O_o$$

Figure 4.28: Possible defect chemistry reactions for dopants.

For Mn and Fe doping on the B-site, oxygen vacancies can form defect dipoles which can accumulate at domain walls. Defect dipoles can prevent domain wall movement which gives a hard character to the ceramic. The oxygen vacancies in the perovskite structure can promote lattice diffusion, thus assisting the sintering and grain growth. For Mn and Fe doping, the dielectric constant decreased with the increase in MnO_2 and Fe_2O_3 contents due to the hardener ions affected the movement of domains while Curie temperature so increased. Compared with the undoped ceramic, Mn and Fe-doped ceramics showed larger coercive field (Ec) values due to the harder domain switching. The substitution of Pb^{2+} with Nd^{3+} on the A-site can cause the formation of some lead vacancies. This situation would relax the strain caused by reorientatiton of domains. Therefore, the movement of the domains becomes easier and leads to a softening in the piezoelectric properties [Berksoy- Yavuz et al., 2020], [Du et al., 2012], [Kang and Kang, 2019].

4.2.4. Electromechanical Properties of PNN-PZT Ceramics

The empedance (Z)-frequency (f) graphs of doped and undoped PNN-PZT ceramic are given in the Figure 4.29, Figure 4.30, Figure 4.31 and the electromechanical properties are given in the Table 4.4. It was measured that the undoped PNN-PZT ceramic has 30 kHz bandwidth. It was determined that the undoped PNN-PZT ceramic had a wider band gap than the doped ceramic. It was determined that the bandwidth increased as the amount of Mn doping increased, while the bandwidth decreased as the amount of Nd and Fe doping increased. The highest mechanical quality factor belongs to Mn doped ceramics. It was determined that as the amount of doping increased, the mechanical quality factor also increased for all doped ceramics. The highest piezoelectric charge constant (d_{33}) belongs undoped ceramics.

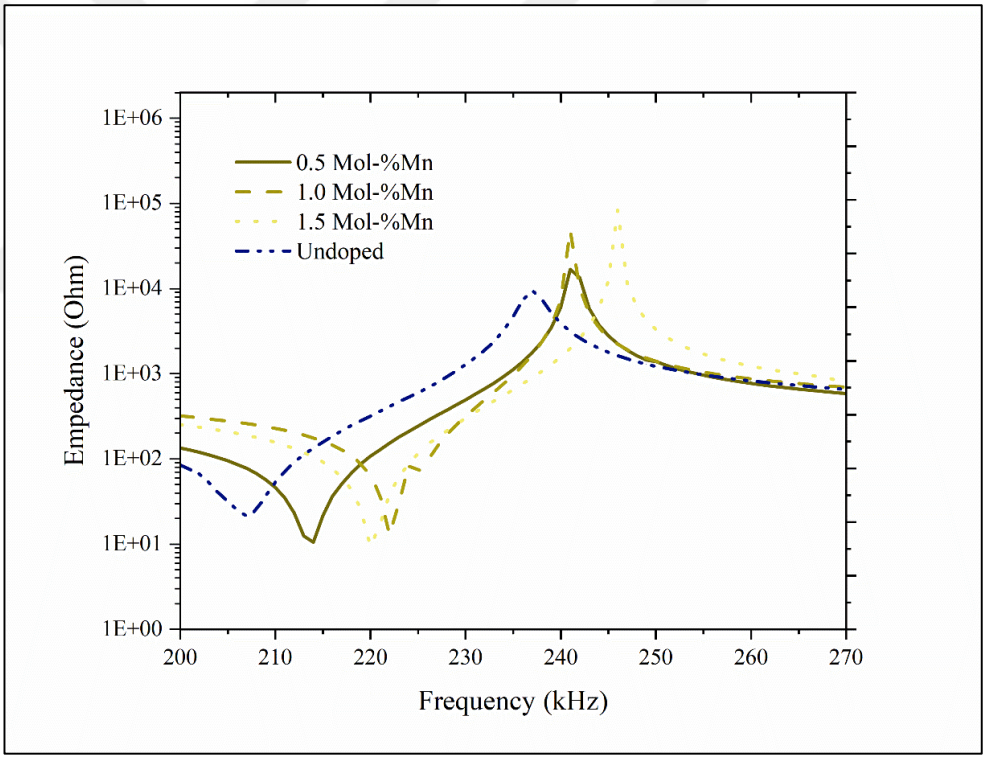

Figure 4.29: Empedance vs. frequency measurements of undoped and Mn-doped ceramics.

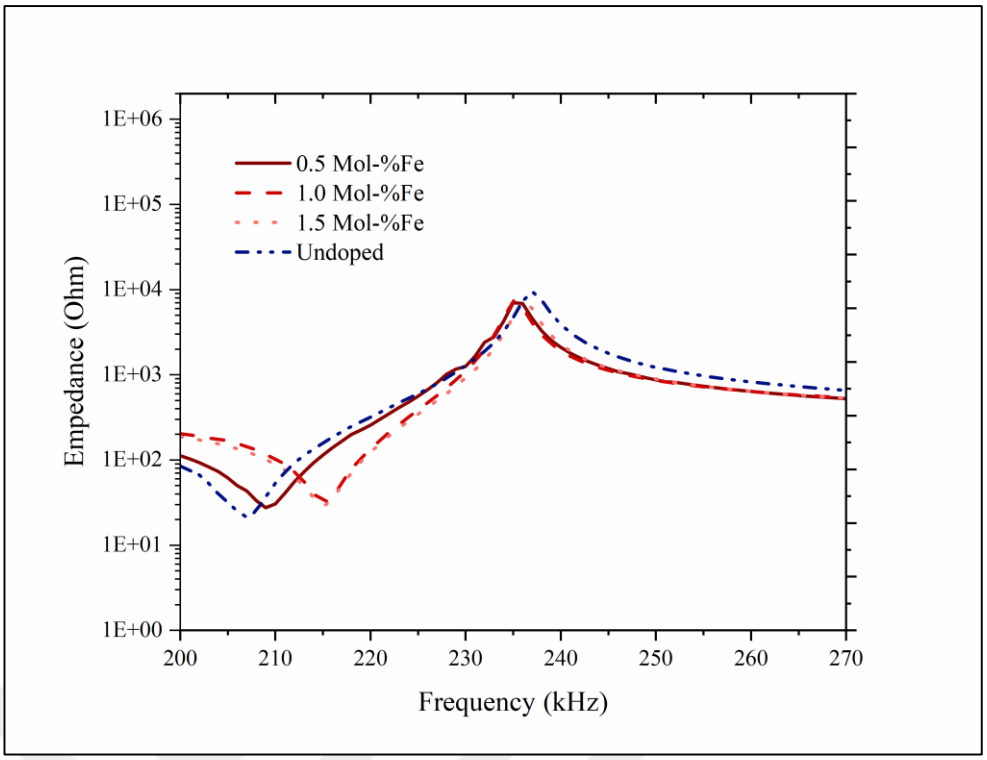

Figure 4.30: Empedance vs. frequency measurements of undoped and Fe-doped ceramics.

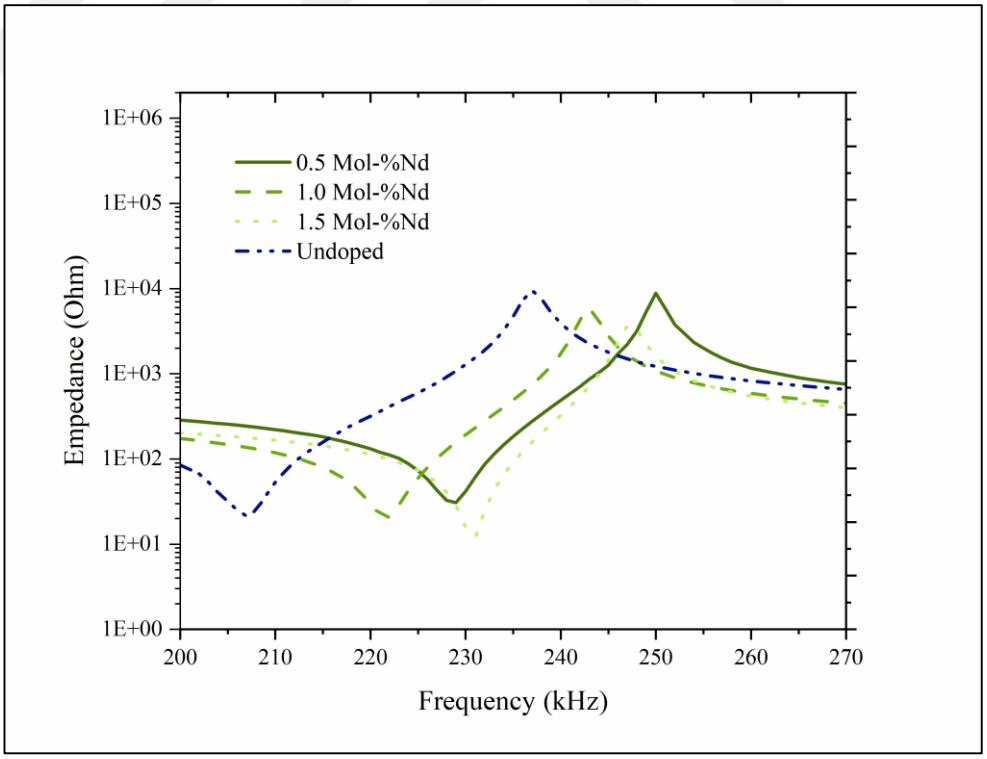

Figure 4.31: Empedance vs. frequency measurements of undoped and Nd- doped ceramics.

Table 4.4: Electromechanical properties of undoped and doped ceramics.

Composition	**Resonance Frequency-f_r (kHz)**	**Antiresonance Frequency-f_a (kHz)**	**Phase Angle (°)**	**Mechanical Quality Factor-Q_m**	**Electromechanical Coefficient-k_p (%)**	**Piezoelectric Charge Constant-d_{33} (pC/N)**
Undoped	207	237	81	67	0.59	705
0.5mol-%Mn	214	242	86	132	0.56	530
1.0mol-%Mn	222	241	87	227	0.46	280
1.5mol-%Mn	220	246	88	228	0.53	320
0.5mol-%Nd	228	250	78	65	0.48	500
1.0mol-%Nd	222	243	79	73	0.48	450
1.5mol-%Nd	230	247	77	105	0.42	230
0.5mol-%Fe	210	236	79	44	0.54	590
1.0mol-%Fe	215	235	77	70	0.47	460
1.5mol-%Fe	215	236	78	70	0.49	430

4.2.5. Underwater Measurement Results of PNN-PZT Ceramics and Composite

Piezocomposites with 1-3 connectivity work in thickness mode. 1-3 piezocomposites work very efficiently as a sensors at frequencies in the Hz-MHz range [Kaya, 2018]. Performances of PNN-PZT ceramic, 1-3 piezocomposite and PZT-5A, PZT-5H ceramics were compared for underwater accoustic applications. Undoped PNN-PZT ceramic and piezocomposites were poled for 10 minutes at room temperature by applying 25kV/cm electric field while PZT-5A and PZT-5H ceramic were poled for 10 minutes at 120 ℃ by applying 20kV/cm for underwater measurement. Underwater admittance and phase angle vs. frequency graphs of undoped, PZT-5A, PZT-5H ceramic, piezocomposites are given in the Figure 4.32. Resonance and antiresonance frequency of ceramics are given in Table 4.5. It was observed that the highest band with belongs to PNN-PZT composite. The frequency range of the composite is lower and wider than other ceramics.

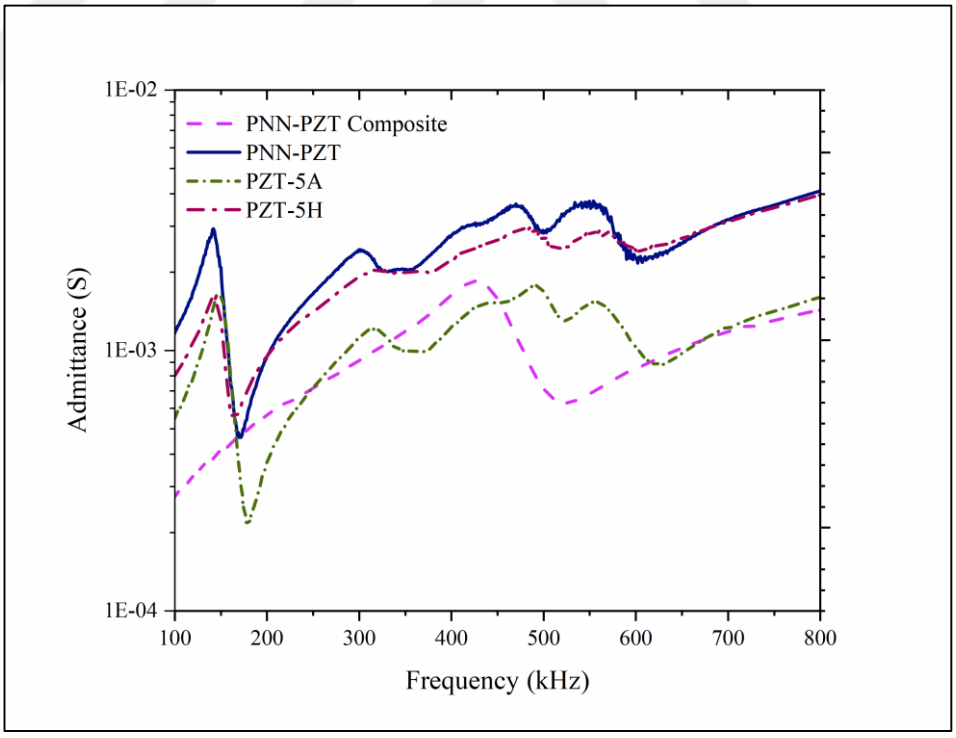

Figure 4.32: Admittance-phase angle vs. frequency measurements of undoped, PZT-5A, PZT-5H and piezocomposite.

Table 4.5: Resonance and antiresonance frequencies of ceramics.

Composition	**Resonanace Frequency-f_r (kHz)**	**Antiresonance Frequnecy-f_a (kHz)**	**Piezoelectric Charge Costant (pC/N)**
PNN-PZT Composite	430	522	401
PNN-PZT	553	603	710
PZT-5A	557	630	440
PZT-5H	557	603	400

The performance of an underwater projector is measured by its TVR value. It corresponds to the free field pressure created at a distance of 1 m versus a potential difference of 1 V applied across the electrical terminals of the transducer. The unit of TVR is dB ref μPa/V @1m. TVR vs. frequency graphs of undoped, PZT-5A, PZT-5H ceramic, piezocomposites are given in the Figure 4.33.

When the thickness mode resonance TVR peak values of PNN-PZT composite, PNN-PZT, PZT-5A and PZT-5H ceramics were compared, it was seen that the highest TVR value belongs to PNN-PZT ceramic. The PNN-PZT composite was demonstrated to have a comparable performance with that of PNN-PZT ceramic. TVR values of PNN-PZT ceramic and PNN-PZT composite were calculated as 144.71 dB at 564 kHz and 142.60 dB at 444 kHz, respectively. TVR values of PZT-5A ceramic was calculated as 141.45 dB at 567 kHz and PZT-5H ceramic was calculated as 142.12 dB at 570 kHz.

The band width of the PNN-PZT composite is 84 kHz, PNN-PZT is 81 kHz, PZT-5A is 71 kHz and PZT-5H is 70 kHz. Despite soft piezoelectric ceramics, such as PZT-5A and PZT-5H, have greater TVR peak values due to higher dielectric constants and piezoelectric coefficients, they have heating problem during continuous operation of active underwater transducers due to their higher loss tangent. As a result, they are often used for passive hydrophone applications rather than active transducer applications [Yalcin, 2022].

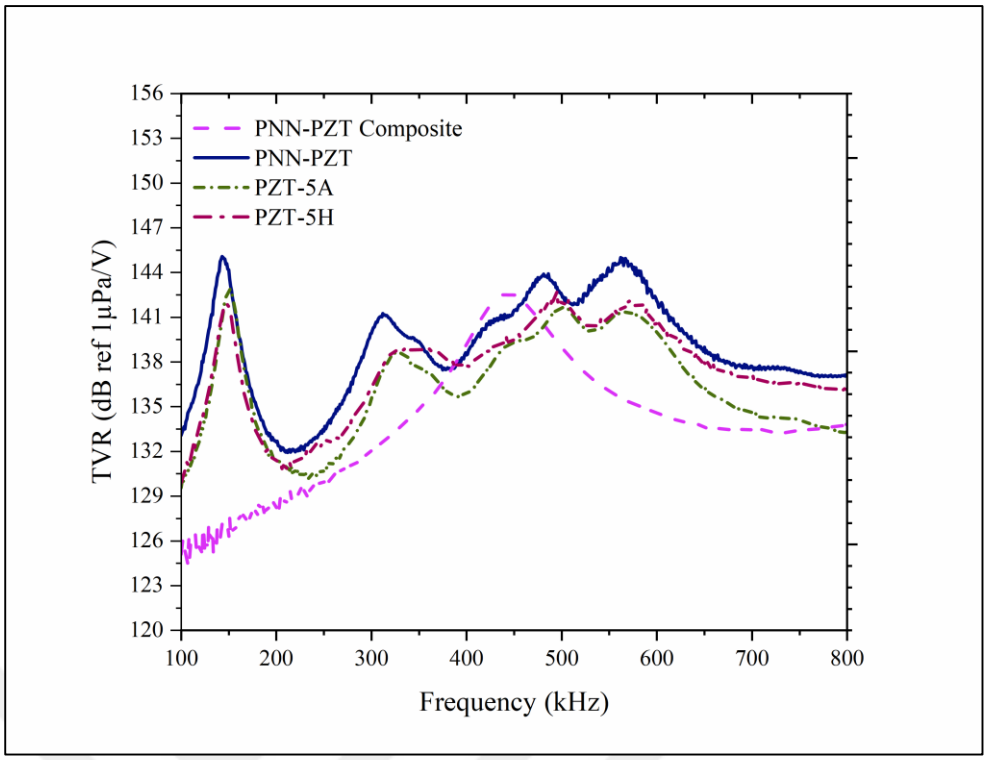

Figure 4.33: TVR vs. frequency measurements of undoped, PZT-5A, PZT-5H and piezocomposite.

In electro-acoustic transducers, FFVS is the open circuit electrical voltage corresponding to the unit sound pressure (1 µPa). The unit of FFVS is dB ref V/µPa @1m [Kaya, 2018]. FFVS vs. frequency graphs of undoped, PZT-5A, PZT-5H ceramic, piezocomposites are given in the Figure 4.34.

When the thickness mode resonance FFVS peak values of PNN-PZT composite, PNN-PZT, PZT-5A and PZT-5H ceramics were compared, it was seen that the highest FFVS value belongs to PNN-PZT composite. FFVS values of PNN-PZT ceramic and PNN-PZT composite were calculated as -214.08 dB at 588 kHz and -206.13 dB at 506 kHz, respectively. FFVS values of PZT-5A ceramic was calculated as -209.86 dB at 604 kHz and PZT-5H ceramic was calculated as -215.99 dB at 584 kHz.

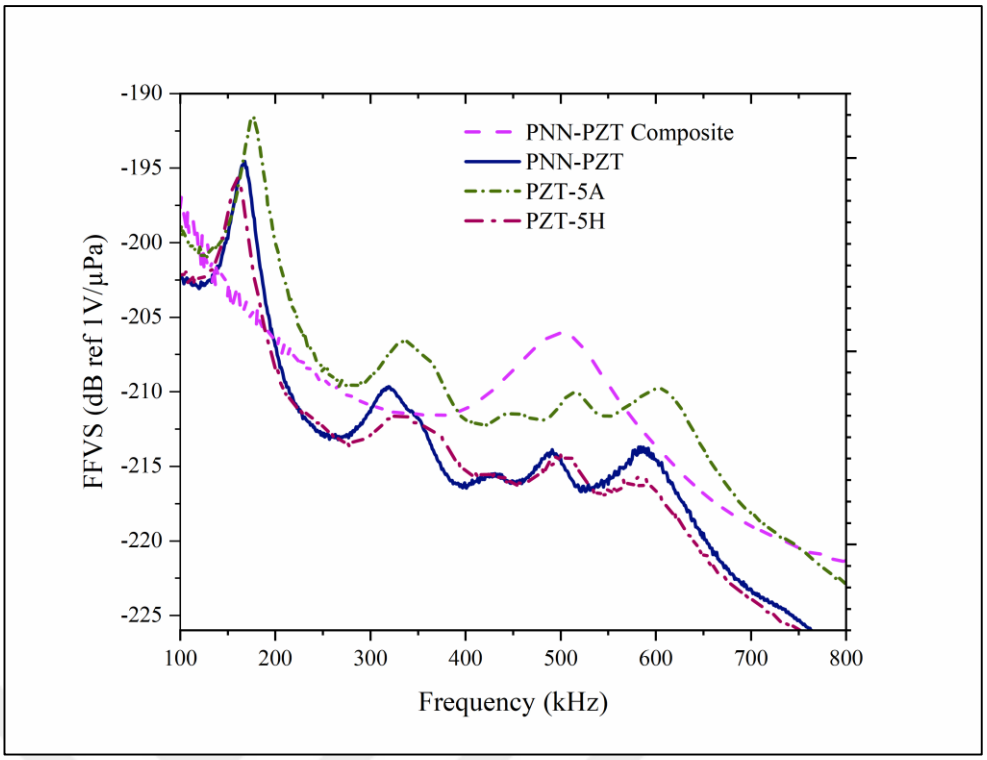

Figure 4.34: FFVS vs. frequency measurements of undoped, PZT-5A, PZT-5H and piezocomposite.

5. CONCLUSION

Undoped and doped ceramics were fabricated using columbite method. Pure perovskite structure was obtained in undoped and Fe, Mn, 0.5% Nd-doped PNN-PZT compositions. Secondary phases were seen in 1.0 and 1.5 %Nd-doped ceramics. Sintering time and temperature can be studied to overcome this problem. As a result of microstructure analysis, it was observed that a dense structure was obtained in all ceramics.

Mn and Fe-doped ceramics exhibited hard character because of the oxygen vacancies while Nd-doped ceramic showed soft character because of the Lead vacancies. The maximum dielectric constant value at 100 kHz was measured as 4669 for 1.5% Nd doped ceramic. So, Nd-doped ceramics can be suitable for capacitor applications. Compared to undoped and Mn, Fe-doped ceramics, 1.5% Nd-doped ceramic can be studied for solid state cooling applications due to the lowest Curie temperature as 91°C which is closer to room temperature. Mn and Fe-doped ceramics can be used for ultrasonic transducer and motor applications due to their hard character.

The highest d_{33} value was measured as 705 pC/N for undoped ceramic, and this composition was chosen for fabricating 1-3 piezocomposite due to the higher piezoelectric properties. Sodium alginate gelation method was used to fabricate fibers. PNN-PZT 1-3 piezocomposite was fabricated and its underwater maesurements were compared with the PZT-5A, PZT-5H, and PNN-PZT ceramics. Due to the higher piezoelectric properties, FFVS-TVR values, flexibility, and larger bandwidth of 1-3 PNN-PZT piezocomposite, it can be promising for underwater acoustic applications.

REFERENCES

Akdogan E. K., Allahverdi M., Safari A., (2005), "Piezoelectric composites for sensor and actuator applications", IEEE Transactions on Ultrasonics, Ferroelectrics, and Frequency Control, 52 (5), 746-775.

Alkoy S., Yanik H., Yapar B., (2007), "Fabrication of lead zirconate titanate ceramic fibers by gelation of sodium alginate" , Ceramics international, 33(3), 389-394.

Andres J., Longo V., Cavalcante L., Moreira M.L., Varela., Longo E., "A fresh look at the structural ferroelectric and photoluminescent properties in perovskites", Nova Science Publishers Inc., 2011.

Bain A.K., (2017), " Ferroelectrics", Wiley-VCH Verlag GmbH & Co. KGaA.

Berksoy-Yavuz A., Mensur-Alkoy E., Erdem E., Alkoy S., (2020), "Electrical properties, EPR analyses and defect chemistry of Mn-doped 0.675 PMN-0.325PT piezoceramics", Ceramics International, 46(18), 28980-28986.

Bharadwaj, S. R., Varma, S., Wani, B. N., (2012), "Electroceramics for fuel cells, batteries and sensors", Functional Materials, 639-674.

Bibi F., Villain, M., Guillaume C., Sorli B., Gontard N., (2016), "A review: Origins of the dielectric properties of proteins and potential development as bio-sensors", Sensors, 16(8), 1232.

Bove T., Wolny W., Ringgaard E., Pedersen A., (2001), "New piezoceramics PZT–PNN material for medical diagnostics applications", Journal of the European Ceramic Society, 21 (10), 1469-1472.

Butnoi P., Pisitpipathsin N., Eitssayeam S., Rujijangul G., Tunkasiri T., Pengpat K., (2014), "Improvement of mechanical and electrical properties of PNN-PZT Ceramics with Strontıum Content", SURANAREE JOURNAL OF SCIENCE AND TECHNOLOGY, 21(1), 27-34.

Callister W.D., (2007), "An introduction: material science and engineering", 7th. Edition, John Wiley & Sons, Inc.

Chen, Y., Zheng D. Y.,Wang Y. Y., (2020), "Doping for inducing the formation of lead niobate-nicklate in piezo-ceramics", Journal of Alloys and Compounds, 845, 155903.

Cheng C., Zheng D. Y., Peng G. G., Hu S. M., Zhang H., Zhang J., (2017), "The effects of Sm_2O_3 doping on properties of PNN–PZT ceramics near morphotropic phase boundary", Journal of Materials Science: Materials in Electronics, 28(2), 1624-1630.

Chu S. Y., Hsieh C. S., (1999), "The piezoelectric properties of low-temperature sintered PNN-PZT-based ceramics and their applications", Integrated Ferroelectrics, 24(1-4), 121-127.

Damjanovic D., (1998), "Ferroelectric, dielectric and piezoelectric properties of ferroelectric thin films and ceramics", Progress in Physics, 61(9), 1267.

Davari P., Ghasemi N., Zare, F., (2014), "Power converters design and analysis for high power piezoelectric ultrasonic transducers" , European Conference on Power Electronics and Applications, 1-9, Lappeenranta, Finland, August 2014.

Dong H., Wu J., Zhang H., Zhang G., "Measurement of a piezoelectric transducer's mechanical resonant frequency based on residual vibration signals" , In The 2010 IEEE International Conference on Information and Automation, 1872-1876, Harbin, China, June 2010.

Du J., Qiu J., Zhu K., Ji, H., Chen, Y., "Fabrication and characterization of relaxor-ferroelectric 0.55 Pb ($Ni_{1/3}Nb_{2/3}$) O3-0.45 Pb ($Zr_{0.3}Ti_{0.7}$)O_3 ceramics with sintering aid", In Third International Conference on Smart Materials and Nanotechnology in Engineering, 56-61, Shenzhen, China, November 2011.

Du J., Qiu J., Zhu K., Ji H., Pang X., Luo J., (2012), "Effects of Fe_2O_3 doping on the microstructure and piezoelectric properties of 0.55Pb($Ni_{1/3}Nb_{2/3}$)O_3-0.45Pb($Zr_{0.3}Ti_{0.7}$)O_3 ceramics", Materials Letters, 66(1), 153-155.

Gao X., Wu J., Yu Y., Chu Z., Shi H., Dong S., (2018), "Giant piezoelectric coefficients in relaxor piezoelectric ceramic PNN-PZT for vibration energy harvesting", Advanced Functional Materials, 28(30), 1706895.

Gururaja T. R., Schulze W. A., Cross L E., Newnham R. E., Auld B. A., Wang Y. J., (1985), "Piezoelectric composite materials for ultrasonic transducer applications. Part I: Resonant modes of vibration of PZT rod-polymer composites", IEEE Trans. Sonics Ultrason, 32(4), 481-498.

Haertling G. H., (1999), "Ferroelectric ceramics: history and technology", Journal of the American Ceramic Society, 82 (4), 797-818.

Islam R.H., Priya S., (2012), "Progress in dual (piezoelectric-magnetostrictive) phase magnetoelectric sintered composites", Advances in Condensed Matter Physics, 1-29.

Jordan T. L., Ounaies Z., (2001), "Piezoelectric ceramics characterization", Instıtute for computer applications in science and engıneering, Hampton, Virginia, 2001.

Kang M., Kang L. H., (2019), "Piezoelectric characteristics of 0.55Pb ($Ni_{1/3}Nb_{2/3}$)O_3-0.45Pb(Zr,Ti)O_3 ceramics with different MnO_2 concentrations for ultrasound transducer applications", Materials, 12(24), 4115.

Kao K. C., (2004), "Ferroelectrics, Piezoelectrics, and Pyroelectrics", K.C. Kao, Editor, "Dielectric Phenomena in Solids", Academic Press.

Kaya M. Y., (2018), “Esnek gerilmeli dönüştürücü tasarımı, üretimi, karakterizasyonu ve uygulamaları ”, Doktora Tezi, Gebze Teknik Üniversitesi.

Khan M. I., Upadhyay T. C., (2021), “General Introduction to Ferroelectrics”, Multifunctional Ferroelectric Materials,7

Kim J. M., Kim J. S., Cheon C. I., (2011), “Low-temperature sintering and electrical properties of PGO-doped PNN-PZT ceramics”, Journal of Ceramic Processing Research, 12(1), 12-15.

Liu H., Nie R., Yue Y., Zhang Q., Chen Q., Zhu J., Yu P., Xiao D., Wang C., Wang X., (2015), “Effect of MnO_2 doping on piezoelectric, dielectric and ferroelectric properties of PNN–PZT ceramics”, Ceramics International, 41 (9, Part A), 11359-11364.

Liu S., Shen B., Hao H., Zhai J., (2019), “Glass–ceramic dielectric materials with high energy density and ultra-fast discharge speed for high power energy storage applications”, Journal of Materials Chemistry C, 7(48), 15118-15135.

Lu C H., Hwang W. J., (1996), “Phasic and microstructural developments of $Pb(Ni_{1/3}Nb_{2/3})O_3$ prepared by the columbite precursor process”, Ceramics international, 22(5), 373-379.

Mahajan S., Thakur O. P., Prakash C., (2007), “Effect of Sintering Temperature on Structural and PiezoelectricProperties of PNN-PZT Ceramics”, Defence Science Journal; Vol 57, No 1, 23-28.

Mahajan S., Prakash C., Thakur O. P., (2009), “Piezoelectric properties of 0.5 $(PbNi_{1/3}Nb_{2/3})\ O_3$–0.5 $Pb(Zr_{0.32}Ti_{0.68})\ O_3$ ceramics prepared by solid state reaction and mechanochemical activation-assisted method”, Journal of alloys and compounds, 471(1-2), 507-510.

Mensur Alkoy E., Tekdas A. S., Berksoy A., (2011), “Electrical Properties of 1–3 Piezocomposites with Potassium Sodium Niobate Fibers”, Ferroelectrics, 420(1), 1-6.

Mensur Alkoy E., Kaya M. Y., Avdan D., Alkoy S. (2016), “Properties of $[Pb(Zn_{1/3}\ Nb_{2/3})O_3]_x$–$[Pb(Zr_{0.48}Ti_{0.52})O_3]_{(1-x)}$ Ceramics With Low Sintering Temperature and Their 1–3 Piezocomposites”, EEE Transactions on Ultrasonics, Ferroelectrics, and Frequency Control, 63(6), 907-914.

Mensur Alkoy E., Kaya M. Y., Sarı H. A., Pekel O., Olukkent R., Tur Y. K., Alkoy, S., (2020), “Mechanical and electromechanical properties of piezoelectric ceramic fibers drawn by th alginate gelation method”, International Journal of Applied Ceramic Technology, 17(3), 1371-1381.

Miclea C., Tanasoiu C., Miclea C. F., Tanasoiu V., (2002), “Advanced electroceramic materials for electrotechnical applications”, J. Optoelectron. Adv. Mater, 4, 51-58.
Moulson A. J., Herbert J. M., (2003), “Electroceramics: Materials, Properties, Applications”, 2nd Edition., John Wiley & Sons Ltd, England.

Newnham R. E., Skinner D. P., Cross L. E., (1978), "Connectivity and piezoelectric-pyroelectric composites", Materials Research Bulletin, 13(5), 525-536.

Newnham R. E. (2005). Properties of materials: anisotropy, symmetry, structure. Oxford University Press on Demand.

Nie R., Zhang Q., Yue Y., Liu H., Chen Y., Chen Q., Xiao D. (2016). Phase structure–electrical property relationships in Pb $(Ni_{1/3}Nb_{2/3})O_3$–Pb(Zr, Ti)O_3-based ceramics. Journal of Applied Physics, 119(12), 124111

Özyazıcı M. G., (2018), "Investigation of electrical properties of Pb$(Ni_{1/3}Nb_{2/3})O_3$-Pb(Zr,Ti)O_3(PNN-PZT) ceramics and their device applications ", Master's Thesis, Gebze Technıcal University.

Padasalkar G. G., Shaikh J. M., Syed Y. D., Tamboli S. H., Phutane P. S., (2015), "A review on piezoelectricity", IJAREEIE, 4, 8231-8235.

Pan J. S., Zhang X. W., (2007), "Structure and Electrical Properties of Pb $(Ni_{1/3}Nb_{2/3})O_3$-Pb (Zr/Ti)O_3 Relaxors", Key Engineering Materials, 336 (30-32)

Peláiz-Barranco A., Calderón-Piñar F., García-Zaldívar O., González-Abreu Y., (2012), "Relaxor behaviour in ferroelectric ceramics", Advances in Ferroelectrics, 85-107.

Peng G.-g., Zheng D.-y., Cheng C., Zhang J., Zhang H., (2017), "Effect of rareearth addition on morphotropic phase boundary and relaxation behavior of the PNN-PZT ceramics", Journal of Alloys and Compounds, 693 1250-1256.

Pu T., Chen H., Xing J., Luo Y., Fan S., Liu H., Zhu, J., (2022), "High piezoelectricity of low-temperature sintered Li_2CO_3-added PNN–PZT relaxor ferroelectrics", Journal of Materials Science: Materials in Electronics, 33(8), 4819-4830.

Roth R. S., (1957), "Classification of perovskite and other ABO_3-type compounds", Journal of Research of the National Bureau of Standards, 58(2), 75-88.

Safari A., Jadidian B., Akdogan, E. K. (2000), "Piezoelectric composites for transducer applications", Comprehensive Composite Materials, 533-561.

Setter N., Waser R., (2000), "Electroceramic materials", Acta materialia, 48(1), 151-178.

Singh V., Kumar V. V., Kharat D.K., Kulkarni M.P., (2007), "Effect of Heating Rate on Electromechanical Properties ofPNN–PZT Solid Solution", Defence Science Journal, Vol. 57, No 1, 51-54.

Sutjarittangtham K., Tawichai N., Intatha U., Eitssayeam, S., Pengpat, K., Rujijanagul G., Tunkasiri, T., (2009), "Electrical Properties and Phase Transition Behaviors of Sn

Doped 0.45 PZT-0.55 PNN Ceramics", AIP Conference Proceedings, Vol. 1151, No. 1, 174-176.

Trolier-McKinstry S., Zhang S., Bell A. J., Tan X., "High-performance piezoelectric crystals, ceramics, and films", Annual Review of Materials Research, 48, 191-217.
Uchino K., (2018), "Ferroelectric devices", Second Edition, CRC press.

Vilarinho P. M., (2005), "Functional materials: properties, processing and applications" In Scanning Probe Microscopy: Characterization, Nanofabrication and Device Application of Functional Materials", Springer, Dordrecht, 3-33.

Vittayakorn N., Rujijanagul G., Tan X., Marquardt M. A., Cann D. P., (2004), "The morphotropic phase boundary and dielectric properties of the $xPb(Zr_{1/2}Ti_{1/2})O_3$-$(1-x)Pb(Ni_{1/3}Nb_{2/3})O_3$ perovskite solid solution", Journal of Applied Physics, 96(9), 5103-5109.

Wang P., (2012), "The general properties and applications of ceramic materials", Applied Mechanics and Materials, Vol. 174, 215-218.

Wang H., Zhang F., Chen Y., Huang C., Wang X., Wu X., Xing, J., (2021), "Giant piezoelectric coefficient of PNN-PZT-based relaxor piezoelectric ceramics by constructing an RT MPB", Ceramics International, 47(9), 12284-12291.

Xu Y., (2013), "Ferroelectric materials and their applications", Elsevier.

Yalcin E., Ankut M., Sungur S. M., Turgut H. I., Kar K. S., Alkoy S., Menşur E., (2021), "Comparison of the performance characteristics of the tonpilz transducers fabricated from 0.60 PMN-0.40 PT & PZT piezoceramics", Ferroelectrics, 586(1), 82-92.

Yang S., Bao H., Zhou C., Wang Y., Ren X., Matsushita Y., Gao J., (2010), "Large magnetostriction from morphotropic phase boundary in ferromagnets", Physical review letters, 104(19), 197201.

Yi J., Jiang S., Liu S., Zhang L., He J., (2014), "Effects of $LiBiO_2$ addition on the microstructure and piezoelectric properties of CuO-doped PNN–PZT ceramics", Physica Status Solidi (A), 211 (11), 2552-2557.

Yi J., Shen M., Liu S., Jiang S., (2015), "Effects of PbO-B_2O_3 glass doping on the sintering temperature and piezoelectric properties of 0.35 Pb $(Ni_{1/3}Nb_{2/3})O_3$-0.65Pb $(Zr_{0.41}Ti_{0.59})O_3$ ceramics.

Yoon C. B., Jun S. H., Lee S. M., Kim H. E., Lee K. W., (2006), "Piezoelectric Fibers with Uniform Internal Electrode by Co-Extrusion Process", Journal of the American Ceramic Society, 89(4), 1333-1336.

Yue Y., Zhang Q., Nie R., Yu P., Che Q., Liu H., Song H., (2017), "Influence of sintering temperature on phase structure and electrical properties of 0.55Pb $(Ni_{1/3}Nb_{2/3})O_3$–0.45Pb $(Zr_{0.3}Ti_{0.7})O_3$ ceramics" Materials Research Bulletin, 92, 123-128.

Wang H., Zhu K., Qiu J., Luo J., Ji H., (2010), “Ferroelectric and piezoelectric properties of Pb $(Ni_{1/3}Nb_{2/3})0.5(Ti_{0.7}Zr_{0.3})0.5O_3$ ceramics fabricated by tape-casting process” Ferroelectrics, 396(1), 90-97.

BIOGRAPHY

Ezgi Yalçın received the B.S. degree in materials science and engineering in 2016 from Erciyes University.

She worked as a quality control engineer at Tosyalı Toyo Çelik. A. Ş between 2017-2019. She worked as a mechanical process engineer at ALP Havacılık between 2019-2021. She started her master's degree in Material Science and Engineering at Gebze Technical University in 2021. In 2021, she started to work as research assistant at the same department.